Ab-initio Study of Hydrogen Technology Materials for Hydrogen Storage and Proton Conduction.

Dissertation
zur Erlangung des Grades

"Doktor der Naturwissenschaften"

dem Fachbereich Chemie, Pharmazie und Geowissenschaften
der Johannes Gutenberg-Universität Mainz
vorgelegt von

Guillermo Andrés Ludueña
geboren in Córdoba, Argentina

Mainz 2011

Die vorliegende Arbeit wurde in der Zeit
von Oktober 2007 bis Oktober 2010
am Max-Planck-Institut für Polymerforschung
angefertigt.

A ▭,
▭ y ▭.

Abstract

This dissertation deals with two specific aspects of a potential hydrogen-based energy economy, namely the problems of energy storage and energy conversion. In order to contribute to the solution of these problems, the structural and dynamical properties of two promising materials for hydrogen storage (lithium imide/-amide) and proton conduction (poly[vinyl phosphonic acid]) are modeled on an atomistic scale by means of first principles molecular dynamics simulation methods.

In the case of the hydrogen storage system lithium amide/imide ($LiNH_2$/-Li_2NH), the focus was on the interplay of structural features and nuclear quantum effects. For these calculations, Path-Integral Molecular Dynamics (PIMD) simulations were used. The structures of these materials at room temperature were elucidated; in collaboration with an experimental group, a very good agreement between calculated and experimental solid-state ^1H NMR chemical shifts was observed. Specifically, the structure of Li_2NH features a disordered arrangement of the Li lattice, which was not reported in previous studies. In addition, a persistent precession of the NH bonds was observed in our simulations. We provide evidence that this precession is the consequence of a toroid-shaped effective potential, in which the protons in the material are immersed. This potential is essentially flat along the torus azimuthal angle, which might lead to important quantum delocalization effects of the protons over the torus.

On the energy conversion side, the dynamics of protons in a proton conducting polymer (poly[vinyl phosphonic acid], PVPA) was studied by means of a steered *ab-initio* Molecular Dynamics approach applied on a simplified polymer model. The focus was put on understanding the microscopic proton transport mechanism in polymer membranes, and on characterizing the relevance of the local environment. This covers particularly the effect of water molecules, which participate in the hydrogen bonding network in the material. The results indicate that these water molecules are essential for the effectiveness of proton conduction. A water-mediated Grotthuss mechanism is identified as the main contributor to proton conduction, which agrees with the experimentally observed decay on conductivity for the same material in the absence of water molecules.

The gain in understanding the microscopic processes and structures present in this materials can help the development of new materials with improved properties, thus contributing to the solution of problems in the implementation of fuel cells.

Zusammenfassung

Diese Dissertation behandelt zwei spezifische Aspekte einer vielversprechenden wasserstoffbasierten Ökonomie: die Energiespeicherung und die Energiekonversion. Um sich der Lösung dieser Problemstellungen zu nähern, werden die strukturellen und dynamischen Eigenschaften zweier aussichtsreicher Materialien für die Wasserstoffspeicherung (Lithiumimid/-amid) und für die Protonenleitung (Polyvinylphosphonsäure) auf der atomistischen Skala per ab-initio Molekulardynamik modelliert.

Im Fall des Wasserstoffspeicherungssystems Lithiumamid/-imid ($LiNH_2/Li_2NH$), wurde der Schwerpunkt auf das Zusammenspiel von strukturellen Eigenschaften und Kernquanteneffekten gelegt. Für die Berechnungen wurden pfadintegrale Molekulardynamik-Simulationen (Path-Integral Molecular Dynamics, PIMD) angewendet. Diese Methode diente der Aufklärung der Struktur der untersuchten Materialien bei Raumtemperatur; in Zusammenarbeit mit einer experimentellen Gruppe konnte eine sehr gute Übereinstimmung zwischen den errechneten und den experimentell gemessenen Werten für den chemischen Übergang in der Festkörper-Protonen-Kernspinresonanzspektroskopie (NMR) beobachtet werden. Insbesondere bei der Struktur von Li_2NH stellte sich ein ungeordneter Aufbau des Li Gitters heraus, welcher in vorausgegangenen Studien noch nicht beschrieben wurde. Außerdem wurde eine anhaltende Kreiselbewegung der NH-Verbindungen in unserer Simulationen registriert. Wir haben nachgewiesen, dass diese Kreiselbewegung die Folge eines toroidgeformten effektiven Potenzials ist, in dem die Protonen versenkt sind. Dieses Potenzial ist im Wesentlichen flach entlang des Torus-Azimut-Winkels. Dieser Umstand könnte die wahrnehmbaren Quantendelokalisationsfekte des Protonens bedingen.

Zur Untersuchung der Energiekonversion wurde die Dynamik der Protonen anhand eines protonenleitfähigen Polymers (Polyvinylphosphonsäure, PVPA) studiert. Dazu wurde ein gesteuerter molekulardynamischer ab-initio Ansatz für ein vereinfachtes Polymermodell angewendet. Ziel war das Gewinnen neuer Erkenntnisse über den mikroskopischen Protonenleitungsmechanismus in Polymermembranen, sowie die Charakterisierung der Relevanz der lokalen Umgebung. Bei Letzterem wurde der Fokus hauptsächlich auf die Effekte von Wassermolekülen gelegt, die an der Wasserstoffverbindung im Material beteiligt sind. Die Ergebnisse lassen den Schluss zu, dass die Wassermoleküle essentiell für die Effektivität der Protonenleitung sind. Es hat sich herausgestellt, dass ein wasservermittelter Grotthuss Mechanismus einen Hauptbeitrag zur Protonenleitung leistet, was sich mit der experimentell nachgewiesenen Erkenntnis deckt, dass die Protonenleitung in diesem Material bei extrem niedriger Feuchtigkeit zusammenbricht.

Der Verständnisgewinn über die mikroskopischen Prozesse und die Materialeigenschaften kann dem Zweck dienen, die Entwicklung neuer Materialien mit verbesserten Eigenschaften voranzutreiben, sowie dann eine Lösung für die praktische Umsetzung der Brennstoffzelle zu finden.

Abbreviations

au: Atomic Units
BLYP: Becke Lee Yang Parr (energy functional)
BO: Born-Oppenheimer
CPMD: Car Parrinello Molecular Dynamics
DFT: Density Functional Theory
FPMD: First-Principles Molecular Dynamics
GGA: Generalized Gradient Approximation
HEG: Homogeneous Electron Gas
HK: Hohenberg-Kohn
KS: Kohn-Sham
LDA: Local Density Approximation
MD: Molecular Dynamics
NMR: Nuclear Magnetic Resonance
PEMFC: Proton Exchange Membrane Fuel Cell
PES: Potential Energy Surface
PIMD: Path-integral Molecular Dynamics
ppm: Parts per million
PP: Pseudopotential
PVPA: poly[vinyl phosphonic acid]
PW: Plane Wave
SCF: Self Consistent Field

Contents

1 Introduction **1**

1.1 Technological background 4

1.1.1 *Proton Exchange Membrane Fuel Cells* . . . 4

1.1.2 *Hydrogen storage* 7

2 Theoretical Background **11**

2.1 Density Functional Theory (DFT) 11

2.1.1 *The Schrödinger equation* 12

2.1.2 *Born-Oppenheimer Approximation* 13

2.1.3 *Hohenberg-Kohn (HK) Theorems* 15

2.1.4 *The Kohn-Sham (KS) Method* 16

2.1.5 *The Exchange-Correlation Functional* 21

2.1.6 *Basis Sets* 24

2.1.7 *Pseudopotentials (PP)* 29

2.1.8 *Mixed Gaussian and Plane Waves Method* . 32

2.2 *Ab-initio* Molecular Dynamics Simulations 34

2.2.1 *Born-Oppenheimer Molecular Dynamics* . . 36

2.2.2 *Car-Parrinello Molecular Dynamics (CPMD)* 37

2.2.3 *The Nosé-Hoover Thermostat* 39

2.2.4 *Accelerated BOMD and Langevin dynamics* 41

2.3 Path Integral Molecular Dynamics (PIMD) . . . 44

2.3.1 *Derivation of the Formalism* 45

2.4 Calculation of Chemical Shifts from DFT 51
2.4.1 *Derivation* 53
2.5 Final Remarks 56

3 The Li_2NH–$LiNH_2$ Hydrogen Storage System 57
3.1 Methods 60
3.1.1 *Computational setup* 60
3.2 Structural properties 62
3.2.1 *Local disorder in lithium imide (Li_2NH)* . . . 62
3.2.2 *$LiNH_2$ calculations* 69
3.2.3 *NMR chemical shifts* 72
3.2.4 *Diffraction Patterns* 76
3.3 Quantum properties of protons in Li_2NH 77
3.3.1 *Quantum particle density* 78
3.3.2 *Proton delocalization in isolated molecules* . 81
3.3.3 *Convergence of the bead distribution's width* . 83
3.4 Conclusion 88

4 High Temperature Proton Conduction in PVPA 91
4.1 Setup 95
4.2 Dynamics of Proton hopping 97
4.2.1 *On the decay law of $\eta(t)$* 100
4.3 Proton conductivity σ and the Q variable 107
4.3.1 *$\Delta\tilde{Q}$ and the O-O distance of a jump.* 112
4.4 Conclusion 114

5 Summary 117

A Proof of the Hohenberg-Kohn Theorems 123
A.1 First HK Theorem 123
A.2 Second HK Theorem 125

Chapter 1

Introduction

The economic activities of modern society are driving it to a confrontation with the problems of imminent shortage of fossil fuels and global warming. These issues will eventually force the society to transform the economy, putting emphasis on renewable energies. The challenge represents a milestone in modern history and an opportunity for countries aiming to establish themselves at a good position in the economy of the future. The successful adaptation of the present energy infrastructure based on fossil fuels to renewable energies will involve a broad range of sectors, in particular from science and technology.

One of the most promising models for the *clean energy*-based economy is the so-called *Hydrogen economy* [16]. In this model, energy is to be generated from many processes, preferably renewable energy sources like solar cells, wind mills, geothermic or hydroelectric centrals among others. The generated energy would today be distributed by an electrical network. Such a solution is enough for many necessities, but it leaves out one of the most important and most fuel-dependent activities: the transport industry. Here is where hydrogen comes into play.

Hydrogen itself is the most abundant component in the known universe. The pure element is, however, virtually absent on our planet, while it is found abundantly forming other compounds. Hydrogen is therefore to be obtained from decomposition of natural compounds, like e.g. by electrolysis of water. As a consequence, hydrogen is not relevant as an energy *source* but rather as an energy *vector*. The energy produced by the aforementioned processes is to be stored in hydrogen, either in its gas form as molecular H_2 or forming other compounds, from which the energy stored chemically could be efficiently reverted. The process of energy production, storage and conversion is then completed by transforming the energy stored in hydrogen into electricity. This last step of energy conversion would be carried within e.g. Proton Exchange Membrane Fuel Cells (PEMFCs, see next section), leaving preferably a byproduct with low environmental impact, like water.

There is a big gap between the technical and economic advantages of hydrogen technology and the state-of-the-art fossil-fuel based technologies. For the task of filling this gap, the design of better functional materials is crucial.

In this work, we address the problems of energy conversion and energy storage by studying the properties at an atomic level of two promising materials for hydrogen storage (lithium imide/amide) and proton conduction (poly[vinyl phosphonic acid], PVPA). The gain in the understanding of the microscopic processes and structures in this materials can help the development of new materials with improved properties. This knowledge is provided in this work from a theoretical approach, consisting of methods which fall under the scope of *ab-initio* Molecular Dynamics. This methods consist roughly in simulating the dynamics of the atoms in the bulk materials, fully considering the quantum properties of electrons and to some degree also of the atomic nuclei. In *ab-initio* Molecular Dynamics, the atomic orbitals are computed from the individual solutions of the electronic Schrödinger equation, that is, by calculating the quantum state of the electrons in the molecular system. This allows access to properties like for example formation and breaking of covalent bonds, H-bonding energies or electronic interaction, which are not accessible from Molecular Dynamics simulations based on force fields.

The theory behind the computational methods used throughout this work is exposed in chapter 2. The contents of sections 2.1 and 2.2 describe the Density Functional Theory (DFT) and the Molecular Dynamics (MD) method, which are the basis of the whole work. Sections 2.3 and 2.4 describe path-integral molecular dynamics (a simulation technique which enables the quantum treatment of atomic nuclei) and Nuclear Magnetic Resonance (NMR) calculations from DFT.

In chapter 3 the lithium amide/imide hydrogen storage system is studied. The focus is made on the structural properties of this materials, with a particular emphasis in the imide, for which the discussion about the correct structure has generated much debate [80, 17, 123]. The quantum properties of nuclei are taken into account and the possibility of proton quantum delocalization is put under consideration. As a bridge between theoretical simulation and the actual material, spectroscopic observables have been computed under different structural assumptions. In particular, the ^{1}H NMR spectra were calculated and compared with experimental results, yielding a very good agreement.

In chapter 4 the proton conduction process is studied in poly[vinyl phosphonic acid] (PVPA). In order to study this macroscopic phenomena on the atomic level, we model proton conduction in a simplified polymer model as the response to a constant force bias. The model is studied under different concentrations of water and compared with the experimentally observed behavior. Then, the main processes involved in proton conduction are identified, in particular the function of water molecules embedded in the structure of the polymer and its relevance for proton conduction.

1.1 Technological background

1.1.1 *Proton Exchange Membrane Fuel Cells*

Proton exchange membrane fuel cells (PEMFC) (for an extensive review see e.g. [56]) are electrochemical cells that produce electricity from a fuel source, usually molecular hydrogen gas.

In a PEMFC (see fig. 1.1), the cathode and anode, as well as the fuel and the oxidant, are separated by an electrolyte membrane through which only the positive charges should travel. From the resulting potential difference, electricity circulates through an external electrical circuit. Both fuel (usually molecular H_2) and oxidant (typically oxygen free in the air) must be continually inserted in their respective sides of the cell. A reaction takes place in the cathode side, where oxygen molecules in the air meet the electrons coming from the circuit along with the protons, which have traveled through the membrane, thus leaving water as a subproduct. This reaction, as well as the separation of protons and electrons in the anode, is helped by

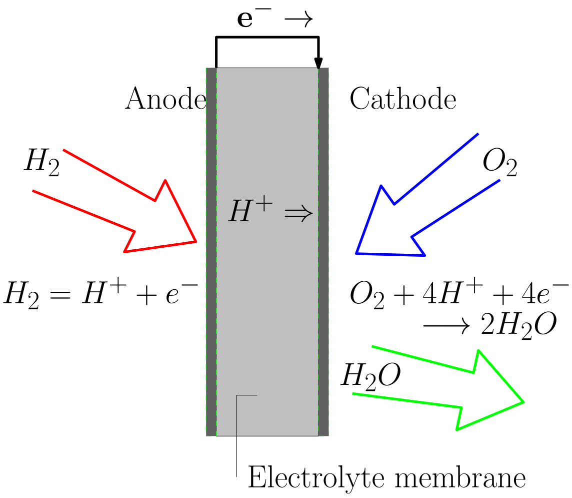

Figure 1.1: Scheme of a Proton Exchange Membrane Fuel Cell.

the presence of a catalyst, which is usually a thin platinum layer. The need of this precious material is one of the main economical and practical drawbacks of this technology (even if we assume the high costs of a precious material, the future availability of this material is strongly limited). This problem spanned interest in alternative approaches, like e.g. Fe-based catalysts [76, 24].

The main difference between PEMFC and classical electrochemical cell batteries is the fact that in in the former, there is material coming in and out of the cell, which brings energy to the device. A battery is instead a closed system, where the electricity is chemically stored, and only energy is exchanged with the environment.

High temperature proton conducting membranes

The state-of-the-art proton conducting membrane material used in the industry is Nafion$^{(R)}$. It consists in a hydrofobic polymer matrix, in which water channels are embedded. It is precisely in those water channels where the proton conduction process takes place. The conductivity of this type of membranes is therefore highly dependent on the water content. The requirement to maintain a high level of hydration restricts the operating temperature to 100°C. This constrain gives rise to the problem that at such a low temperature, CO poisoning of the electrode quickly damages the catalyst and strongly reduces the performance of the fuel cell. To avoid this poisoning, it is necessary to use highly pure hydrogen as a fuel and noble metals as electrode materials, which makes production extremely expensive. In addition, the use of those materials cannot be sustained in the future, as the provisions of this rare materials will eventually extinguish as the introduction of this technology becomes mainstream. Operating the PEMFCs at high temperatures would reduce CO poisoning, due to the increased activity of the catalyst. For this reason, various approaches have been proposed, aiming at developing new classes of proton conducting membranes for high-temperature proton exchange membranes (PEMs).

Polymer membranes containing phosphonic acid groups are one of the promising candidates for PEMs. Aside from the material components, cross linking between polymer chains containing sulfonic acid was reported to provide proton conductivity comparable to Nafion$^{(R)}$ and to enhance mechanical stability [103]. Therefore, there has been a lot of research towards combining these properties, in order to achieve high proton conductivity as well as the mechanical strength needed for the technological implementation of PEMs. Among other possibilities, poly[vinyl phosphonic acid] (PVPA) is one promising proton conducting material which does not form water channels. However, the conductivity of the material is lost when highly dried, a result that remained unexplained. In this work, we consider PVPA to be a model system to study the behavior of this kind of proton conductors on an atomistic level, with the aim of gaining a deeper understanding of the processes involved in proton conduction at that level, a knowledge that should help the design of "dry" proton conducting materials. The study is presented in chapter 4.

1.1.2 *Hydrogen storage*

The Hydrogen storage problem is one of the main unsolved issues for the introduction of hydrogen economy. The problem has been addressed with many approaches, with both physical storage (compression and liquefaction) and chemical storage (metal hydrides, clathrates, metal organic frameworks, carbon nanotubes, among others [93, 78, 110]).

One kilogram of hydrogen occupies a volume of 11 m^3 at atmospheric pressure. The classical solution for transporting gas is to compress it into steel tanks. This solution is typical in many countries where *natural gas* (consisting mostly of Methane) is used to fuel cars. This tanks are typically filled to 200 bar, with some 45 liters of internal volume. Using this technology would allow to carry 1.2 Kg of Hydrogen, giving an autonomy of $\sim$60 Km (today a car is expected to have around 400 Km autonomy). This number is not completely discouraging and technological advances in the design (including the use of better materials) of the tubes allow for 600 and even 700 bar compression, which combined with a bigger tank sizes can give reasonable autonomy (678 Km of autonomy are claimed by Mercedes-Benz[1] with 700 bar tubes). However, these containers would carry a 4 %wt., along with the security issues related to the daily use of high pressure gas. In addition, hydrogen has an extremely low condensation temperature (-252°C), which makes liquid or solid transport an inconvenient option.

The above drawbacks could be overcome by adsorption of the gas into a solid. In this manner, the hydrogen would be stored in a material, significantly losing volume. The problem in this case is to find a sufficiently light material, which adsorbs hydrogen and (ideally) reversibly liberates it when needed. This chemical storage technology is still in early stage of development. One of the most successful methods of this kind is to keep the hydrogen in a hydride form. Hydrides chosen for storage applications provide low reactivity (high safety) and high hydrogen storage densities. Some extensively studied materials in this group are complex and metal hydrides like LiH, $NaBH_4$ and $LiAlH_4$. More recently, extensive interest has been focused on lightweight hydrides like MgH_2, $LiBH_4$ and Li_2NH, due to its high gravimetric and volumetric hydrogen densities. All of these materials have some practical drawbacks for the full implementation, which occur mainly due to a high thermal stability, slow absorption/desorption kinetics, irreversibility of cycling and undesirable byproduct gases (like ammonia).

A deeper understanding of the nature of this materials to an atomistic level could be of great relevance to find a solution to this problems. In this work, the structural properties of the Lithium imide/amide (Li_2NH/$LiNH_2$) storage system and its

---

[1] as officially presented in the IAA exposition, Frankfurt am Main 2009

nuclear quantum properties were studied in detail. The outcome of this study is presented in chapter 3.

Chapter 2

Theoretical Background

This chapter contains the basic conceptional ideas of electronic structure theory, in particular of Density Functional Theory (DFT), as well as an introduction to molecular dynamics simulation methods. The combination of both techniques (often denoted as *ab-initio molecular dynamics* simulations) provides a tool to obtain a statistical ensemble of conformations of a (supra-) molecular system, based on the time-propagation of the equations of motion using a potential energy surface generated from a quantum-mechanical description of the electronic degrees of freedom.

2.1 Density Functional Theory (DFT)

Density Functional Theory (DFT)[7, 63, 47] is one of the most popular methods available for the study of the electronic structure of many-body systems. Starting from the time-independent Schrödinger equation for the electronic many-body wavefunction, a conceptional simplification is introduced by moving the focus of interest towards the electronic density. While the many-body wavefunction is a function that depends on the ensemble of coordinates of electrons, the density only depends on a single set of coordinates. This considerably reduces the dimensionality of the equations that have to be solved, which in turn lowers the required computational effort. Throughout this thesis, DFT is used as the fundamental technique for the description of electronic structure and for the calculation of the potential energy hypersurface.

2.1.1 *The Schrödinger equation*

The quantum state of an ensemble of non-relativistic particles is described by the wavefunction of the system, which is a function that depends on the spatial variables of all particles, specifically the atomic and electronic coordinates. The wavefunctions that describe stationary states of a system must be solutions of the time-independent Schrödinger equation, which is an eigenvalue equation for the wavefunction. Its eigenvalues represent the energies of the considered system in the respective quantum states.

For simplicity, all equations in this chapter are expressed in atomic units (au). In this units, a rescaling of variables is applied, by which the electron mass m_{e}, the elementary electron charge q_e, the reduced Planck's constant $\hbar = \frac{h}{2\pi}$ and Coulomb's constant $\frac{1}{4\pi\epsilon_0}$ have unity value.

For a system consisting of n electrons and N nuclei, the time-independent[1] Schrödinger equation is given by

$$\mathcal{H}\chi(\mathbf{r}_1, \ldots, \mathbf{r}_n, \mathbf{R}_1, \ldots \mathbf{R}_N) = E\chi(\mathbf{r}_1, \ldots, \mathbf{r}_n, \mathbf{R}_1, \ldots \mathbf{R}_N) \ . \quad (2.1)$$

---

[1] In this section, whenever the Schödinger equation is addressed, it is referred to its time-independent case.

Here, the Hamiltonian $\mathcal{H}$ is defined as

$$\begin{aligned}
\mathcal{H} &= \underbrace{\sum_i -\frac{1}{2}\nabla_i^2}_{\equiv T_E} + \underbrace{\sum_I -\frac{1}{2M_I}\nabla_I^2}_{\equiv T_N} + \frac{1}{2}\sum_i \sum_{j\neq i} \frac{1}{|\mathbf{r}_i - \mathbf{r}_j|} + \\
&\quad + \frac{1}{2}\sum_I \sum_{J\neq I} \frac{Z_I Z_J}{|\mathbf{R}_I - \mathbf{R}_J|} - \sum_i \sum_I \frac{Z_I}{|\mathbf{r}_i - \mathbf{R}_I|} \qquad (2.2) \\
&\equiv \mathcal{H}_0 + T_N \ , \qquad (2.3)
\end{aligned}$$

where the lowercase indices label electrons (i, j), the capital index (I) labels nuclei, M_I is the nuclear mass of nucleus I and Z_I is the number of elemental charges in the nuclei. The position operators of the electron and nuclei, $\mathbf{r}$ and $\mathbf{R}$, follow the same notation. The wavefunction of a system of n electrons and N nuclei has $3(N+n)$ variables, which generally prohibits an exact solution of the Schrödinger equation, be it analytically or numerically, except for very simple situations like single isolated atoms.

2.1.2 *Born-Oppenheimer Approximation*

In the Schrödinger equation, both nuclei and electrons are treated as quantum particles on the same footing. Therefore the wavefunction of the system depends both on the positions of the electrons and the nuclei, resulting in a high dimensionality of the wavefunction. However, nuclei and electrons are significantly different in their masses (the proton mass is about 2000 times larger than that of the electron). It turns out that this substantial difference in the mass of the particles involved enables a separation of the two variables in the equation which considerably reduces the computational effort required to solve the equations.

Defining $\kappa = \frac{1}{M}$ as the ratio of the masses of electron and proton, the total Hamiltonian in eq. (2.3) can be rewritten, by rewriting the kinetic energy T_N of the nuclei as

$$T_N = \kappa\mathcal{H}_1, \qquad \mathcal{H}_1 = -\sum_I \frac{1}{2A_I}\nabla_I^2 \, , \tag{2.4}$$

where A_I is the number of protons and neutrons in the nucleus. This enables us to write the Hamiltonian as

$$\mathcal{H} = \mathcal{H}_0 + \kappa\mathcal{H}_1 \; . \tag{2.5}$$

Since $\kappa \ll 1$, the nuclear kinetic energy can be treated as a perturbation. Using the classical analogy principle, this would correspond to the situation that the motion of the nuclei is much slower that that of the electrons, and thus the nuclear motion is decoupled from the electronic degrees of freedom. Consequently, an Ansatz for the total wavefunction would reflect this by factorizing the function as a product of an electronic and a nuclear wavefunction:

$$\chi(\mathbf{r}_1, \ldots, \mathbf{r}_n, \mathbf{R}_1, \ldots, \mathbf{R}_N) = \Psi_{R_1,\ldots,R_N}(\mathbf{r}_1, \ldots, \mathbf{r}_n)\,\Phi(\mathbf{R}_1, \ldots, \mathbf{R_N})\, , \tag{2.6}$$

where the positions of the nuclei $\{\mathbf{R}_1, \ldots \mathbf{R}_N\}$ are only parameters for the electronic wavefunction.

This simplifies the original problem to an equation for the electronic wavefunction which must be solved for fixed atomic (nuclear) positions $\mathbf{R}_I$:

$$\mathcal{H}^{el}\Psi_{R_1,\ldots,R_N}(\mathbf{r}_1, \ldots, \mathbf{r}_n) = E_{R_1,\ldots,R_N}\Psi_{R_1,\ldots,R_N}(\mathbf{r}_1, \ldots, \mathbf{r}_n) \; , \tag{2.7}$$

with

$$\mathcal{H}^{el} \;=\; \underbrace{\sum_i -\frac{1}{2}\nabla_i^2}_{T} + \underbrace{\frac{1}{2}\sum_i\sum_{j\neq i}\frac{1}{|\mathbf{r}_i - \mathbf{r}_j|}}_{V_{ee}} - \sum_i\sum_I \frac{Z_I}{|\mathbf{r}_i - \mathbf{R}_I|} \, , \tag{2.8}$$

where T is the kinetic energy operator and V_{ee} is the electron-electron electrostatic potential. This new equation has only the $3n$ electronic degrees of freedom, which represents an important simplification compared to the original Schrödinger equation.

2.1.3 *Hohenberg-Kohn (HK) Theorems*

A very successful approach to solve the electronic quantum many-body problem consists in considering the electronic density as the central quantity, instead of the electronic wavefunction. This method is based on two fundamental theorems by Hohenberg and Kohn (HK) [35]. The first theorem states:

Theorem 1 (First Hohenberg-Kohn theorem)**.** *The external potential $v(\mathbf{r})$ is determined, within a trivial additive constant, by the electron density $\rho(\mathbf{r})$.*

The proof of this theorem can be found in the appendix A.1, and a good discussion is given in [87, sec. 3.2, 3.3].

Noting that the electron density describes the total number and the spatial distribution of the electrons, thus determining the potential and therefore the Hamiltonian, it is visible that it uniquely defines the quantum state of the electrons. Thus, the corresponding wavefunction $\Psi_0(\mathbf{r}_1, ..., \mathbf{r}_n)$ is uniquely determined by the electronic density $\rho_0(\mathbf{r})$. It is therefore formally possible to express the electronic wavefunction as a functional of the electronic density, which in turn enables a description of all properties of the system which are based on the electronic structure as a functional of the density.

The second HK theorem provides the energy variational principle to find the ground state density.

Theorem 2 (Second Hohenberg-Kohn theorem)**.** *For a trial density $\tilde{\rho}(\mathbf{r})$, such that $\tilde{\rho}(\mathbf{r}) \geq 0$ and $\int \tilde{\rho}(\mathbf{r})\mathrm{d}\mathbf{r} = N$, the energy functional value of the corresponding distribution $E_v[\tilde{\rho}]$ is an upper bound of the ground state E_0,*

$$E_0 \leq E_v[\tilde{\rho}] \tag{2.9}$$

As in the case of the first theorem, a proof can be found in appendix A.2. In principle, this theorem provides a recipe for actually obtaining the ground-state density by minimizing the energy functional. Also in this context, it is important to note that the direct application of this theorem is limited by the fact that no closed expression is known for this general energy functional. At present, it does not appear likely that an exact expression will be found in the future.

2.1.4 *The Kohn-Sham (KS) Method*

The HK theorems provide the formal basis to construct a method that determines the electronic ground state density and thus derive molecular properties of interest. As stated before, no closed expression is known for the energy functional $E_v[\rho]$ that must be minimized. This drawback can be overcome to a great extent by the *Kohn-Sham* (KS) method [54].

In their approach, Kohn and Sham propose the introduction of a fictitious system of non-interacting electrons. These non-interacting electrons are subject to a potential energy $v_s(\mathbf{r}_i)$ (s subindices indicate the fictitious system). The idea is to adjust this potential such that the electronic density derived from the non-interacting set of electrons becomes equal to the electronic density of the real system, $\rho_s(\mathbf{r}) = \rho(\mathbf{r})$. According to the first HK theorem, the potential $v_s(\mathbf{r}_i)$ can be determined from the electronic ground-state density. Since we are treating a non-interacting system, the corresponding Hamiltonian $\mathcal{H}_s$ is the sum of one-particle operators,

$$\begin{aligned} \mathcal{H}_s &= \underbrace{\sum_{i=1}^{n} -\frac{1}{2}\nabla_i^2}_{T_s} + \sum_{i=1}^{n} v_s(\mathbf{r}_i) && (2.10) \\ &\equiv \sum_{i=1}^{n} h_i^{KS} \, , && (2.11) \end{aligned}$$

where h_i^{KS} is the one-particle KS Hamiltonian which acts on electron i, and T_s is the kinetic energy operator of the non-interacting system.

A suitable Ansatz for solving the Schrödinger equation for this Hamiltonian is therefore an product of the eigenfunctions of h_i^{KS}. In order to satisfy the Pauli exclusion principle, the resulting product function must subsequently be antisymmetrized. The set of n eigenfunctions with the lowest energy eigenvalues constitutes the ensemble of occupied single-particle states (also called KS orbitals, here denoted as $\theta_i^{KS}(\mathbf{r}_i)$). These orbitals solve the equations

$$h_i^{KS}\theta_i^{KS} = \varepsilon_i^{KS}\theta_i^{KS} \, , \qquad (2.12)$$

where ε_i^{KS} are effective one-electron energies. As a remark, the KS orbitals are not directly related to the exact many-body quantum wavefunction, but are rather solutions to the analogous non-interacting system of electrons. The same applies to their energies ε_i^{KS}, whose sum does *not* correspond to the total energies of the interacting system of electrons.

In order to express the exact energy functional (of the interacting set of electrons) on the basis of the ensemble of non-interacting electrons and their KS orbitals, it is helpful to define the quantities

$$\begin{aligned} \Delta T[\rho] &\equiv T[\rho] - T_s[\rho] \qquad (2.13) \\ \Delta V_{ee}[\rho] &\equiv V_{ee}[\rho] - \frac{1}{2} \int\int \frac{\rho(\mathbf{r}_1)\rho(\mathbf{r}_2)}{r_{1,2}} \, d\mathbf{r}_1 d\mathbf{r}_2 \, , \qquad (2.14) \end{aligned}$$

where $r_{1,2} \equiv ||\mathbf{r}_1 - \mathbf{r}_2||$. $\Delta T[\rho]$ is the difference between the kinetic energy of the interacting ($T[\rho]$) and non-interacting ($T_s[\rho]$) system, while $\Delta V_{ee}[\rho]$ is the difference between the respective electrostatic energies (the electron-electron potential V_{ee} is defined in eq. (2.8)). The explicit form of the functionals $\Delta T[\rho]$ and $\Delta V_{ee}[\rho]$ is unknown, as they include the terms $T[\rho]$ and $V_{ee}[\rho]$ of the interacting system. They are formally grouped into an *exchange-correlation energy functional* $E_{xc}[\rho]$

$$E_{xc}[\rho] \equiv \Delta T[\rho] + \Delta V_{ee}[\rho] \, , \qquad (2.15)$$

for which no closed expression can be given either, but for which a series of approximations exists.

The resulting energy functional reads:

$$E_v[\rho] = \int \rho(\mathbf{r}) v(\mathbf{r}) + T_s[\rho] + \frac{1}{2} \int\int \frac{\rho(\mathbf{r}_1)\rho(\mathbf{r}_2)}{r_{1,2}} \, d\mathbf{r}_1 d\mathbf{r}_2 + E_{xc}[\rho] \, . \qquad (2.16)$$

In this way, the total energy functional is expressed exclusively in terms of quantities defined within the fictitious non-interacting system of electrons. In practice, the central difficulty of incorporating the exact physical Coulomb operator between two electrons has been transformed into the problem of formulating a suitable closed expression for the exchange-correlation functional $E_{xc}[\rho]$. It turns out that approximative expressions can be found on the basis of the homogeneous electron gas (HEG), considered in the limits of low and high electronic density [7, 63, 88].

The kinetic energy functional $T_s[\rho]$ is formally written as a functional of the density, for which several approximations exist. However, in most cases, the kinetic energy functional is expressed in terms of the single-electron KS orbitals, which define the total density via

$$\rho = \rho_s = \sum_{i=1}^{n} |\theta_i^{KS}|^2 \ . \tag{2.17}$$

The kinetic term can be then calculated as

$$T_s[\rho] = -\frac{1}{2} \sum_{i=1}^{n} \langle \theta_i^{KS} | \nabla^2 | \theta_i^{KS} \rangle \ . \tag{2.18}$$

This representation of the electronic density in terms of KS orbitals is used to apply the variational principle of the second HK theorem. The electronic ground state is reached for those KS orbitals which render the DFT energy functional extremal. This corresponds to

$$\delta E_v[\{\theta_i^{KS}\}] = 0 \ . \tag{2.19}$$

As a consequence of the Pauli exclusion principle, the KS orbitals must be orthonormal,

$$\int \theta_i^{KS*}(\mathbf{r}) \theta_j^{KS}(\mathbf{r}) \, d\mathbf{r} = \delta_{ij} \ , \tag{2.20}$$

which can be incorporated into the variational principle in the form of an additional constraint with the help of a Lagrange multiplier technique. This yields an energy functional that has to be minimized with respect to both the electronic density and the Lagrange multipliers ε_{ij}:

$$\delta\left[E_v[\{\theta_i^{KS}\}]-\sum_{i=1}^{n}\sum_{j=1}^{n}\varepsilon_{ij}\int\theta_i^{KS*}(\mathbf{r})\theta_j^{KS}(\mathbf{r})\,d\mathbf{r}\right]=0\ , \quad (2.21)$$

where ϵ_{ij} are Lagrange multipliers.

This condition leads to a set of n equations for the n electronic orbitals, known as the *KS equations*,

$$\begin{aligned}\varepsilon_i^{KS}\theta_i^{KS}(\mathbf{r}) &= \left[-\frac{1}{2}\nabla^2+v(\mathbf{r})+\int\frac{\rho(\mathbf{r}')}{||\mathbf{r}-\mathbf{r}'||}\,d\mathbf{r}'+v_{xc}(\mathbf{r})\right]\theta_i^{KS}(\mathbf{r})\\ \varepsilon_i^{KS}\theta_i^{KS}(\mathbf{r}) &= h^{KS}\theta_i^{KS}(\mathbf{r})\ , \end{aligned} \quad (2.22)$$

where h^{KS} is the one-electron operator from eq. (2.10), and the potential $v_{xc}(\mathbf{r})$ is defined as

$$v_{xc}(\mathbf{r})\equiv\frac{\delta E_{xc}[\rho(\mathbf{r})]}{\delta\rho(\mathbf{r})}\ . \quad (2.23)$$

The potential $v(\mathbf{r})$ and the gradient term are the one-particle potential and kinetic energy operators, and the integral term comprises the electrostatic interactions (Hartree term). The equations have to be solved self-consistently. This means that a set of trial orbitals is used to build an electronic trial density, which is then inserted into the Hartree term. The resulting Hamiltonian is then used to improve the initial trial orbitals such as to yield the stationarity condition, eq. (2.22).

The central advantage of the KS approach is that the energy minimization problem can be solved iteratively as a set of n quasi-independent minimization problems for the set of n electronic orbitals. These minimizations are described by single-particle-equations, in which the exact interactions between the electrons are only taken into account via their mean field, i.e. the Coulomb potential of their total density (as opposed to the physically correct two-particle interaction). The central difficulty in actual realizations is the fact that there are only approximate formulations of the exchange-correlation potential, which are not capable of correctly representing all physical interactions and their consequences. In particular, the absence of electronic correlation in the independent-electron-picture could not be compensated up to now in any exchange-correlation functional.

2.1.5 *The Exchange-Correlation Functional*

The exchange-correlation functional $E_{xc}[\rho]$ is intended as a term that enables us to yield the exact electronic density from the minimization of the total energy functional. There is no closed expression up to now that fulfills this purpose, but there is a series of approximations that have turned out to generate ground-state electronic densities with a good accuracy. As all the unknowns in the theory are "packed" in this functional, the accuracy of a DFT calculations depends on the chosen approximation for $E_{xc}[\rho]$ [53, sec. 6.7].

The exchange-correlation contains the *kinetic correlation energy* (i.e. the difference in the kinetic energy of the real molecule and the non-interacting reference system), the *exchange energy* (which arises from the antisymmetry requirement for the wavefunction), the *Coulombic correlation energy* (associated with interelectronic repulsions) and a *self-interaction correction* (SIC) which compensates the error introduced in eq. (2.14), since an electron can interact with its own charge distribution.

The Local-Density Approximation

The simplest approximation to the exchange-correlation functional is the *Local-Density approximation* (LDA). This approximation was applied already in the seventies in a number of systems with slowly varying densities. It assumes that the energy functional depends solely on the value of the electronic density at each point in space. Then, if the density varies very slowly with position, the exchange-correlation functional can be written as

$$E_{xc}^{LDA}[\rho] = \int \rho(\mathbf{r})\epsilon_{xc}(\rho)\ \mathrm{d}^3r\ , \tag{2.24}$$

where $\epsilon_{xc}(\rho)$ is the exchange and correlation energy per electron in a HEG with electron density ρ. A potential $v_{xc}^{LDA}(\mathbf{r})$ can, then, be extracted by taking the functional derivative with respect to $\rho(\mathbf{r})$:

$$v_{xc}^{LDA}(\mathbf{r}) = \frac{\delta E_{xc}^{LDA}[\rho(\mathbf{r})]}{\delta\rho(\mathbf{r})} = \epsilon_{xc}(\rho(\mathbf{r})) + \rho(\mathbf{r})\frac{\delta\epsilon_{xc}(\rho(\mathbf{r}))}{\delta\rho(\mathbf{r})}\ . \tag{2.25}$$

Now, the KS equations eq. (2.22) can be self-consistently solved using this potential.

The most successful local approximations are those that have been derived from the HEG model, which are then applied to realistic systems (molecules and solids).

It can be shown [87] that $\epsilon_{xc}(\rho)$ can be written as the sum of exchange and correlation parts:

$$\epsilon_{xc}(\rho) = \epsilon_x(\rho) + \epsilon_c(\rho)\ , \tag{2.26}$$

where $\epsilon_c(\rho)$ is the correlation energy per electron in a HEG, and $\epsilon_x(\rho)$ is the exchange energy, which for the HEG is analytically known to be

$$\epsilon_x(\rho) = -\frac{3}{4}\left(\frac{3}{\pi}\right)^{\frac{1}{3}} \rho^{\frac{1}{3}} \ . \qquad (2.27)$$

The complete derivation of these results can be found for instance in [87, sec. 7.4], precise values for $\epsilon_c(\rho)$ from a Monte-Carlo simulations can be found in [14].

This approximation is very successful in many condensed phase systems, but LDA results are less accurate in atomic and molecular cases, and where hydrogen bonds are present.

Gradient-corrected functionals and the BLYP functional

The local density approximation is built on the basis of the HEG. Therefore, molecular and supramolecular systems with strongly oscillating densities may fall out of its range of validity. In particular, the effect of electron correlation, which is non-local, cannot be formulated with a local functional of the density.

In order to improve the local density approximation, various types of correction have been proposed, which often mainly address this problem of locality. In particular, the class of gradient-corrected (GC) functionals employs the gradient of the electronic density as a first step towards non-locality. It turns out that this Ansatz can significantly increase the accuracy of DFT.

The general formulation starts with the generalized gradient approximation (GGA):

$$E_{xc}^{GGA}[\rho, \nabla\rho] \;=\; \int \epsilon_{xc}(\rho(\mathbf{r}), \nabla\rho(\mathbf{r}))\ \rho(\mathbf{r})\ \mathrm{d}^3 r \ . \qquad (2.28)$$

This integral is further decomposed into its individual exchange and correlation contributions according to eq. (2.26). One particularly successful exchange functional has been proposed by Becke in 1988 (B88) [7], which reads

$$E_x^{B88}[\rho, \nabla\rho] = E_x^{LDA}[\rho] - b \int \frac{\rho(\mathbf{r})^{\frac{4}{3}} \chi[\rho]^2}{1 + 6b\chi[\rho] \sinh^{-1} \chi[\rho]} \, d^3r \ , \tag{2.29}$$

with $\chi[\rho] = |\nabla\rho(\mathbf{r})| / \rho(\mathbf{r})^{\frac{4}{3}}$ and b=0.0042 au. The value of b was obtained by fitting to the known Hartree-Fock exchange energies of several atoms.

This exchange functional can be combined with a correlation energy functional. In this work, the expression developed by Lee, Yang and Parr (LYP) [63] is used primarily. The combination of the Becke formula for exchange and the LYP term for correlation is denoted BLYP. It reads:

$$\begin{aligned} \epsilon_{xc}[\rho(\mathbf{r}), \nabla\rho(\mathbf{r})] = &- \left(C_X + b \tfrac{\chi[\rho]^2}{1+6b \sinh^{-1} \chi[\rho]} \right) \rho(\mathbf{r})^{1/3} \\ &- a \tfrac{1+f\,\rho(\mathbf{r})^{-5/3} \left(C_F\,\rho(\mathbf{r})^{5/3} - 2\frac{1}{9} t_W[\rho(\mathbf{r})] + \frac{1}{18} \nabla^2 \rho(\mathbf{r}) \right) e^{-c\,\rho(\mathbf{r})^{-1/3}}}{1+d\,\rho(\mathbf{r})^{-1/3}} \end{aligned} \tag{2.30}$$

where

$$t_W[\rho] = \frac{1}{8} \frac{|\nabla\rho(\mathbf{r})|^2}{\rho(\mathbf{r})} - \frac{1}{8} \nabla^2 \rho(\mathbf{r}) \ , \tag{2.31}$$

$\chi[\rho]$ is defined as in eq. (2.29), and the parameters C_X, C_F, a, b, c, d and f are chosen a way such that they fit the known exchange-correlation energy of selected atoms in their ground state [63].

2.1.6 *Basis Sets*

In order to perform numerical calculations within KS-DFT, the electronic orbitals must be expressed in a basis of suitable functions. The choice of this basis set has an important impact on both the amount of necessary computational resources and on the accuracy of the results. For this work, two kind of basis sets will be introduced; the *localized basis sets* and *position independent basis sets*, specifically plane waves (PW).

Localized basis sets are derived from atomic wavefunctions which are centered at the coordinate of the respective atom. These basis functions are typically products of Gaussian or exponential functions with spherical harmonics functions. In contrast, PWs are fully delocalized in space and do not depend on the positions of the atoms. They can be considered as the solutions of the Schrödinger equation for a free particle in a box under periodic boundary conditions.

Localized basis sets

Localized basis sets are composed of functions centered at each of the atoms of a system. They reflect the observation that electronic orbitals are often of finite support in space and decay quickly with the distance from their orbital center. Such basis functions can be realized with different function types. One very natural choice for this is exponential functions, also called *Slater-type orbitals* (STOs). They are based on the exact solutions of the Schrödinger equation for the isolated hydrogen atom. The functional form of the STOs is

$$\chi_{nlm}(r,\theta,\phi) = \mathcal{N} r^{n-1} e^{-\zeta r} Y_l^m(\theta,\phi) \ , \tag{2.32}$$

where Y_l^m are spherical harmonics, n, l, and m are integers (the quantum numbers of the original isolated hydrogen atom problem), ζ is a constant (related to the effective charge of the nucleus) and $\mathcal{N}$ is a normalization constant. The variables r, θ and ϕ are spherical coordinates measured from the nucleus under consideration. Although this basis set is appropriate from the physical point of view, alternative functions are typically used in order to ease the numerical calculation of spacial integrals.

An alternative class of functions is that of *Gaussian-type functions* (GTFs). The main advantage of using this class of functions as basis set is that a product of any two GTFs can be expressed as a single Gaussian function. This property is commonly exploited for the numerical calculation of the different elements of the Hamilton operator. GTFs are defined as

$$g_{ijk}(\mathbf{r}) = \mathcal{N} x^i y^j z^k e^{-\alpha r^2} \ , \tag{2.33}$$

where i, j, k are nonnegative integers, $\mathcal{N}$ is the normalization constant, α is a positive orbital exponent and $\mathbf{r} = (x, y, z)$ are Cartesian coordinates with the origin at the nucleus under consideration. In practice, a basis function is usually taken as a linear combination of several GTFs, forming a *contracted Gaussian-type function* (CGTF):

$$\chi_a = \sum_b d_{ab} g_b \ , \tag{2.34}$$

where g_b are the functions in eq. (2.33), with different α values and centered on the same atom, and the d_{ab} are *contraction coefficients*. The upper bound of the sum depends on the particular contraction elected for the basis set, laying typically between 1 and 7. The idea behind such a contraction is to approximate the natural exponential shape of atomic orbitals in a more accurate way.

Approximate STOs can be constructed from these contractions. The optimal values of the contraction coefficients d_{ab} and the orbital exponent α can be obtained by fitting CGTFs to a

STOs or by finding the CGTFs that minimize the self-consistent-field (SCF) energies of certain atoms. These optimized d_{ab} and α values are stored in the simulation code as constants.

Plane Waves (PW)

Plane wave functions are the solution to the Schrödinger equation for a free particle. They have the form

$$\psi_{\mathbf{G}}(\mathbf{r}) = \mathcal{N} \exp\left[i\mathbf{G} \cdot \mathbf{r}\right] , \tag{2.35}$$

with the normalization constant $\mathcal{N} = 1/\sqrt{\Omega}$, where Ω is the volume of the unit cell. The vectors **G** are the reciprocal lattice vectors, given by the periodicity of the crystal via

$$\mathbf{G}_{i,j,k} = \frac{2\pi}{a} \begin{pmatrix} i \\ j \\ k \end{pmatrix} , \tag{2.36}$$

with three integer numbers i, j, k and the lattice constant a.

Then, an electronic orbital in a periodic system can be expressed as:

$$\Psi(\mathbf{r}) = \frac{1}{\sqrt{\Omega}} \sum_{\mathbf{G}} \Psi(\mathbf{G}) \exp\left[i\mathbf{G} \cdot \mathbf{r}\right] . \tag{2.37}$$

With this definition, the periodicity condition $\Psi(\mathbf{r}) = \Psi(\mathbf{r} + \mathbf{L})$ is met (being $\mathbf{L} = i\hat{\mathrm{e}}_1 + j\hat{\mathrm{e}}_2 + k\hat{\mathrm{e}}_3$, where are i, j, k integers and $\hat{\mathrm{e}}_1, \hat{\mathrm{e}}_2, \hat{\mathrm{e}}_3$ are the lattice vectors).

According to *Bloch's theorem* [1], each solution $\phi_{i\mathbf{k}}(\mathbf{r})$ of the Schrödinger equation with periodic potential can be written as product of a phase factor and a periodic function $u_i(\mathbf{r}, \mathbf{k})$ with the periodicity of the lattice (the *Bloch function*),

$$\begin{aligned}\phi_{i\mathbf{k}}(\mathbf{r}) &= \exp\left[i\mathbf{k}\cdot\mathbf{r}\right] u_i(\mathbf{r},\mathbf{k}) \\ u_i(\mathbf{r},\mathbf{k}) &= u_i(\mathbf{r}+\mathbf{L},\mathbf{k})\ .\end{aligned} \tag{2.38}$$

The k vector belongs to the first Brillouin zone, characterized by $|\mathbf{k}| < 2\pi/a$, and i is the band index (see e.g. [1]). Applying this theorem to the periodic, non-interacting KS reference system yields KS orbitals of the form:

$$\theta_i^{KS}(\mathbf{r},\mathbf{k}) = \exp[i\mathbf{k}\cdot\mathbf{r}]u_i(\mathbf{r},\mathbf{k})\ . \tag{2.39}$$

The periodic function $u_i(\mathbf{r},\mathbf{k})$ can be expanded in plane waves as

$$u_i(\mathbf{r},\mathbf{k}) = \frac{1}{\sqrt{\Omega}}\sum_{\mathbf{G}} c_i(\mathbf{G},\mathbf{k})\exp[i\mathbf{G}\cdot\mathbf{r}]\ , \tag{2.40}$$

where $c_i(\mathbf{G},\mathbf{k})$ are the coefficients of the expansion of the KS orbitals in the PW basis set. This allows to write eq. (2.39) as

$$\theta_i^{KS}(\mathbf{r},\mathbf{k}) = \frac{1}{\sqrt{\Omega}}\sum_{\mathbf{G}} c_i(\mathbf{G},\mathbf{k})\exp[i(\mathbf{G}+\mathbf{k})\cdot\mathbf{r}]\ . \tag{2.41}$$

The summation over reciprocal lattice vectors is in practice truncated, and the truncation is done such that all vectors $\mathbf{G}$ up to a maximum norm are considered, $||\mathbf{k}+\mathbf{G}|| \leq G_{\text{max}}$. This upper limit is usually expressed in terms of the kinetic energy E_k of a plane wave with $||\mathbf{k}+\mathbf{G}|| = G_{\text{max}}$, given by

$$\frac{1}{2}||\mathbf{k}+\mathbf{G}||^2 \ \leq\ E_k\ . \tag{2.42}$$

The kinetic energy of a KS orbital expressed in a plane wave basis can then be obtained as:

$$\begin{aligned}T_i &= -\frac{1}{2}\langle\theta_i^{KS}|\nabla^2|\theta_i^{KS}\rangle \\ &= \frac{1}{2\Omega}\sum_{\mathbf{G}}||\mathbf{k}+\mathbf{G}||^2\ |c_i(\mathbf{G},\mathbf{k})|^2\ .\end{aligned} \tag{2.43}$$

It turns out that for large, non-metallic systems the usage of only one **k** value is sufficient ($\mathbf{k} = 0$, also called Γ-point). This approximation used throughout this work.

The main advantage of plane waves as basis set functions is that both the kinetic energy operator, eq. (2.43), and the Hartree operator are diagonal on this basis. This enables a very efficient calculation of these parts of the total KS energy functional. In contrast to this, the electronic density and the exchange-correlation potential, are formulated in direct space. Hence, a Fourier transformation of each KS orbital is required in order to compute them from the plane wave coefficients. In practice, Fast Fourier Transformation techniques are used in order to reduce the computational effort neccessary for these transformations.

2.1.7 *Pseudopotentials (PP)*

The electronic orbitals of an atom decay quickly with increasing distance to the atomic center. This is particularly true for atoms with higher nuclear charges (in practice for atoms with $Z \geq 3$), which have tightly bound electrons with large negative energy eigenvalues close to the nucleus. These electrons are called core electrons. The outer (valence) electrons have a slower decay, but the orthogonality requirement of the electronic states leads to valence orbitals which have large oscillations in the core region of the atoms. Both situations result in the computational problem that the number of plane waves required to correctly represent such orbitals increases very quickly with the atomic number. The most common solution to this problem is the use of *Pseudopotentials* (PP, also called effective core potentials).

The general idea can be traced back to the work of Hans Hellmann [33, 34] in the '30s, and is based on the observation that the core electrons hardly contribute to chemical bonds, in the sense that their orbitals do not change upon a change in the bonding situation of an atom. Only the outer part of the valence orbitals changes. Thus, it is possible to reproduce the chemical bonding behavior of an atom by replacing the nuclear potential and the core electrons by an effective potential that reproduces the shape of the valence orbitals in the bonding region. The orbital shape in the core region (in particular the strong oscillations caused by the orthogonality requirement) may change, but this deviation can be ignored because the core part of the orbitals does not contribute significantly to the chemical bonding properties.

Pseudopotentials have therefore to be designed to reproduce the original valence wavefunctions accurately outside of a given radius r_c. It is important that the PP remain as smooth as possible, in order to minimize the oscillations in the wavefunction for the valence electrons when $r < r_c$, and at the same time not compromising its accuracy on the $r > r_c$ region. In addition, the ability to reproduce the behavior of the valence electronic wavefunction in different chemical environments is a central goal in the development of PPs.

A particularly relevant type of PP are *Norm-conserving* pseudopotentials, whose defining property is that their valence wavefunctions integrate to the same charge in the core region as an all-electron calculation. These pseudopotentials V^{PP} have in general the following *non-local* form:

$$
\begin{aligned}
V^{PP}(\mathbf{r},\mathbf{r}') &= V^{\rm loc}(\mathbf{r})\,\delta(\mathbf{r}-\mathbf{r}') + \\
&+\sum_{l=0}^{l_{max}}\sum_{m=-l}^{m=l} Y^*_{lm}(\theta,\phi)V^{nl}_l(r)\frac{\delta(r-r')}{r^2}Y_{lm}(\theta',\phi')\ , \qquad (2.44)
\end{aligned}
$$

where $V^{nl}_l(r)$ and $V^{\rm loc}(\mathbf{r})$ are respectively the non-local and local parts of the potential, $r = ||\mathbf{r}||$, and l is the angular quantum momentum number. There are several possible expressions for $V^{nl}_l(r)$ and $V^{\rm loc}(\mathbf{r})$, for instance [26, 4, 31, 112, 51]. In this work, a slightly different type of effective core potentials is used. The pseudopotentials of Goedecker [26] are defined as

$$
\begin{aligned}
V^{\rm loc}(r) &= \frac{-Z_{ion}}{r}\,\mathbf{erf}\left(\frac{r}{\sqrt{2}r_{loc}}\right) + \exp\left[-\frac{1}{2}\left(\frac{r}{r_{loc}}\right)^2\right] \times \\
\times & \left[C_1 + C_2\left(\frac{r}{r_{loc}}\right)^2 + C_3\left(\frac{r}{r_{loc}}\right)^4 + C_4\left(\frac{r}{r_{loc}}\right)^6\right] , \qquad (2.45)
\end{aligned}
$$

and the non-local part as

$$
V^{nl}(\mathbf{r},\mathbf{r}') \;\propto\; p^l_m(r)p^l_m(r')\ , \qquad (2.46)
$$

with

$$
p^l_1(r) \;\propto\; \frac{r^l \exp\left[-\frac{1}{2}\left(\frac{r}{r_{loc}}\right)^2\right]}{r^{l+\frac{3}{2}}\sqrt{\Gamma(l+\frac{3}{2})}} \qquad (2.47)
$$

$$
p^l_2(r) \;\propto\; \frac{r^{(l+2)} \exp\left[-\frac{1}{2}\left(\frac{r}{r_{loc}}\right)^2\right]}{r^{l+\frac{7}{2}}\sqrt{\Gamma(l+\frac{7}{2})}}\ , \qquad (2.48)
$$

where Z_{ion} is the ionic charge of the core, $\Gamma(x)$ is the gamma function, r_{loc} is the range of the potential and the constants

$C_1, \dots, C_4$ are determined from all-electron reference calculations [91]. The functions $p^l_m(r)$ comply with $1 = \int_0^\infty p^l_m(r) p^l_m(r) r^2 \mathrm{d}r$.

2.1.8 *Mixed Gaussian and Plane Waves Method*

The use of either plane waves or localized basis sets carries some drawbacks along with their advantages. For instance, using localized basis sets for describing the electronic wavefunction in the core of the atom is a very natural choice, while the use of PWs has the disadvantage that the size of the basis set necessary for this task increases quickly with the atomic number. On the other side, the calculation of the Hartree term in eq. (2.22) under periodic boundary conditions is more straightforward in PWs, while GTFs scale more unfavorably with the system size. In addition, the physical interpretation of electron orbitals in terms of PWs is not as straightforward as with localized basis sets.

The Mixed Gaussian and Plane Waves (GPW) Method [67, 120] tries to combine both basis sets to obtain the advantages of each approach.

The derivation of the method goes as follows. The density ρ can be expressed in the basis $\{\phi_i\}$ as

$$\rho(\mathbf{r}) = \sum_{\mu,\nu} P^{\mu\nu} \phi_\mu(\mathbf{r}) \phi^*_\nu(\mathbf{r}) \; , \tag{2.49}$$

where $P^{\mu\nu}$ are the density matrix elements. In the PWs basis set, this is expressed as

$$\rho(\mathbf{r}) = \frac{1}{\Omega} \sum_{\mathbf{G}} \rho(\mathbf{G}) \exp\left(i\mathbf{G} \cdot \mathbf{r}\right) \; . \tag{2.50}$$

Again, Ω is the volume of the unit cell, $\mathbf{G}$ are the reciprocal lattice vectors. The KS DFT energy becomes under this representation:

$$
\begin{aligned}
E_v[\rho] &= E_T[\rho] + E_V[\rho] + E_H[\rho] + E_{xc}[\rho] + E_{II} && (2.51)\\
&= \sum_{\mu,\nu} P^{\mu\nu} \langle \phi_\mu(\mathbf{r})| - \frac{1}{2}\nabla^2 |\phi_\nu(\mathbf{r})\rangle + && (2.52)\\
& \quad + \sum_{\mu,\nu} P^{\mu\nu} \langle \phi_\mu(\mathbf{r})| V^{\mathrm{loc}}(r) |\phi_\nu(\mathbf{r})\rangle + && (2.53)\\
& \quad + \sum_{\mu,\nu} P^{\mu\nu} \langle \phi_\mu(\mathbf{r})| V^{nl}(\mathbf{r},\mathbf{r}') |\phi_\nu(\mathbf{r}')\rangle + && (2.54)\\
& \quad + 2\pi\Omega \sum_{\mathbf{G}} \frac{\rho^*(\mathbf{G})\rho(\mathbf{G})}{\mathbf{G}^2} + && (2.55)\\
& \quad + \int \epsilon_{xc}(\mathbf{r}) d\mathbf{r} + && (2.56)\\
& \quad + \frac{1}{2} \sum_{I \neq J} \frac{Z_I Z_J}{|\mathbf{R}_I - \mathbf{R}_J|}\ . && (2.57)
\end{aligned}
$$

Here, $E_T[\rho]$ is the electronic kinetic energy, $E_V[\rho]$ is the electronic interaction with the ionic cores, $E_H[\rho]$ is the electronic Hartree energy, $E_{xc}[\rho]$ is the exchange-correlation energy and E_{II} is the interaction energy of the ionic cores, which in turn have charges Z_A and positions $\mathbf{R}_A$. V^{loc} and V^{nl} are as defined in sec. 2.1.7.

In addition to eq. (2.16), the interaction energy of the ionic cores (eq. (2.57)) has been added. Also the external potential $v(\mathbf{r})$ has been split in the local (eq. (2.53)) and non-local (eq. 2.54) contributions of the pseudopotential[2]. Finally, the major advantage of the GPW method is in the Hartree energy term (eq. (2.55)), which is now expressed in the reciprocal space:

---

[2] (see sec. 2.1.7)

It can be calculated now as

$$v_H(\mathbf{G}) = \frac{4\pi\rho_{\text{tot}}(\mathbf{G})}{\mathbf{G}^2}\,, \tag{2.58}$$

with $\rho_{\text{tot}}(\mathbf{G}) = \rho(\mathbf{G}) + \rho_c(\mathbf{G})$, where $\rho_c(\mathbf{G})$ is the nuclear charge density. The real-space potential is then obtained by a Fourier transformation.

In summary, this method eliminates the main bottleneck of Gaussian basis sets under periodic boundary conditions by calculating the Hartree term in the reciprocal space, using a plane-waves representation. The price payed for it is the need to store both representations at the same time.

2.2 *Ab-initio* Molecular Dynamics Simulations

Molecular Dynamics (MD) is a well established technique to compute the equilibrium and transport properties of *classical* many-body systems. The word *"Classical"*, as used in this context, means that the particles involved in the calculation are governed by classical mechanics.

The idea of MD simulations is to calculate the dynamics of atoms, which interact through their potentials. At this level, many possible approaches can be taken on how to describe the interatomic interactions in order to calculate the trajectories of the nuclei accurately and with a reasonable computational cost. The usual approach for most systems where quantum effects are not important is to parametrize effective potentials in advance from more accurate calculations of isolated monomers, for instance from DFT, and then employ them in the calculation of the dynamics of the system. This approach of parametrized *force-fields* molecular dynamics allows the study of relatively large systems, like those found in biological problems.

The present work uses an alternative approach to MD, where the potential energy surface (PES) is directly obtained from electronic structure calculations, instead of using a parametrized force field. The methods following this approach are called *ab-initio* or *first-principles* MD (FPMD). This kind of methods involve the calculation of the interatomic forces by explicitly solving the quantum electronic problem. These forces, of quantum and electrostatic origin, are used to calculate the dynamics of the classically described nuclei.

The family of *ab-initio* MD comes in several flavors as well. One can typically think of three different levels [74]. First, *Ehrenfest Molecular Dynamics*, in which the classical equations of motion and the Schrödinger equation for the electrons are solved simultaneously. This leads to huge computational demands, which make this technique unfeasible for many problems of interest. This flavor of FPMD is not used in this work.

Born-Oppenheimer Molecular dynamics (BOMD), in turn, uses the Born-Oppenheimer approximation (sec. 2.1.2), which establishes two different and decoupled timescales in the system: one corresponding to the nuclei and the other to the electrons. Therefore, the Schrödinger equation for the electrons is solved with fixed nuclei, as if it were a static problem. Afterwards, the equations of motion for the nuclei moving in the PES generated by the electrons is solved. This separation allows for the solution of much larger timesteps (the time segment to which the dynamics of the system is solved in each iteration of the simulation) than *Ehrenfest MD*. The calculations in chapter 4 are based on this method, which is presented in sec. 2.2.1.

Car-Parrinello Molecular Dynamics [12] goes one step further in the simplification of the problem, by avoiding the explicit solution of the Schrödinger equation in each step. Instead, the electron orbitals are treated as fictitious particles and their dynamics evolve with their own equations of motion for a number of steps. Most calculations in chapter 3 are based on this method, which presented in sec. 2.2.2.

2.2.1 *Born-Oppenheimer Molecular Dynamics*

As stated in the introduction, *Born-Oppenheimer Molecular dynamics* (BOMD) owes its name to the use of the Born-Oppenheimer approximation (sec. 2.1.2) as its basic Ansatz. The dynamics is split into the static electronic structure problem and the molecular dynamics problem of the nuclei. In addition, a second approximation is applied: the nuclei are treated as classical particles.

Each step of a BOMD calculation consists in solving the Schrödinger equation for the electrons (in this work using the KS method, sec. 2.1.4), followed by the calculation of forces exerted on the nuclei from the electrons and the other nuclei. Finally, an integration of the nuclear dynamics from these forces follows. The method is defined by the equations of motion:

$$\begin{aligned} M_I \ddot{\mathbf{R}}_I &= \mathbf{F}_I && (2.59) \\ &= -\nabla_I \min_{\Psi}\{\langle\Psi|\mathcal{H}^{\mathrm{el}}|\Psi\rangle\} && (2.60) \\ &= -\nabla_I \min_{\rho}\{E_v[\rho]\} \,, && (2.61) \end{aligned}$$

where the electronic Hamiltonian $\mathcal{H}^{el}$ depends on the position of the nuclei (see definition in eq. (2.8)). The electrostatic force exerted on the nuclei by the electrons (eq. (2.59)) is calculated from the electron density obtained from electronic structure calculations (eq. (2.60)), in particular for this work via DFT (eq. (2.61)). The classical equations of motion for the nuclei are then defined with the addition of the electrostatic forces of the other ions.

The computational bottleneck in this approach is the optimization of the electronic wavefunction in each step. Enhancements of this method are made precisely by predicting the evolution of the ground state wavefunction in order to avoid its explicit calculation on each step. One successful example of this optimization is Car-Parrinello Molecular Dynamics (CPMD), which is presented in next section. Many other algorithmic optimizations can also be used in order to improve convergence. In particular, details of the implementation of the QUICKSTEP module for the `CP2K` code, which is the computational code used for the calculations of chapter 4, can be found in [120].

2.2.2 *Car-Parrinello Molecular Dynamics (CPMD)*

The basic idea of the Car-Parrinello approach [12, 74] is to postulate a fictitious Newtonian-like dynamics of the electron orbitals, such that the evolution timescale in the dynamics of both nuclear and electronic degrees of freedom is similar.

The equations of motion that the fictitious orbital "particles" follow are derived from a Lagrangian formulation of the system. In classical mechanics, the force on the nuclei is the opposite of the gradient of the potential energy with respect to the nuclear positions. Then, a suitable Lagrangian can be designed such that the functional derivative with respect to the orbitals results in the force exerted on the nuclei by the electrons [12]. This is met by the Lagrangian

$$\begin{aligned}\mathcal{L}_{CP} &= \underbrace{\sum_I \frac{1}{2} M_I \ddot{\mathbf{R}}_I^2 + \sum_i \mu \langle \dot{\psi}_i | \dot{\psi}_i \rangle}_{\text{kinetic energy}} - \underbrace{\langle \Psi_0 | \mathcal{H}^{el} | \Psi_0 \rangle}_{\text{potential energy}} + \\ &+ \text{ orthonormality constraints (o.c.)} \quad , \end{aligned} \tag{2.62}$$

Where μ is a free parameter (see below), $\mathcal{H}_{el}$ is the electronic Hamiltonian, ψ_i are one electron orbitals, M_I and $\mathbf{R}_I$ are the mass and position of nuclei I, respectively, and Ψ_0 is the ground-state electronic wavefunction. Here, Ψ_0 is assumed to be a linear combination of Slater determinants using the one-particle orbitals ψ_i, in this case KS orbitals. The parameter μ is called the "fictitious mass" of the electron orbitals, since it acts as an inertia parameter. A third term is added to account for the constrains imposed in the orbitals, in particular their orthonormality. The corresponding Euler-Lagrange equations derived from this Lagrangian read

$$\begin{aligned}\frac{\mathrm{d}}{\mathrm{d}t}\frac{\partial \mathcal{L}}{\partial \dot{\mathbf{R}}_I} &= \frac{\partial \mathcal{L}}{\partial \mathbf{R}_I} \\ \frac{\mathrm{d}}{\mathrm{d}t}\frac{\delta \mathcal{L}}{\delta \langle \dot{\psi}_i |} &= \frac{\delta \mathcal{L}}{\delta \langle \psi_i |} \, , \end{aligned} \tag{2.63}$$

which leads to the Newtonian equations:

$$\begin{aligned} M_I \ddot{\mathbf{R}}_I(t) &= -\frac{\partial}{\partial \mathbf{R}_I} \langle \Psi_0 | \mathcal{H}^{el} | \Psi_0 \rangle + \frac{\partial}{\partial \mathbf{R}_I} (\text{o.c.}) \\ \mu_i \ddot{\psi}_i(t) &= -\frac{\delta}{\delta \langle \psi_i |} \langle \Psi_0 | \mathcal{H}^{el} | \Psi_0 \rangle + \frac{\delta}{\delta \langle \psi_i |} (\text{o.c.}) \, . \end{aligned} \tag{2.64}$$

These quasi-classical equations of motion can be solved to get the trajectory of the nuclei and the fictitious particles. Notice that a full optimization of the electronic wavefunctions should be done once after a number of steps in order to periodically correct the errors that can eventually lead the system far from the instantaneous ground state. How often this full calculation must be done depends on the choice of the fictitious mass μ, along with the properties of the particular system. μ is to be chosen freely along with the timestep length to tune the accuracy and computational cost of a calculation. Another important issue involved in the loss of accuracy of a calculation with this method is the necessity to maintain the energy contributions from the electronic orbitals decoupled from those of the atomic nuclei, otherwise the BO approximation would be rendered invalid. If this decoupling must be enforced, a thermostat (sec. 2.2.3) can be attached to the electrons in order to release the energy acquired from the other degrees of freedom in the system.

The statistical behavior of BOMD and CPMD are equivalent [60, 96], which means that both methods are similarly useful to study the statistical properties of a system, although the forces and trajectories generated by each method may differ [111].

2.2.3 *The Nosé-Hoover Thermostat*

In order to generate an NVT ensemble, that is, to perform simulations at constant temperature, a modification of the system must be introduced to account for the effect of a thermal bath. This is called a *thermostat*. In this work, the Nosé-Hoover thermostat was used [81].

The idea behind the Nosé-Hoover Thermostat is to add a certain degrees of freedom to the system to represent the reservoirs characterising a desired NVT ensemble. This *extended* system is governed by a Hamiltonian such that the generated phase-space trajectories of the *real* variables in the extended system are equivalent to those of the real system in the desired ensemble.

The system is extended by introducing a rescaling of the time, via the additional variable s,

$$\mathrm{d}t = s\mathrm{d}t' \ . \tag{2.65}$$

The introduction of this additional variable produces also a rescaling of the momentum in the extended system, via $p_i' = s \cdot p_i$ (the primed variables correspond to the extended system).

The corresponding extended Hamiltonian, as postulated by Nosé, reads

$$\mathcal{H} = \sum_i \frac{p_i'^2}{2ms^2} + \sum_i \frac{p_s^2}{2Q} + V(\{\mathbf{R}_I\}) + \frac{3N+1}{\beta} \log s \ , \tag{2.66}$$

where $V(\{\mathbf{R}_I\})$ is the potential energy of the system, which depends on all the coordinates $\mathbf{R}_I$ of all the nuclei, Q is the fictitious "mass" of the thermostat, N is the number of atoms in the system, $1/\beta = k_B T$ is the thermal energy, p_i is the momentum of of particle i, and p_s is the "momentum" of the thermostat (the conjugate variable of s).

By writing each momentum as $p_i = p_i'/s$, the partition function of the system can be expressed back in the real variables, as

$$\begin{aligned} \mathcal{Z} &= \frac{1}{N} \int \mathrm{d}p_s \mathrm{d}s \mathrm{d}p_1' \cdots \mathrm{d}p_N' \mathrm{d}r_1 \cdots \mathrm{d}r_N \delta\left(\mathcal{H} - E\right) && (2.67) \\ &= \frac{1}{N} \int \mathrm{d}p_s \mathrm{d}s \mathrm{d}p_1 \cdots \mathrm{d}p_N \mathrm{d}r_1 \cdots \mathrm{d}r_N \times \\ &\quad \times \delta\left(\mathcal{H}_0 + \frac{p_s^2}{2Q} + \frac{3N+1}{\beta} \log s - E\right) \ , && (2.68) \end{aligned}$$

where E is the energy of the extended system and $\mathcal{H}_0$ is the real Hamiltonian. Using the property of Dirac's delta, $\delta(f(x)) = \delta(x - x_0)/|f'(x)|_{x \to x_0}$ (with $f(x_0) = 0$), the partition function can be expressed as

$$\begin{aligned} \mathcal{Z} &= \frac{1}{N!} \int \mathrm{d}p_s \mathrm{d}s \mathrm{d}p'_1 \cdots \mathrm{d}p'_N \mathrm{d}r_1 \cdots \mathrm{d}r_N s^{3N} \frac{\beta}{3N+1} \times \\ & \quad \times \exp\left[-\frac{\beta}{3N+1} \mathcal{H}_0 + \frac{p^2}{2Q} - E \right] \qquad (2.69) \\ &= \frac{\beta e^{\beta E/(3N+1)}}{N!} \left(\frac{2Q\pi}{\beta} \right)^{\frac{1}{2}} \times \qquad (2.70) \\ & \quad \int \mathrm{d}p_1 \cdots \mathrm{d}p_N \mathrm{d}r_1 \cdots \mathrm{d}r_N \exp\left[-\beta \mathcal{H}_0 \right] \; . \qquad (2.71) \end{aligned}$$

This means that the partition function of the real system is obtained (up to a constant prefactor) from the integration over the extended variables s and p_s of the partition function corresponding to the extended system. In this way, a canonical ensemble average can be obtained from the microcanonical ensemble of an extended system.

2.2.4 *Accelerated BOMD and Langevin dynamics*

A novel method to provide efficient and accurate Born-Oppenheimer dynamics, developed by Kühne et. al in 2007 [59], is extensively used in sec. 4. The method consists in predicting the density matrix of the system from the previous integration steps in order to avoid the need of a full self-consistent-field (SCF) optimization, thus being a new alternative to CPMD simulations.

Consider a set of M KS orbitals, and take the lowest N occupied orbitals. From this subset of orbitals, we can define an overlap matrix $C \in R^{M\times N}$, which is a subset of the overlap matrix $S \in R^{M\times M}$. The corresponding density matrix of this subset is, then, $P = CC^T$. Now, suppose a number n of steps have already been calculated by the standard BOMD method (sec. 2.2.1), and the last K matrices C have been kept stored, that is, $C(t_{n-1})\dots C(t_{n-K-1})$ with $n > K+1$. Then, a predictor-corrector method can be taken to estimate the next C matrix. In particular, using the always stable predictor (ASPC) method [55], the matrix $C(t_n)$ can be estimated via:

$$C^p(t_n) \approx \sum_{m=1}^{K}(-1)^{m+1} m \frac{\binom{2K}{K-m}}{\binom{2K-2}{K-1}} C(t_{n-m})C^T(t_{n-m})S(t_{n-m})C(t_{n-1}) \ , \tag{2.72}$$

where the superindex p denotes that this is the predictor step of the ASPC method. The matrix C was approximated by CC^TS, because this evolves more smoothly than C [59]. Afterwards, a corrector step must be applied to minimize the deviation from the ground state. This is done with the corrector

$$C(t_n) = \omega \mathrm{Min}[C^p(t_n)] + (1-\omega)C^p(t_n) \ , \tag{2.73}$$

where $\omega = K/(2K-1)$, a value chosen for generating a stable relaxation [59], and the Min function denotes one single SCF minimization step. The obtained density matrix CC^T is then used for all calculations as if it were obtained from a full SCF optimization.

Langevin Dynamics

In practice, the method explained previously is dissipative. This drawback is however overcome by applying the accelerated BOMD method within the framework of Langevin Dynamics [105].

Langevin Dynamics is an alternative approach for modeling the dynamics of molecular systems. In this approach certain degrees of freedom can be omitted with the use of stochastic differential equations.

Given a system with N particles of mass M_I and coordinates $\mathbf{R}_I(t)$, the Langevin equations read

$$M_I\ddot{\mathbf{R}}_I = \mathbf{F}_I^{BO} - \gamma_L M_I \dot{\mathbf{R}}_I + \Xi(t) \tag{2.74}$$

where $\mathbf{F}_I^{BO} \equiv -\nabla_I U(\{\mathbf{R}_I\})$ is the force over particle I calculated from the particle interaction potentials, γ_L is the Langevin friction constant (a free parameter), M_I is the mass of the particle I and $\Xi(t)$ is a random force (white noise), which holds the following properties:

$$\begin{aligned} \langle \Xi(t) \rangle &= 0 && (2.75) \\ \langle \Xi(t)\Xi(t') \rangle &\propto \delta(t-t') \ . && (2.76) \end{aligned}$$

To guarantee an accurate sampling of the Boltzmann distribution, the noise has to obey the fluctuation-dissipation theorem:

$$\langle \Xi_I(0)\Xi_I(t) \rangle = 6(\gamma_D + \gamma_L) M_I k_B T \delta(t), \tag{2.77}$$

where k_B is the Boltzmann constant and T is the system temperature.

When using a predictor-corrector (PC) method, the forces $\mathbf{F}_I^{PC}$ arising from the method can be expressed as $\mathbf{F}_I^{PC} = \mathbf{F}_I^{BO} - \gamma_D M_I \dot{\mathbf{R}}_I$, where γ_D is a constant that must be chosen to obtain the desired temperature. The equation (2.74) can then be finally rewritten as

$$M_I\ddot{\mathbf{R}}_I = \mathbf{F}_{BO} - (\gamma_L + \gamma_D) M_I \dot{\mathbf{R}}_I + \Xi_I(t) \ . \tag{2.78}$$

When a simulation is being carried on, one must take care that there is no relevant temperature drift. The γ constants should be tuned to guarantee a constant the temperature, in a similar way to the tuning of the fictitious mass μ for the conservation of energy in the Car-Parrinello scheme.

2.3 Path Integral Molecular Dynamics (PIMD)

The basic principles of the formulation of quantum statistical mechanics in terms of path integrals were developed by Richard Feynman in 1948 [22] as an alternative formulation of non-relativistic quantum mechanics. This representation is vowed not only for its elegance but also for its convenience for numerical calculations, since this representation fits perfectly for parallel computation (in comparison to other approaches, where the intrinsic non-locality of quantum mechanics produce a prohibitive scaling of the computing time with the number of parallel nodes). The formulation has also the big advantage of allowing a "modular" implementation; it can be used within the framework of established simulation methods, like Monte Carlo [115], CPMD or BOMD [75, 116], with a small implementation overhead.

This method has even been successfully used to study inherently quantum properties like superfluidity, in a work carried on by Ceperley for the description of condensed helium [13].

2.3.1 *Derivation of the Formalism*

One quantum particle

The definition of the partition function for a system of a single quantum particle is

$$\mathcal{Z} \equiv \mathcal{Z}(N, V, T) = \mathrm{Tr}\left[\mathrm{e}^{-\beta\mathcal{H}}\right] \ , \tag{2.79}$$

with $\beta = \frac{1}{k_B T}$. This can be expanded in the position basis $|\mathbf{R}\rangle$,

$$\mathcal{Z} = \int \mathrm{d}\mathbf{R} \ \langle\mathbf{R}|\mathrm{e}^{-\beta\mathcal{H}}|\mathbf{R}\rangle \ . \tag{2.80}$$

Given that the kinetic energy operator $\hat{T}$ and potential energy operator $\hat{V}$ do not commute,

$$[\hat{\mathcal{T}}, \hat{\mathcal{V}}] \neq 0 \tag{2.81}$$

the exponential term in eq. (2.79) cannot be separated in factors, unless the Trotter-Suzuki (TZ) expansion is used:

$$\mathrm{e}^{\lambda(A+B)} = \lim_{P\to\infty}\left[\mathrm{e}^{\lambda B/(2P)}\mathrm{e}^{\lambda A/P}\mathrm{e}^{\lambda B/(2P)}\right]^P \ , \tag{2.82}$$

where A, B are any matrices, and λ an arbitrary number. Using this expansion, eq. (2.80) can be written as

$$\mathcal{Z} = \lim_{P\to\infty}\int \mathrm{d}\mathbf{R} \ \langle\mathbf{R}|\Omega^P|\mathbf{R}\rangle \ , \tag{2.83}$$

where the operator Ω is defined as

$$\Omega = \mathrm{e}^{-\beta\hat{\mathcal{V}}/(2P)}\mathrm{e}^{-\beta\hat{\mathcal{T}}/P}\mathrm{e}^{-\beta\hat{\mathcal{V}}/(2P)} \ . \ , \tag{2.84}$$

Inserting $P-1$ times the identity in the following way:

$$\Omega^P = \Omega I_1 \Omega I_2 \cdots \Omega I_{P-1}\Omega \ , \tag{2.85}$$

and then expanding the following definition of the identity:

$$I_i = \int \mathrm{d}\mathbf{R}_i |\mathbf{R}_i\rangle\langle\mathbf{R}_i| \ , \tag{2.86}$$

the integrand of eq. (2.83) can be expanded as

$$\begin{aligned}\langle\mathbf{R}_1|\Omega^P|\mathbf{R}_1\rangle =& \int \mathrm{d}\mathbf{R}_1 \cdots \mathrm{d}\mathbf{R}_P \ \langle\mathbf{R}_1|\Omega|\mathbf{R}_2\rangle\times \\ & \times \ \langle\mathbf{R}_2|\Omega|\mathbf{R}_3\rangle\langle\mathbf{R}_3|\cdots|\mathbf{R}_P\rangle\langle\mathbf{R}_P|\Omega|\mathbf{R}_1\rangle \\ =& \int \mathrm{d}\mathbf{R}_1 \cdots \mathrm{d}\mathbf{R}_P \ \prod_{i=1}^{P}\langle\mathbf{R}_i|\Omega|\mathbf{R}_{i+1}\rangle\Big|_{\mathbf{R}_1=\mathbf{R}_{P+1}} ,\end{aligned} \tag{2.87}$$

where $\{|\mathbf{R}_i\rangle\}$ are elements of the position basis set. They correspond to the same physical particle, but their integration is independent. In effect, it can be thought as corresponding to different *images* or *replicas* of the same particle. Evaluating each term in the product yields

$$\begin{aligned}\langle\mathbf{R}_i|\Omega|\mathbf{R}_{i+1}\rangle =& \langle\mathbf{R}_i|\mathrm{e}^{-\beta\hat{\mathcal{V}}/(2P)}\mathrm{e}^{-\beta\hat{p}^2/(2mP)}\mathrm{e}^{-\beta\hat{\mathcal{V}}/(2P)}|\mathbf{R}_{i+1}\rangle \\ =& \mathrm{e}^{-\beta(V(\mathbf{R}_i)+V(\mathbf{R}_{i+1}))/(2P)}\langle\mathbf{R}_i|\mathrm{e}^{-\beta\hat{p}^2/(2mP)}|\mathbf{R}_{i+1}\rangle \ ,\end{aligned} \tag{2.88}$$

where m is the mass of the particle. This integral is solved by using the expansion of the identity in the form

$$I = \int \mathrm{d}p \ |p\rangle\langle p| \ , \tag{2.89}$$

thus the remaining operator elements can be calculated as

$$\begin{aligned}\langle\mathbf{R}_i|\mathrm{e}^{-\beta\hat{p}^2/(2mP)}|\mathbf{R}_{i+1}\rangle =& \int \mathrm{d}p \ \langle\mathbf{R}_i|p\rangle\langle p|\mathrm{e}^{-\beta\hat{p}^2/(2mP)}|\mathbf{R}_{i+1}\rangle \\ =& \int \mathrm{d}p \ \langle\mathbf{R}_i|p\rangle\langle p|\mathbf{R}_{i+1}\rangle \ \mathrm{e}^{-\beta p^2/(2mP)} \ ,\end{aligned} \tag{2.90}$$

where p and R are the momentum and position associated to the states $|p\rangle$ and $|R\rangle$, respectively.

The projection of the momentum eigenstates on the position basis is

$$\langle \mathbf{R}|p\rangle = \frac{1}{\sqrt{2\pi}}\, \mathrm{e}^{ipR}\ . \tag{2.91}$$

This can be used to calculate the integral in eq. (2.90), yielding

$$\langle \mathbf{R}_i|\mathrm{e}^{-\beta\hat{p}^2/(2mP)}|\mathbf{R}_{i+1}\rangle = \left(\frac{mP}{2\pi\beta}\right)^{1/2} \times \tag{2.92}$$

$$\times \exp\left[-\frac{mP}{2\beta}(\mathbf{R}_{i+1} - \mathbf{R}_i)^2\right]\ . \tag{2.93}$$

Using this result, the partition function in eq. (2.83) takes the form

$$\mathcal{Z} = \lim_{P\to\infty} \left(\frac{mP}{2\pi\beta}\right)^{P/2} \int \mathrm{d}\mathbf{R}_1 \cdots \mathrm{d}\mathbf{R}_P \times$$

$$\times \exp\left[-\beta \sum_{i=1}^{P} \left(\frac{1}{2} m\omega_P^2 (\mathbf{R}_{i+1} - \mathbf{R}_i)^2 + \frac{1}{P} V(\mathbf{R}_i)\right)\right]\ , \tag{2.94}$$

where $\omega_P = \frac{\sqrt{P}}{\beta}$ and $\mathbf{R}_{P+1} = \mathbf{R}_1$ to approximate the effect of the limit $P \to \infty$.

The outcome indicates an isomorphism between a static quantum mechanical problem and the classical problem of a replicated classical particle. This classical particle is under the influence of a potential $V(\mathbf{R})/P$, and in addition it also interacts with two (and only two) of its own images through a quadratic potential.

Many quantum particles

The previous result for one isolated quantum particle can be extended to an N-particle system [116]. In this case, the partition function is

$$\begin{aligned}\mathcal{Z} = \lim_{P\to\infty} \prod_{I=1}^{N} \left(\frac{M_I P}{2\pi\beta}\right)^{3P/2} \int \mathrm{d}\mathbf{R}_I^{(1)} \cdots \mathrm{d}\mathbf{R}_I^{(P)} \times \\ \times \exp\left(-\beta \sum_{s=1}^{P} \left\{ \sum_{I=1}^{N} \frac{1}{2} M_I \omega_P^2 \left(\mathrm{R}_I^{(s)} - \mathrm{R}_I^{(s+1)}\right)^2 + \right.\right. \\ \left.\left. + \frac{1}{P} V(\{\mathrm{R}_I^{(s)}\}) \right\}\right) ,\end{aligned} \tag{2.95}$$

where M_I is the mass of nucleus I, $\mathrm{R}_I^{(P)}$ is the position of nucleus I in the Pth replica, and as in the case of one particle, $\mathrm{R}_I^{(P+1)} = \mathrm{R}_I^{(1)}$. This integral can also be written as a phase space integral:

$$\begin{aligned}\mathcal{Z} =& \prod_{I=1}^{N} \mathcal{N} \iint \mathrm{d}\mathbf{R}_I^{(1)} \cdots \mathrm{d}\mathbf{R}_I^{(P)} \mathrm{d}\mathbf{P}_I^{(1)} \cdots \mathrm{d}\mathbf{P}_I^{(P)} \\ & \times \exp\left(-\beta \sum_{s=1}^{P} \left\{ \sum_{I=1}^{N} \left\{ \frac{P_I^{(s)2}}{2M_I'} + \frac{1}{2} M_I \omega_P^2 \left(\mathrm{R}_I^{(s)} - \mathrm{R}_I^{(s+1)}\right)^2 \right\} + \right.\right. \\ & \left.\left. + \frac{1}{P} V(\{\mathrm{R}_I^{(s)}\}) \right\}\right) ,\end{aligned} \tag{2.96}$$

where $\mathcal{N}$ is a normalization factor.

As a remark, this method works only for the Partition function of the system, not for the Hamiltonian. This means, that although one can derive a Hamiltonian from the partition function of the replicated system,

$$\begin{aligned}\mathcal{H} =& \sum_{s=1}^{P} \left\{ \sum_{I=1}^{N} \left\{ \frac{P_I^{(s)2}}{2M_I'} + \frac{1}{2} M_I \omega_P^2 \left(\mathrm{R}_I^{(s)} - \mathrm{R}_I^{(s+1)}\right)^2 \right\} + \right. \\ & \left. + \frac{1}{P} V(\{\mathrm{R}_I^{(s)}\}) \right\} ,\end{aligned} \tag{2.97}$$

the resulting dynamics of this Hamiltonian system cannot be directly related to the quantum system being studied, but rather only the statistical properties of the ensemble.

The Hamiltonian in eq. (2.97) presents the isomorphism between the quantum system and the replicated classical system. As in the case of one isolated particle, each atom interacts with two of its replicas, with the difference that in this case each particle interacts in addition with all the other particles within its replica. This interaction takes place with a P-times weaker potential and a P-times higher temperature. Due to this topology, the replicated systems are usually named a "ring polymer" or "ring necklace" (see illustration in fig. 2.1). This representation fits the design of parallel computers, thus a straightforward implementation can present a linear scaling of the time needed for a calculation when more beads are added. The overall scaling of the method with system size will therefore depend only on the implementation of the MD in which each replica is calculated. This good scaling turns the method into a powerful tool to calculate statistical properties of materials including nuclear quantum effects.

The Staging transformation

If the number of replicas P is large, the harmonic potentials (usually called *"springs"*) between beads are P-times stronger, and the V potential between particles in a replica is P-times weaker (see eq. (2.97)). Then, the harmonic forces can dominate the dynamics and the system could not explore the rest of the phase space efficiently. For this reason, the harmonic modes have to be decoupled if the number of replicas P is

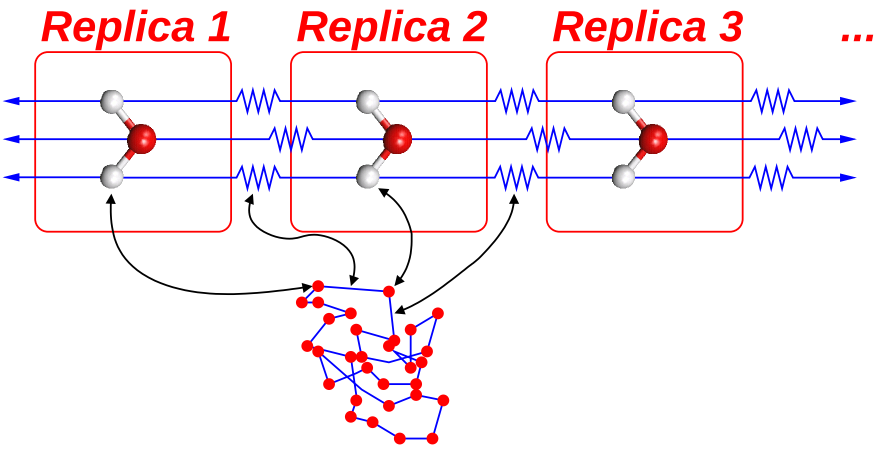

Figure 2.1: Illustration of the topology of the Path Integral representation, in this case for a water molecule. The replicas are represented spatially separated only for illustration purposes, being in actuality highly superimposed.

large. This can be accomplished by applying the *staging transformation* [116], which was developed in analogy to the staging Monte Carlo method [107].

In this transformation, the nuclear coordinates $\mathbf{R}_I$ of each nucleus I is transformed via

$$\begin{aligned} \mathbf{u}_I^{(1)} &= \mathbf{R}_I^{(1)} \;, \\ \mathbf{u}_I^{(s)} &= \mathbf{R}_I^{(s)} - \mathbf{R}_I^{(s)*} \;, \qquad s = 2, \ldots, P \;, \end{aligned} \tag{2.98}$$

with

$$\mathbf{R}_I^{(s)*} := \frac{(s-1)\mathbf{R}_I^{(s+1)} + \mathbf{R}_I^{(1)}}{s} \;, \tag{2.99}$$

and being s the replica index ($s \in [1 \ldots P]$). The transformation can be inverted via

$$\begin{aligned} \mathbf{R}_I^{(1)} &= \mathbf{u}_I^{(1)} \;, \\ \mathbf{R}_I^{(s)} &= \mathbf{u}_I^{(1)} + \sum_{t=s}^{P} \frac{s-1}{t-1} \mathbf{u}_I^{(t)} \;, \qquad s = 2, \ldots, P \;. \end{aligned} \tag{2.100}$$

Substituting this transformation into (2.96), the resulting partition function reads

$$
\begin{aligned}
Z = \prod_{I=1}^{N} \mathcal{N}' \iint & \mathrm{d}\mathbf{u}_I^{(1)} \cdots \mathrm{d}\mathbf{u}_I^{(P)} \mathrm{d}\mathbf{P}_I^{(1)} \cdots \mathrm{d}\mathbf{P}_I^{(P)} \times \\
& \times \exp\left(-\beta \sum_{s=1}^{P} \left\{ \sum_{I=1}^{N} \left\{ \frac{(P_I^{(s)})^2}{2M_I'^{(s)}} + \frac{1}{2} M_I^{(s)} \omega_P^2 \left(\mathbf{u}_I^{(s)} \right)^2 \right\} + \right.\right. \\
& \left.\left. + \frac{1}{P} U(\{\mathbf{R}_I^{(s)}\}) \right\} \right) ,
\end{aligned}
\tag{2.101}
$$

where the *staging masses* $M_I^{(s)}$ are defined as

$$
\begin{aligned}
M_I^{(1)} &= M_I , \\
M_I^{(s)} &= \frac{s}{s-1} M_I , \quad s = 2, \ldots, P .
\end{aligned}
\tag{2.102}
$$

The harmonic oscillators are now decoupled from each other. A side consequence is that, as the degrees of freedom are completely decoupled, they now have to be coupled to thermostats to assure the generation of an NVT ensemble. Using this method, the path integral calculations are expected to sample its phase space much more efficiently.

2.4 Calculation of Chemical Shifts from DFT

Nuclear magnetic resonance (NMR)[3] is a widespread technique in the fields of physics, chemistry and biology. The main observable of this technique is the NMR chemical shift spectrum,

---

[3] in this work we refer to NMR as the NMR spectroscopy technique, although strictly speaking the term NMR refers to the phenomena in which the technique is based.

which allow the characterization of the chemical environment of individual atoms.

In the case of spin-1/2 nuclei, the phenomena of NMR is based on the splitting ΔE of the energy levels of a nucleus by the presence of an external magnetic field B_0. The splitting of the energy levels in the nuclei is proportional to the magnitude of the field B_0 and the magnetogyric ratio γ of the nucleus,

$$\Delta E \propto \gamma B_0 \; . \tag{2.103}$$

Since the electrons also react to the external field, the total magnetic field responsible for this energy splitting is the superposition of the external field B_0 and the field B' induced by the electronic response,

$$\Delta E' \propto \gamma (B_0 + B') \; . \tag{2.104}$$

From a quantum mechanical perspective, the chemical shift is actually caused by a change in the electronic wavefunction due to the external magnetic field. This field induces electronic currents, which in turn also interact with the nuclear spins.

The effect of the shifting in the energy level splitting $\Delta E'$ of the nuclei due to the presence of the local B' field is called a chemical shift. More precisely, the chemical shift δ is the dependence of the induced magnetic field B' on the external magnetic field B_0, with respect to a reference chemical environment. As a consequence, the chemical shift is an immensely important observable, since it carries information about the environment in which each atom is immersed.

In the following, a brief introduction to the calculation of chemical shifts from DFT calculations is presented. This presentation does not show the improvements used in order to solve the issues brought about by the use of periodic boundary conditions. A good discussion on the particular implementation under periodic conditions can be found in [99, 92].

2.4.1 *Derivation*

The Nuclear Shielding Tensor

The nuclear shielding tensor $\sigma(\mathbf{R})$ is defined as

$$\sigma(\mathbf{R}) = -\frac{\partial \mathbf{B}^{\mathrm{ind}}(\mathbf{R})}{\partial \mathbf{B}^{\mathrm{ext}}}\,, \tag{2.105}$$

that is, the proportionality tensor between the induced and the external magnetic field at the nuclear position $\mathbf{R}$. The absolute values of this tensor cannot be experimentally measured, but rather its difference to the values corresponding to a standard molecule. The difference between the isotropic part of this tensor for a given nucleus in a molecule and the same nucleus in a standard chemical environment called the chemical shift δ.

Application of an external magnetic field

If a constant external magnetic field is applied to a quantum system, its effect can be formulated as a modification to the Hamiltonian $\mathcal{H}_0$, where the momentum operator $\hat{\mathbf{p}}$ is transformed into a shifted momentum operator $\hat{\pi}$. This shifted operator is defined as $\hat{\mathbf{p}} \to \hat{\pi} = \hat{\mathbf{p}} - \frac{1}{c}\mathbf{A}$, where $\mathbf{A}$ is the vector potential of the applied external field. The resulting Hamiltonian with the external field reads

$$\begin{aligned}\mathcal{H} &= \frac{1}{2}\hat{\pi}^2 + V \qquad (2.106)\\ &= \frac{1}{2}\left(\hat{\mathbf{p}} - \frac{1}{c}\mathbf{A}\right)^2 + V\\ &= \frac{\hat{p}^2}{2} + V - \frac{1}{2c}(\hat{\mathbf{p}}\cdot\mathbf{A} + \mathbf{A}\cdot\hat{\mathbf{p}}) + \frac{1}{2c^2}\mathbf{A}^2\,,\end{aligned}$$

where c is the speed of light in atomic units. Here, the vector potential $\mathbf{A}$ of the homogeneous field $\mathbf{B}^{\mathrm{ext}}$ is defined as

$$\mathbf{A}(\mathbf{r}) = \frac{1}{2}\,\mathbf{B}^{\mathrm{ext}} \times (\mathbf{r} - \mathbf{R})\,. \qquad (2.107)$$

Gauge choice problem

The previous is a particular gauge, chosen to simplify the derivation. The gauge invariance $\mathbf{A} \rightarrow \mathbf{A}' = \mathbf{A} + \nabla\phi(\mathbf{r})$ is, however, lost in the numerical implementation due to the truncation of the basis set in the actual calculations. To solve this problem, many possible approaches were suggested, for instance

- *Gauge Including Atomic Orbitals* (GIAO) [19] (the atom position is the gauge origin for the basis functions –i.e. the *atomic orbitals*–)
- *Individual Gauges for Localized Orbitals* (IGLO) [61] (the center of charge of the molecular orbitals is chosen as origin)
- *Continuous Set of Gauge Transformations* (CSGT) [50] (the gauge depends on where the induced current is calculated)

A thorough comparison of these approaches can be found in [15]. In this work, the CSGT gauge is used.

Perturbation of the wavefunction by the external magnetic field

Assuming the effect of the magnetic field as a perturbation, one can truncate in the linear term of the expansion in the magnetic field, which from eq. (2.106) is:

$$\mathcal{H}_1 = -\frac{1}{2c}(\hat{\mathbf{p}} \cdot \mathbf{A} + \mathbf{A} \cdot \hat{\mathbf{p}}) \; . \tag{2.108}$$

To the first order of this perturbation, the ground state $|\Psi_0'\rangle$ of the Hamiltonian $\mathcal{H} = \mathcal{H}_0 + \mathcal{H}_1$ reads [87, sec. 1.5]:

$$\begin{aligned} |\Psi_0'\rangle &= |\Psi_0\rangle + \sum_n \frac{\langle \Psi_n | \mathcal{H}_1 | \psi_0 \rangle}{E_0 - E_n} \, |\Psi_n\rangle \\ &\equiv |\Psi_0\rangle + \sum_n V_{n,0} |\Psi_n\rangle \; . \end{aligned} \tag{2.109}$$

The expansion to the first order of the wavefunction can be used to calculate the induced current. The quantum current operator corresponding to the problem is

$$\hat{\mathbf{j}} = \frac{1}{2} \, (\hat{\pi}|\mathbf{r}\rangle\langle\mathbf{r}| + |\mathbf{r}\rangle\langle\mathbf{r}|\hat{\pi}) \; , \tag{2.110}$$

thus the total current $\mathbf{j}^{\mathrm{el}} = \langle \Psi_0' | \hat{\mathbf{j}} | \Psi_0' \rangle$ reads

$$\begin{aligned} \mathbf{j}^{\mathrm{el}}(\mathbf{r}) &= \frac{1}{2\mathrm{i}}(\Psi_0^* \nabla \Psi_0 - \Psi_0 \nabla \Psi_0^*) \\ &\quad + \sum_n \frac{1}{2\mathrm{i}}(\Psi_0^* \nabla \Psi_n - \Psi_n \nabla \Psi_0^*) V_{n,0} \\ &\quad + \sum_n \frac{1}{2\mathrm{i}}(\Psi_n^* \nabla \Psi_0 - \Psi_0 \nabla \Psi_n^*) V_{n,0}^* \\ &\quad - \frac{1}{c}\mathbf{A}|\Psi_0|^2 \; , \end{aligned} \tag{2.111}$$

where the first term is the unperturbed current $\langle \Psi_0 | \hat{\mathbf{j}} | \Psi_0 \rangle$, and therefore vanishes (the bra and ket can be chosen to be real).

Calculation of the chemical shift from the perturbed wavefunction

The magnetic field induced at the nucleus is, according to the *Biot-Savart* law,

$$\mathbf{B}^{\text{ind}}(\mathbf{r}) = \frac{1}{c}\int \mathrm{d}^3r'\mathbf{j}^{\text{el}}(\mathbf{r}') \times \frac{(\mathbf{r}-\mathbf{r}')}{|\mathbf{r}-\mathbf{r}'|^3}\ . \tag{2.112}$$

Applying this to the law in eq. (2.105) the components of the shielding tensor are obtained:

$$\sigma_{i,j}(\mathbf{r}) = \frac{1}{cB}\int \mathrm{d}^3r' \left[\mathbf{j}_i^{\text{el}}(\mathbf{r}') \times \frac{(\mathbf{r}-\mathbf{r}')}{|\mathbf{r}-\mathbf{r}'|^3}\right]_j\ . \tag{2.113}$$

Finally, the computed chemical shift δ is obtained via

$$\delta = \sigma_{ref} - \frac{1}{3}\mathrm{Tr}\left[\sigma(\mathbf{R}_n)\right]\ . \tag{2.114}$$

The reference σ_{ref} for ^{1}H-NMR is the tetramethylsilane molecule (TMS), which has an absolute nuclear shielding of $\sigma_{ref} = 31.7$ ppm (from DFT calculations).

2.5 Final Remarks

In this chapter, the main concepts from in *ab-initio* Molecular Dynamics simulations used in this work where introduced.

The methods described in this chapter have been developed during almost a century, making a fairly solid framework where chemical systems can be studied with an excellent accuracy. In this thesis, we take advantage of this accuracy to study the physicochemical properties and phenomena taking place on the systems of interest.

Chapter 3

Complex hydrides for hydrogen storage applications: Structure and nuclear quantum properties of the Li_2NH–$LiNH_2$ system

The issue of hydrogen storage is one of the key problems for the actual implementation of the so-called hydrogen economy, due to the difficulty of transporting hydrogen in its function as an energy carrier. The central aim is to store and release molecular hydrogen efficiently and without excessive needs in terms of pressure, temperature, and time. In this context, the lithium amide ($LiNH_2$) / lithium imide (Li_2NH) system is arguably one of the most promising hydrogen storage systems due to its very light weight. In addition, the lithium imide/amide system is considered to present all the main properties of the family of complex hydrides, thus being a model system for these hydrogen storage materials.

The lithium imide/amide system can in principle reversibly store and release molecular hydrogen via the reaction

$$\mathrm{Li_2NH} + \mathrm{H_2} \rightleftharpoons \mathrm{LiNH_2} + \mathrm{LiH}. \tag{3.1}$$

This reaction has a high H storage density (6.5% wt. [17]), although there are still important technological difficulties in the release reaction [29, 68, 52]. The main drawback for H_2 storage in alkali imides is presently the extremely low reversibility of the storage reaction (3.1). In technologically feasible prototypes, the actual amount of reversibly stored H_2 is only about 3% [36]. Our intention is to address this problem by first improving our understanding of the atomistic structure of this class of compounds, eventually helping the understanding the dynamics and the molecular mechanism of the storage reaction. In this way, an explanation for the underlying microscopic effects that determine the degree of reversibility in the storage/release reaction (3.1) can be provided.

A lot of research, both computational and experimental, has been done on lithium imide (Li_2NH), since the exact structure of the material is not yet fully determined [41]. In this direction, the possibility of quantum delocalization of the protons has been reported [123]. This unusual quantum behavior could be the reason of the unclear structure of the hydrogen atoms in the material, whose understanding plays a key role in the development of a proper technological implementation of this system. The configuration of the lithium lattice in the material is also a matter of debate, as a phase transition in the material is taking place at about 80 °C, which is related to the mobility and configuration of the lithium cations. In this respect, superionicity due to possible high diffusivity of the lithium cations has been reported from computational studies of the material [77].

In this work, the problem of the structural properties of Li_2NH and $LiNH_2$ is addressed by means of Path-Integral Molecular Dynamics (PIMD) simulations (sec. 2.3). The PIMD approach gives access to the quantum nature of the atomic nuclei, while the underlying potential energy landscape is expressed within gradient-corrected density functional theory (DFT) (sec. 2.1). With the help of these tools, the structural parameters are investigated on the atomistic level. The aim is to get detailed information on the local "packing" of the crystalline material, including the orientation of the NH bonds, the position of the hydrogen and the lithium. This information is also very important for understanding the individual steps of the hydrogen storage process, which requires the diffusion of hydrogen atoms through the crystallites [36].

The atomistic structural parameters are difficult to measure directly, in particular in the absence of long-range crystalline order. In turn, Nuclear Magnetic Resonance (NMR) spectroscopy can provide a more detailed insight into features of the local structure, due to its high sensitivity at the macroscopic length scale [11, 42, 106]. Hence, the computational results of electronic structure calculations are compared with solid-state NMR experiments. This combination can support or invalidate a given structural proposition obtained from a computational first-principles approach [100, 122].

The main questions addressed in this chapter are the elucidation of the proper structure of the material at ambient temperature, the relevance of nuclear quantum properties of hydrogen in the structure of the material, and the possibility of quantum delocalization within this structure. As a tangible outcome of the research presented in this chapter, the articles [71, 70] were authored.

3.1 Methods

3.1.1 *Computational setup*

Our calculations are based on DFT (see sec. 2.1), in the generalized gradient approximation using the BLYP exchange-correlation functional [7, 63]. The orbitals were expanded in plane waves, using Goedecker pseudopotentials for N and Li [26]. The plane-wave cutoff was set to 120 Ry, which turned out to be necessary to achieve converged results for the vibrational spectra of molecular Li_2NH. The timestep was set to 0.085 fs to assure an overall stability (in particular in combination with the path integral technique, see below). The energy hypersurface generated by DFT was used for molecular dynamics simulations via the Car-Parrinello (CPMD) scheme (sec. 2.2.2), using the CPMD code [37], thus applying realistic atomic motion at ambient temperatures to the system. In order to incorporate nuclear quantum effects, especially of the light H and Li atoms, the path integral technique (sec. 2.3) was applied on top of the CPMD simulations, with a Trotter decomposition into P=2,4,8 and 16 beads for $LiNH_2$ and P=4,6,16,32 and 64 beads for Li_2NH. One such bead corresponds to one timestep in imaginary time; the ensemble of coordinates for a given imaginary time is called a replica. Each replica is propagated in real time, forming eventually a path integral trajectory.

The NMR chemical shift calculations were performed within the same framework, using the linear response module of the

CPMD code [92, 102, 101]. This implies a full consideration of the periodic boundary conditions of the condensed phase systems studied in this work. The molecular dynamics trajectories were sampled with NMR calculations using a set of snapshots extracted at random times (with time offsets of at least 0.1 ps). Typically, about 200 configurations were sampled for each of the systems. When combined with the path integral sampling scheme, individual replica from (randomly selected) real-time snapshots were taken as configurations for the NMR calculations. No pre-averaging over imaginary time was performed. Since experimental NMR measurements average the NMR resonances over relatively long times (microseconds), the NMR chemical shifts obtained from both the conventional MD trajectories ($P = 1$) and the path integral MD runs ($P > 1$) have to be averaged for comparison with the corresponding experimental results.

The unit cell for Li_2NH has dimensions of $5.007 \times 5.007 \times 5.007$ Å and contains 16 independent atoms (i.e. 4 Li_2NH molecules). The $LiNH_2$ unit cell is twice as large (32 atoms) with cell dimensions of $5.0079 \times 5.0079 \times 10.0158$ Å. The systems were equilibrated with five PIMD simulations with increasing temperatures of 1 ps duration, until the target temperature of 300 K was reached. The subsequent production runs were between 4 and 9 ps long.

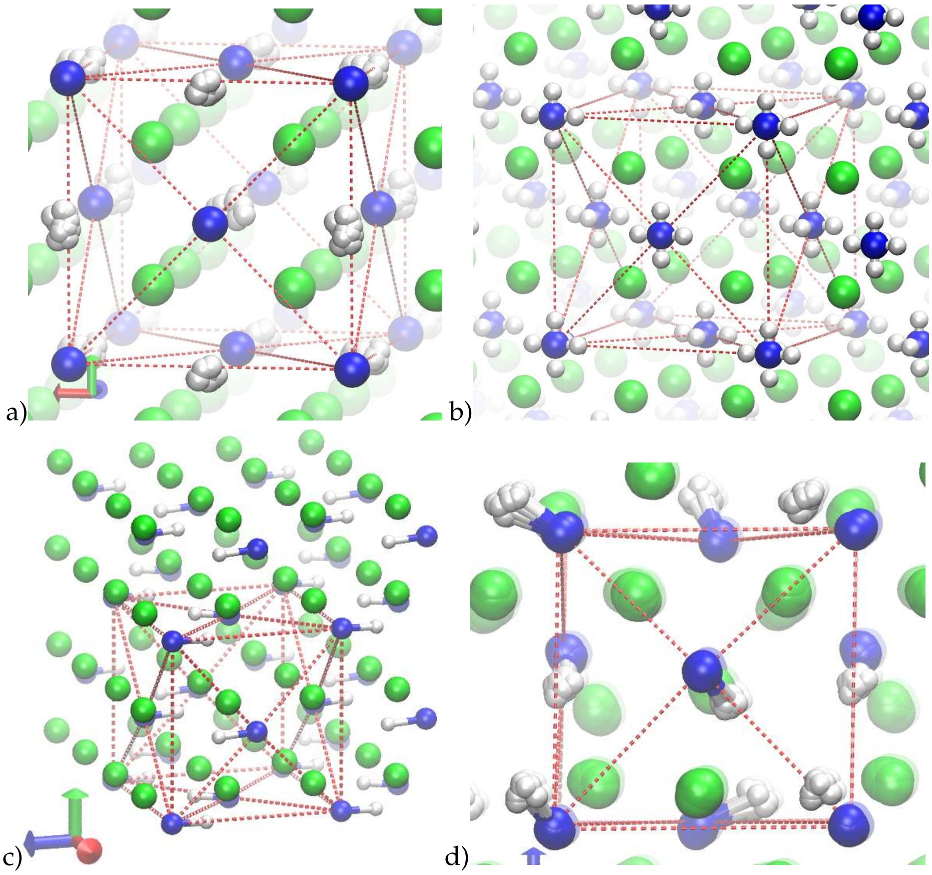

Figure 3.1: Initial and relaxed structures of Li_2NH. N atoms are blue, H white, and Li green. **a)** Initial structure as extracted from X-ray data. **b)** Fictitious structure in which each of the six symmetry-equivalent H sites around the nitrogen atoms is populated by a proton. **c)** Structure after relaxation of (only) the hydrogen atoms. **d)** Fully relaxed structure, with no geometric constrains.

3.2 Structural properties

3.2.1 *Local disorder in lithium imide (Li_2NH)*

A first set of *ab-initio* PIMD simulations of Li_2NH was performed using starting configurations from recently reported crystal structures which were obtained from X-ray scattering and neutron powder diffraction experiments [80, 82]. The local conformations are illustrated in fig. 3.1. Both N and H atoms are located on FCC sites with a lattice constant of 5.007 Å, while Li atoms on an intercalated simple cubic (SC) lattice with half the lattice constant. One hydrogen atom locates at the center between each pair of nitrogen atoms, which would correspond to N-H distances of 2.5 Å. Such a geometry appears chemically not meaningful, but is useful as an unbiased starting point for structural relaxation. In this configuration, the hydrogen positions might be seen as the effective center of mass of a quantum-mechanically delocalized atom in a low-barrier N-H-N double well potential.

As an initial equilibration run within the path integral framework (T=300K, P=16 beads), both N and Li positions were fixed, and only the protons were effectively treated quantum-mechanically. This was achieved by increasing the nuclear mass of N and Li to very large values, turning then into classical immobile nuclei, while the H atoms with their small mass of m_H=1 u were allowed to delocalize spatially. This equilibration run resulted in the formation of normal N-H bonds (d_{NH} ~1.05 Å, oriented along the N-H$\cdots$N direction within the first 0.1 ps (structure shown in fig. 3.1c). In our relatively small unit cells, the orientation of the NH vector showed an antiferroelectric pattern. No quantum delocalization was observed during a subsequent PIMD run of up to 9 ps.

A second attempt to obtain a quantum delocalization of the hydrogens within the PIMD simulations was performed using a starting geometry built from a random distribution of the path integral beads on the six symmetry-equivalent hydrogen positions around each nitrogen. This configuration was suggested from DFT calculations of the potential energy surface for the proton motion, which provided evidence for a very low potential energy barrier between these six equivalent proton sites [123]. The structure used here is illustrated in fig. 3.1b, where each of the six equivalent octahedral sites is filled with a hydrogen atom. However, from this initial configuration the PIMD simulations resulted in a quick localization (within the first 0.1 ps) of the hydrogen particles and the formation of regular NH bonds with antiferrroelectric ordering along the NH$\cdots$N direction.

In a second set of PIMD calculations, the lithium atoms were relaxed as well, by back-substituting their physically correct masses within the path integral framework. Surprisingly, the molecular dynamics simulations yielded a very fast displacement of the Li positions away from their original SC lattice sites. It turned out that this Li motion comes to rest within the first 1 ps of PIMD simulation time (illustrated in fig. 3.2), resulting in a considerable lowering of the potential energy of the system. Thus, it must be considered a real structural relaxation process; a graphical representation of the final equilibrated structure is shown in fig. 3.1d.

While the total mean square displacement per Li atom $\Delta^2 R^{(\mathrm{Li})}(t) = \langle[\mathbf{R}_{\mathrm{Li}}(t) - \mathbf{R}_{\mathrm{Li}}(0)]^2\rangle_{\mathrm{Li}}$ amounts only to about 1.7 Å^2 (see fig. 3.2), a systematic pattern in the final lithium coordinates was not identified. Hence, the relaxed Li structure is considered as disordered, although the small unit cell size permits only a limited amount of disorder. Along with this Li relaxation, a reorientation of the NH vectors was observed, which is correlated with the Li motion.

In the final relaxed conformation, the system retains its anti-

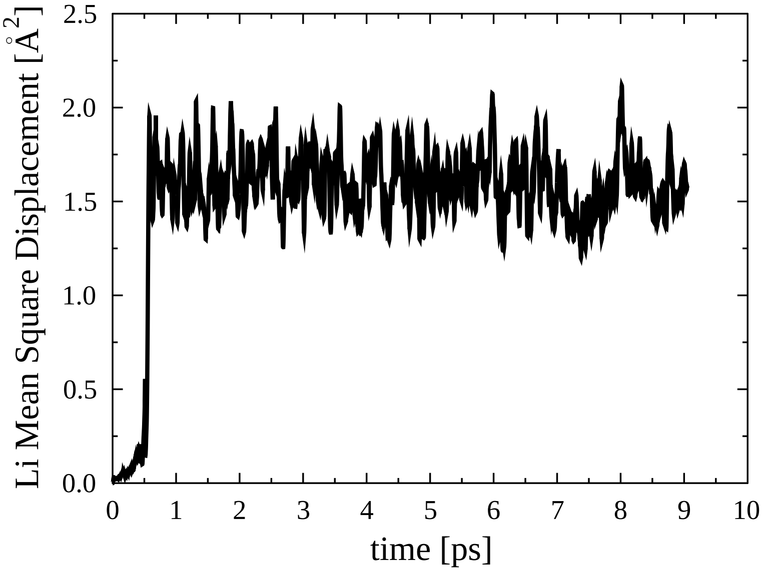

Figure 3.2: Average mean square displacement of the Li atoms in Li_2NH. The relaxation of the lithium atoms is converged after 1 ps.

ferroelectric pattern of the NH orientations, and the NH bond angle distribution converges to a very marked configuration as shown in fig. 3.3 and table 3.1. The average NH angles θ form angles of 30° with the c lattice vector (the vertical axis in fig. 3.1), and 150° for the antiferroelectric NH partner. This orientation is no longer parallel to any lattice vector nor related to any pair of heavy atoms, as observed in the previous calculations with fixed Li coordinates. Instead, it appears to be a conformation which avoids any NH$\cdots$X hydrogen bonds.

As the final step, the constraints on the nitrogen atoms were released, and all atoms were set free to relax. However, no substantial rearrangement of the atomic positions was observed compared to the structure that was relaxed with fixed nitrogen coordinates. Further varying the number of beads within the path integral scheme between $P = 1$ and $P = 64$ did not

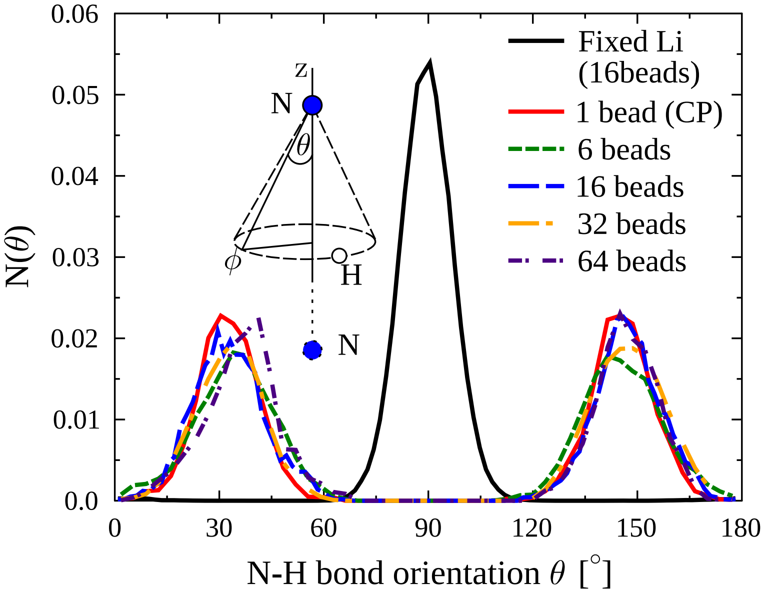

Figure 3.3: Azimuth NH bond angle distributions (θ) in Li$_2$NH after relaxation of all Li,N, and H atoms, performed for different numbers of path integral beads P. Also shown is the distribution resulting from a relaxation with both N and Li atoms fixed at their experimentally reported crystal lattice positions (black line).

show any sizeable dependency of the final equilibrated configuration after about 9 ps of MD relaxation time.

While the average NH bond distance is about the same for $P = 1$ to $P = 64$ beads (1.0 Å), the quantum delocalization has a strong broadening effect on the distribution (see table 3.1). In contrast to this, the distribution of the azimuthal angles θ between the NH vector and the c crystal axis (also shown in table 3.1) is found to be virtually independent of the nuclear quantum delocalization.

To conclude on the relaxation calculations, the local structure of lithium imide seems to be considerably more complicated than previously assumed. While the N lattice remained

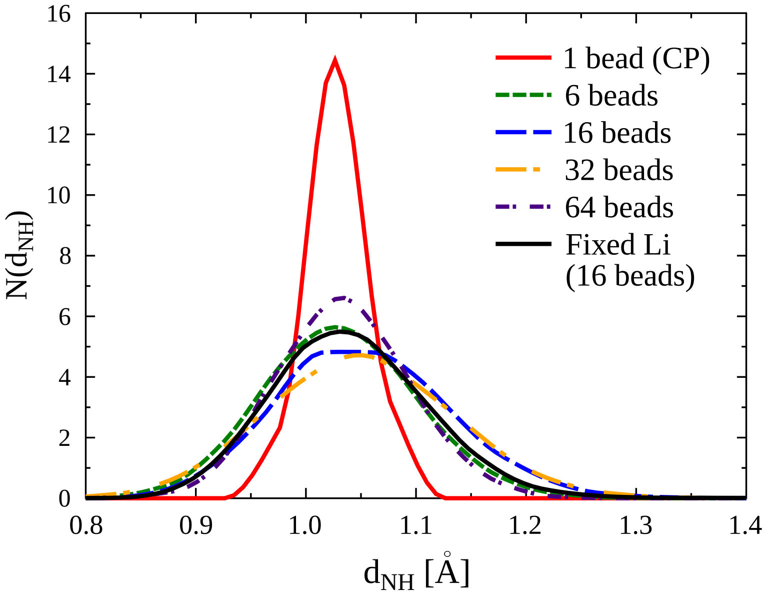

Figure 3.4: NH bond distance distributions in Li_2NH for different numbers of path integral beads P.

well-ordered in our calculations, the Li atoms significantly relaxed to well-defined but effectively disordered sites. Only on average, the Li coordinates can be assumed to be on the reported sites on a simple cubic lattice that is intercalated in the nitrogen FCC lattice. The hydrogen atoms are conventionally bonded to nitrogen, with the NH vectors oriented in an antiferroelectric arrangement, forming an angle of 30° with the c lattice vector. Further, a precession motion of the NH vector around this axis was observed during the molecular dynamics simulations. This behavior is illustrated in fig. 3.5, and has already been recently reported in conventional MD calculations [77]. In turn, no strong direct-space quantum delocalization of the protons or lithium atoms was observed in the PIMD trajectories beyond the normal bond distance broadening of the NH bond.

Beads	θ [°]	N-H bond distance [Å]
1 (Class.)	$32 \pm 9 \mid 146 \pm 9$	1.03 ± 0.03
6	$34 \pm 12 \mid 145 \pm 11$	1.04 ± 0.11
16	$33 \pm 10 \mid 148 \pm 10$	1.05 ± 0.09
32	$32 \pm 10 \mid 146 \pm 13$	1.05 ± 0.18
64	$36 \pm 11 \mid 146 \pm 9$	1.03 ± 0.07

Table 3.1: Li_2NH N-H bond angles θ and distances after complete relaxation without geometrical constrains.

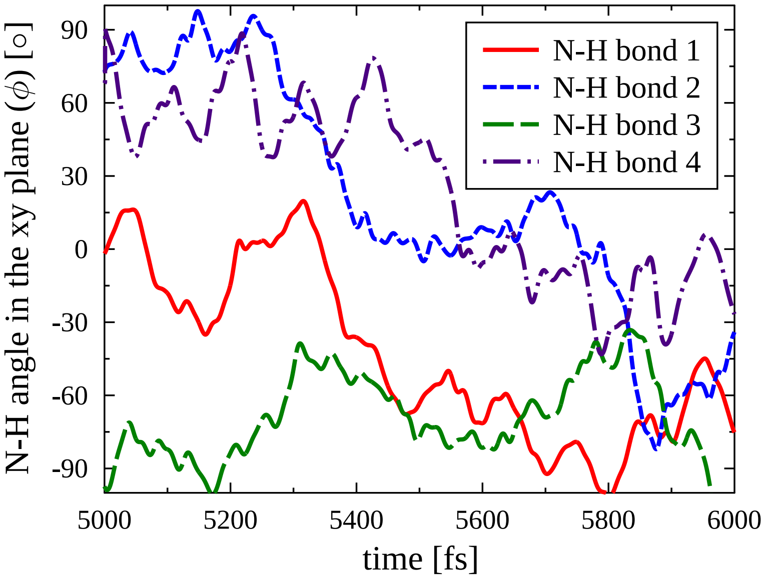

Figure 3.5: Time evolution of the polar angles of the NH vectors in Li_2NH. The drifts in the angles represent the precession of the bond along one c lattice vector.

3.2.2 *$LiNH_2$ calculations*

The structure of $LiNH_2$ is illustrated in fig. 3.6. The lattice constant and the nitrogen positions are about the same as Li_2NH, and the Li atoms are found on the same intercalated simple cubic lattice. The only difference between the twofold protonation of the nitrogen is that every second site of the lithium SC lattice is not occupied.

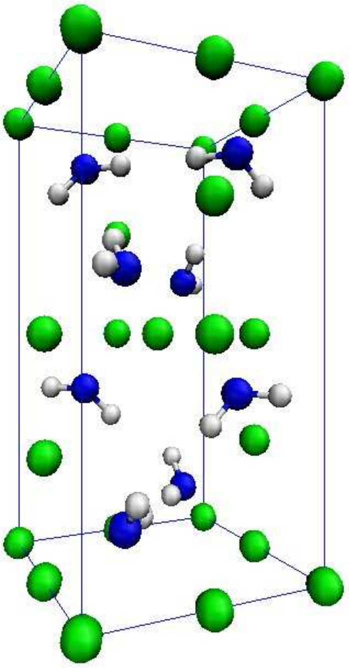

Figure 3.6: X-ray structure of $LiNH_2$.

The starting geometry for our calculations was taken from experimental X-ray and neutron diffraction data [30]. It turned out that this configuration is stable during our calculations of up to 5 ps. Neither the HNH angle nor the NH bond distance deviate from their values in the regular NH_2^- anion (see fig. 3.8, and the corresponding table 3.2). No sizeable influence of the number of path integral beads on their average values was detected (using P=1,2,4,8 and 16). Only the width of the corresponding distribution broadened by a factor of two between the conventional (P=1) and path integral-based calculations.

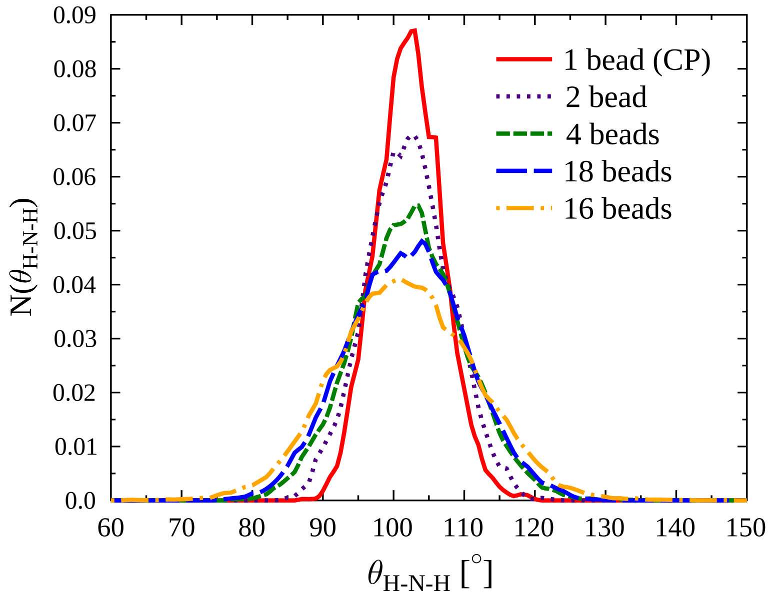

Figure 3.7: Distribution of the H-N-H angle in LiNH$_2$ under different number of path integral beads P.

P	HNH angle [°]	NH bond distance [Å]
1	102.3 ± 4.7	1.017 ± 0.029
2	102.1 ± 5.9	1.019 ± 0.040
4	102.2 ± 7.7	1.023 ± 0.053
8	101.9 ± 8.3	1.029 ± 0.066
16	101.7 ± 9.8	1.037 ± 0.079

Table 3.2: Average bond angles and distances in lithium amide (LiNH$_2$), including the widths of the distributions.

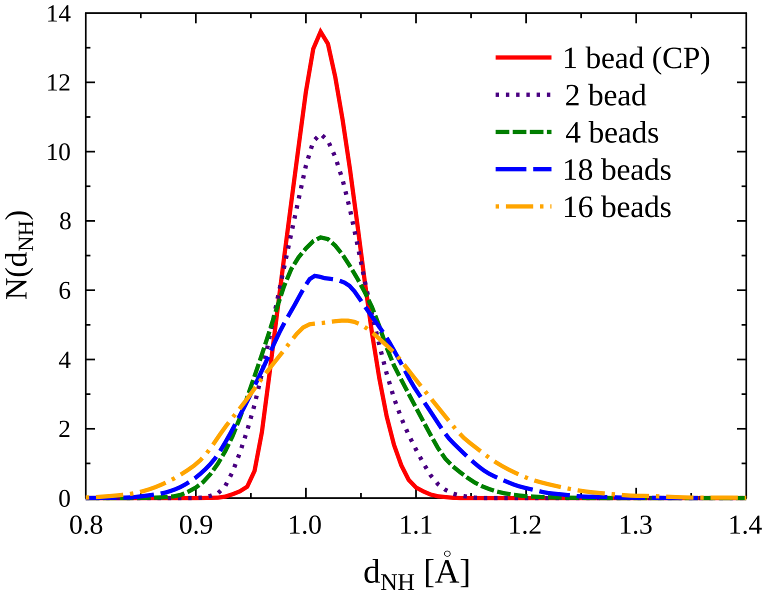

Figure 3.8: Distribution of the NH bond lengths $LiNH_2$ under different number of path integral beads P.

3.2.3 *NMR chemical shifts*

Both the orientation of the NH bonds and the displacement of the lithium atoms from their projected lattice sites are difficult to measure directly. In particular, X-ray diffraction would suffer from the lack of long-range order in this system. NMR spectroscopy, in turn, is particularly sensitive to local packing. Thus, the series of ab-initio path integral trajectories for both Li_2NH and $LiNH_2$ were sampled with NMR calculations under periodic boundary conditions [92, 102].

The resulting computed ^1H NMR chemical shift histograms are shown along with the anticipated experimental chemical shift values (which are discussed in the next section) in fig. 3.9. For Li_2NH, we have also included the spectra obtained from a partial structural relaxation (with the Li and N atoms fixed on their lattice sites as reported by X-ray experiments). The NMR pattern computed from the latter trajectory disagrees with experiment, while the fully relaxed structure yields a very good agreement. This strongly supports our picture of the lithium relaxation towards somewhat disordered sites. For $LiNH_2$, the computed NMR lines also agree very well with the experimental values, thus validating the structural stability indicated by our molecular dynamics simulations.

The effect of nuclear quantum delocalization is surprisingly almost absent in Li_2NH: the NMR histograms for $P > 1$ are not much broader than the one obtained from a conventional ($P = 1$) trajectory. The amide instead shows a clear broadening of the NMR line upon switching to the path integral framework with its additional nuclear delocalization.

It should be noted here that the NMR lineshape computed

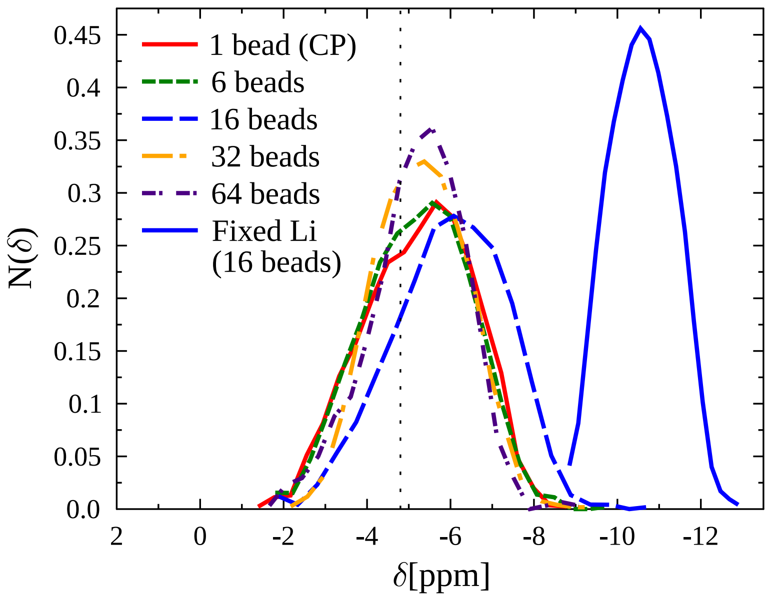

Figure 3.9: Simulated ^{1}H NMR chemical shift spectra of Li_2NH under the different computational conditions considered here. The experimental peak value is marked with a vertical dotted line.

from neither the $P = 1$ nor the $P > 1$ trajectories can be directly related to the experimental lineshape. The former width is due to the distribution of instantaneous chemical shift values of different snapshots from the trajectories. The experimental NMR linewidth, however, is either due to a heterogeneous sample or anisotropic interactions that are not fully averaged by the Magic Angle Spinning technique (MAS). The ^{1}H MAS NMR spectra is affected in particular by homonuclear dipolar couplings causing a strong line broadening. Since the mechanism of the broadening is distinct from the width of the simulated chemical shift histograms, the experimental shifts are only indicated by a dotted line in order to avoid confusion. Dipolar couplings or other line broadening effects are not considered within the simulation.

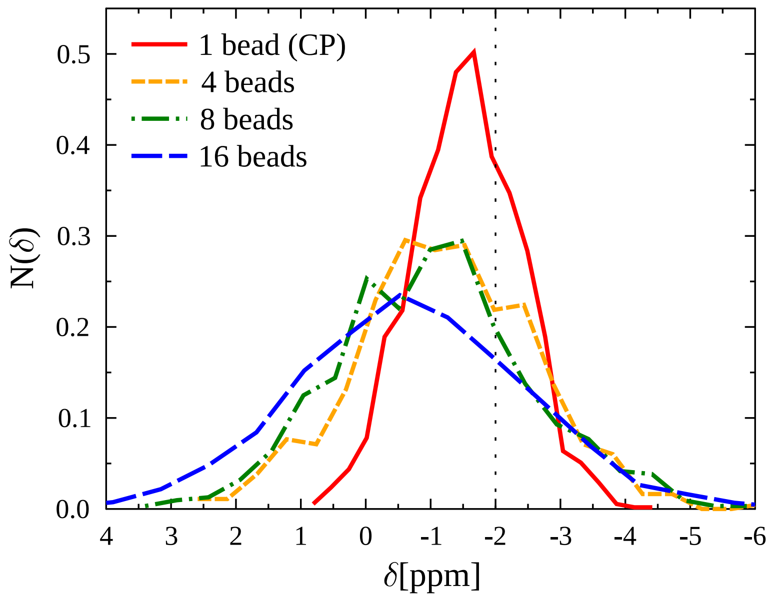

Figure 3.10: Simulated ^{1}H NMR chemical shift spectra of $LiNH_2$ (right) under the different computational conditions considered here. The experimental peak value is marked with a vertical dotted line.

There is a remarkable agreement among the calculations with a different number of beads (see fig. 3.9 and table 3.3), indicating that quantum effects are not observable in the predicted chemical shifts. Furthermore, the proton chemical shifts computed for point particles do not differ from the average chemical shift taken over the spatial proton densities obtained via the path integral scheme.

The ^{1}H NMR chemical shifts obtained with the Li atoms on the (Xray-based) well-ordered lattice positions are of the order of -10ppm, which considerably deviates from the experimental value. In turn, our configurations with disordered lithiums obtained from the molecular dynamics simulations yields proton chemical shifts of -5ppm, which agrees very well with the experimentally observed NMR resonance.

Beads	Ch. shift Li_2NH [ppm]	$LiNH_2$ [ppm]
1 (Class.)	-5.07 ± 1.42	-1.55 ± 0.82
4	-	-1.22 ± 1.37
6	-5.15 ± 1.48	-
6 (Centroids)	-5.14 ± 1.35	-
16	-5.84 ± 1.58	-0.72 ± 1.78
16 (Centroids)	-5.75 ± 1.36	-
16 (Fixed Li,N)	-10.61 ± 0.75	-
32	-5.30 ± 1.18	-
64	-5.01 ± 1.33	-

Table 3.3: Calculated chemical shift in Lithium imide and amide.

The correlation between the NH bond angle and the ^{1}H NMR chemical shift is shown in fig. 3.11, for Li atoms positioned on the fictitious crystal lattice sites (right) and relaxed to their equilibrium coordinates (left). Since the system is inversion-symmetric, the orientations θ and $90° - \theta$ point in opposite directions but are otherwise equivalent. This is reflected in the probability densities $P(\theta, \delta)$ which are approximately symmetric with respect to $\theta = 90°$. The plot illustrates on one hand that the amplitude of the angular oscillations is somewhat stronger after equilibration of the Li atoms, i.e. the probability diagram exhibits more scattering. Also for the chemical shifts, the distribution is considerably broader in the relaxed state. But on the other hand, no clear correlation between the ^{1}H NMR chemical shift and the NH orientation is visible, although the numerical shift values differ significantly (by about 5ppm) between the hypothetical fixed-lithium and relaxed-lithium calculations. This indicates that the dominant origin of the shift variations are the NH bond length fluctuations. In turn, the absolute value of the NMR resonance depends most strongly on the electrostatic environment determined by the relative lithium positions with respect to the nitrogen lattice.

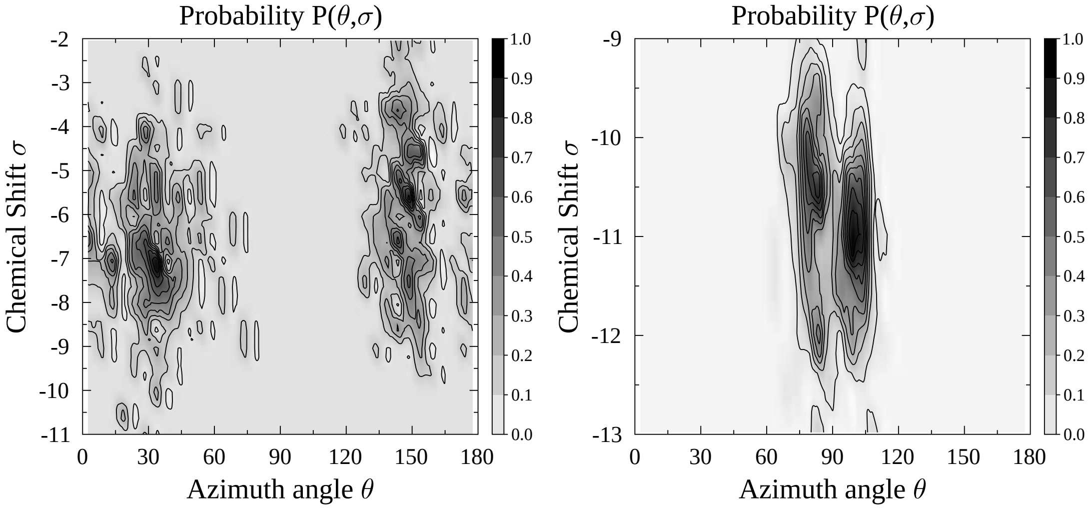

Figure 3.11: Correlation between the computed ^{1}H NMR chemical shift and the instantaneous NH angle θ in Li_2NH with the Li atoms on equilibrated (left) and the fixed crystal lattice positions (right). The probability density $P(\theta, \delta)$ reflects the inversion symmetry of the Li_2NH system (i.e. the orientations θ and $90° - \theta$ point in opposite directions but are otherwise equivalent).

3.2.4 *Diffraction Patterns*

Complementary to the first-principles simulations and the experimental and ab-initio NMR results, the powder diffraction patterns from the initial (“regular”) and relaxed structures of the Li_2NH crystal were computed recently[6]. The additional Li and H disorder in the fully relaxed configuration (third plot, top down), yields additional reflections (specially at $2\Theta \approx 18°$

and 32°), which are absent in the patterns obtained from the unrelaxed structures. While our computed intensity for the peak at $2\Theta \approx 18^\circ$ is considerably higher than the corresponding experimental one, the signal at $2\Theta \approx 35^\circ$ is well reproduced. Most importantly, both peaks are absent in the unrelaxed structures. This further support our findings, in particular regarding the lithium sublattice.

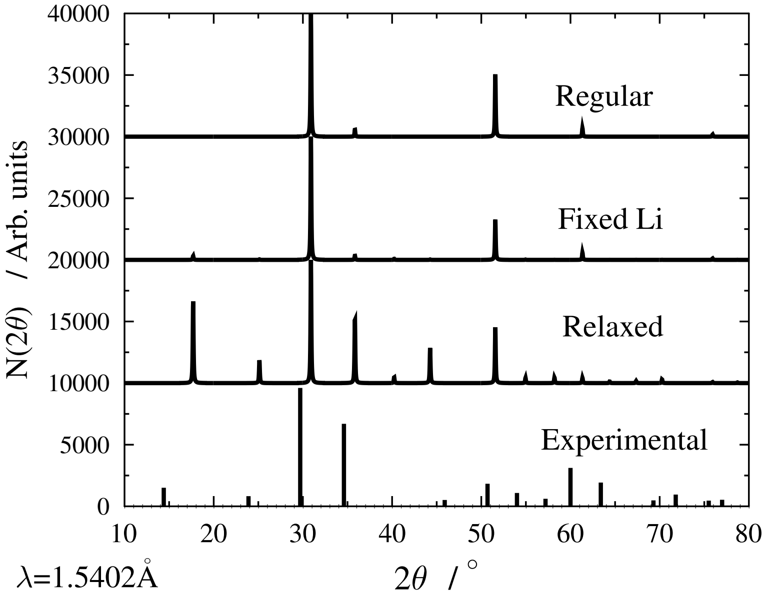

Figure 3.12: Comparison of X-ray diffraction patterns of Li$_2$NH computed for the theoretical structures (top three plots) and from experiment [6].

3.3 Quantum properties of protons in Li$_2$NH

Under ambient conditions, most atoms can normally be approximated as point particles, and this approximation yields a good level of accuracy for most properties. However, in the case of hydrogen, nuclear quantum effects can be observable due to its low atomic mass. In some compounds, hydrogen has been reported to exhibit quantum properties, such as tunneling and quantum delocalization [5, 118]. These effects might also play a role in industrially relevant situations, such as hydrogen storage [95]. Besides this special aspect, understanding the nature of quantum effects of hydrogen in bulk materials is a matter of high fundamental and general relevance.

A particularly intriguing finding is the possibility of quantum delocalization of the protons over several possible sites, as a consequence of the relatively flat potential energy landscape in the highly symmetric structure [123]. However, as shown in the previous sections, the structure at ambient temperature differs from the one previously assumed [71, 77].

In this section, the possibility of quantum delocalization of protons in the Li_2NH bulk in the condensed phase is tackled by studing the particle density obtained from the ab-initio PIMD simulations. A comparison with the behavior of the isolated Li_2NH and methanol (CH_3OH) molecules is also provided.

3.3.1 *Quantum particle density*

The quantum particle density resulting from our PIMD simulations is presented in fig. 3.13, right. The figure shows the superposition of the beads from 5 ps of a PIMD trajectory (32 beads, 300 K). Each individual quantum proton density forms a torus of radius $r \approx 0.5$ Å with an homogeneous proton distribution. However, this distribution has a statistical character. From this distribution alone, it cannot be derived if the proton being delocalized or moving as a localized particle in a torus-shaped potential well.

In order to discriminate the two scenarios, the potential land-

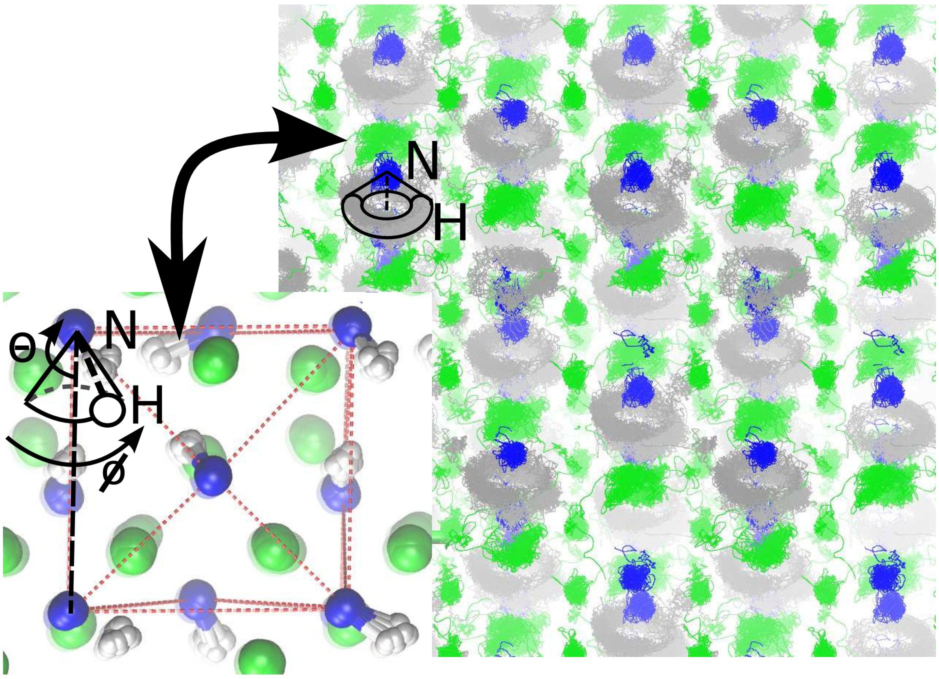

Figure 3.13: **Left:** Li$_2$NH converged structure. The Li lattice is disordered and the N lattice is FCC. The N-H bonds precess around a preferred N-N axis while keeping $\pm 30^\circ$ respect to that axis. **Right:** The Quantum particle density of the Li$_2$NH system, as obtained from PIMD simulations at 300 K.

scape along the precession angle of the protons has been computed (ϕ, sketched in fig.3.13). The potential $\bar{E}_{KS}(\phi)$ was obtained by averaging over all degrees of freedom other than ϕ, based on an ensemble of about 50000 individual configurations. The procedure can formally be expressed as follows: The potential energies of the individual configurations are obtained after an optimization of the electronic wavefunctions, each yielding a set of values $\{E_{KS}, \phi_1, \phi_2, \phi_3, \phi_4\}_\tau$, where τ is the labeling of the individual configuration (four angles per replica are obtained, as the calculation is realized with four NH bonds per unit cell). Then, the energy as a function of the azimuthal angle is obtained by averaging the configuration energies as

$$\begin{aligned} n(\phi,\tau) &:= \frac{\sum_{i=1}^{4}\delta(\phi_i(\tau)-\phi)}{\sum_\tau \sum_{i=1}^{4}\delta(\phi_i(\tau)-\phi)} && (3.2) \\ \bar{E}_{KS}(\phi) &= \sum_\tau E_{KS}(\tau) n(\phi,\tau)\,, && (3.3) \end{aligned}$$

where i is the index of the particular NH bond in an individual snapshot. Using this procedure, the orientation of the other NH bonds in the system is effectively averaged.

In figure fig. 3.14, the resulting potential $\bar{E}_{KS}(\phi)$ is shown. It varies by less than 0.8 mHa as a function of ϕ, which is in the order of the thermal energy $k_B T$ at $T = 300$ K. However, the distribution of individual energies $E_{KS}(\tau)$ has an almost constant standard deviation of 8 mHa for all angles ϕ, that is, ten times the maximal variations of $\bar{E}_{KS}(\phi)$. This indicates that the effective potential for hydrogen motion along the torus is most likely very flat.

In the procedure followed to obtain the potential energy (eqs. 3.2, 3.3), we have assumed that the energy of an individual NH bond azimuthal angle is uncorrelated from the orientation of the rest of the bonds, i.e. there is no concerted rotation of the NH bonds. In order to check this assumption, the correlation between pairs of azimuthal NH bond angles (ϕ_i, ϕ_j) was calculated. In figure fig. 3.15, two plots of the joint probability for the ϕ angles of NH bond pairs is presented. The plots show that the probability is scattered over all possible angle pairs. This indicates that the orientations of different NH bonds are essentially uncorrelated. Hence, we conclude that the individual NH protons precess in an uncorrelated way on a mainly flat potential energy landscape.

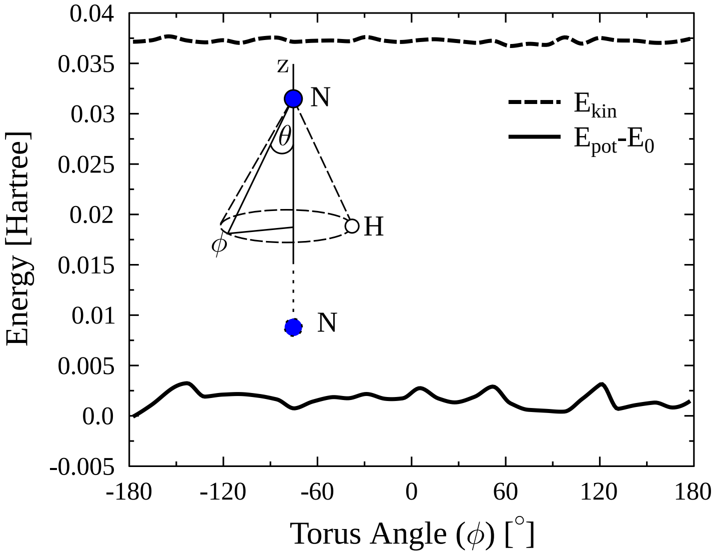

Figure 3.14: Dependence of the averaged Kohn-Sham energy on the azimuth angle ϕ (sketched in figs. 3.13 and 3.17). The error bars show the statistical standard deviation for a given angular range.

3.3.2 *Proton delocalization in isolated molecules*

As a mean for comparison with simpler systems, additional PIMD simulations of the isolated Li_2NH and CH_3OH molecules at 300 K were performed. In fig. 3.16, the obtained quantum particle densities are shown for both molecules.

The NH bond in the isolated Li_2NH molecule shows a different behavior to the bulk Li_2NH, as the molecule converges to an essentially flat and rigid configuration. The final proton density is localized for all particles in the molecule (see fig. 3.16d).

The case of CH_3OH is particularly interesting since the OH proton can freely rotate around the C-O axis, and therefore it experiences a situation similar to the NH protons in bulk Li_2NH. As shown in fig.3.16a, the particle density of the OH proton resembles a torus of radius ∼0.9 Å. In this respect, the proton density distribution looks very similar to the one observed in bulk Li_2NH. Conversely, the protons forming CH_3 are localized due to the repulsion exerted between them. There is, however, a small but noticeable correlation between the density of the OH proton and the orientation of the CH_3 protons (figs. 3.16b,c), due to the proton-proton repulsion.

The shape of the proton distribution in CH_3OH (fig. 3.16) might be expected, however, they illustrate qualitatively that even a small interaction (such as between CH_3 and OH protons) can lead to a visible signature in the proton density distribution, as seen in fig. 3.16c.

The remaining question is if the motion of the protons in imaginary time is a fully "classical" precession or a statistical distribution of an *in principle* coherent delocalized quantum state (which at high temperatures may form a wavepacket). In the following, a study the delocalizaton of the ring polymer in PIMD imaginary time is done, with the aim of finding evidence supporting one of this two possibilities.

In order to quantify the proton ring polymer (de-)localization with respect to the azimuthal angle, the arc distance of bead p to its centroid is computed as

$$\begin{aligned}\Delta arc_{\phi}{}^{(p)}(t) = r^{(p)}(t)\sin(\theta^{(p)}(t))\phi^{(p)}(t) \\ - r_C(t)\sin(\theta_C(t))\phi_C(t)\,,\end{aligned} \tag{3.4}$$

where C indicates the centroid of the ring polymer, and $r^{(p)}$, $\theta^{(p)}$, $\phi^{(p)}$ are the coordinates of the NH bond in a given replica p. In fig. 3.17, the distribution of arc distances during the whole PIMD trajectory for the protons in bulk Li_2NH and CH_3OH is shown. From these distributions, the arc half-width of the proton ring polymers, which we define as the standard deviation of the arc distances distribution ($\sqrt{\langle \Delta arc^2 \rangle - \langle \Delta arc \rangle^2}$) is extracted. We want to remark that the width of the ring polymers at high temperature is dominated by the strong harmonic forces between beads, which are proportional to $mPT^2||\mathbf{R}^{(p)} - \mathbf{R}^{(p+1)}||$. The effect of the external potential in the ring polymer width is therefore expected to be subtle. The arc half-widths obtained are 0.117 Å for the protons in bulk Li$_2$NH (16 beads, 300 K), 0.093 Å for the OH of CH$_3$OH (32 beads, 300 K), and 0.087 Å for the (localized) organic protons in CH$_3$OH (32 beads, 300 K). It is remarkable that the ring polymer angular distribution of the organic protons in CH$_3$OH is only 6.5% narrower than the corresponding to the mobile OH proton, which is not subjected to a confining potential in that angle. When comparing the arc half-widths in the tori for both materials, the angular distribution of the protons in bulk Li$_2$NH turned out to be 26% wider than the OH proton in CH$_3$OH. This narrower distribution in CH$_3$OH may be consequence of the previously mentioned correlation of the OH with the CH$_3$ protons. More importantly, the much wider distribution in Li$_2$NH indicates that the bulk Li$_2$NH protons are exposed to a considerably more flat potential landscape than those in CH$_3$OH.

The flatness of the potential landscape in which Li$_2$NH protons are found is an important evidence supporting proton quantum delocalization in that material.

3.3.3 *Convergence of the bead distribution's width*

In order to test the convergence in the dynamics of the bead distribution width, we calculated the width $\mathcal{W}(t)$ of a particle's ring polymer at simulation time t,

$$\mathcal{W}(t) = \sqrt{\frac{\sum_{p=1}^{P} ||\mathbf{R}^{(p)}(t) - \mathbf{R}_C(t)||^2}{P}} \tag{3.5}$$

where P is the number of beads, $\mathbf{R}^{(p)}(t)$ and $\mathbf{R}_C(t)$ are the position of the pth bead and the centroid at time t, respectively.

Beads	6	16	16 (Fixed Li)	32	64
$\mathcal{W}(t \gg 0)$	0.11	0.10	0.11	0.11	0.12

Table 3.4: Proton beads distribution converged width $\mathcal{W}(t \gg 0)$ in lithium imide at 300 K for different number of beads (in Å).

The time evolution of the width $\mathcal{W}(t)$ during the initial stage of the simulation is presented in fig. 3.18. The convergence of the initially delocalized proton beads is observed to occur in a timescale of 0.3 ps. The width $\mathcal{W}(t)$ is afterwards essentially constant, and its final average value is independent of the number of beads used (see table 3.4). As the width of the beads distribution is converged in such short time scale, we can safely study the ring polymer dynamical properties in the whole of our production trajectories.

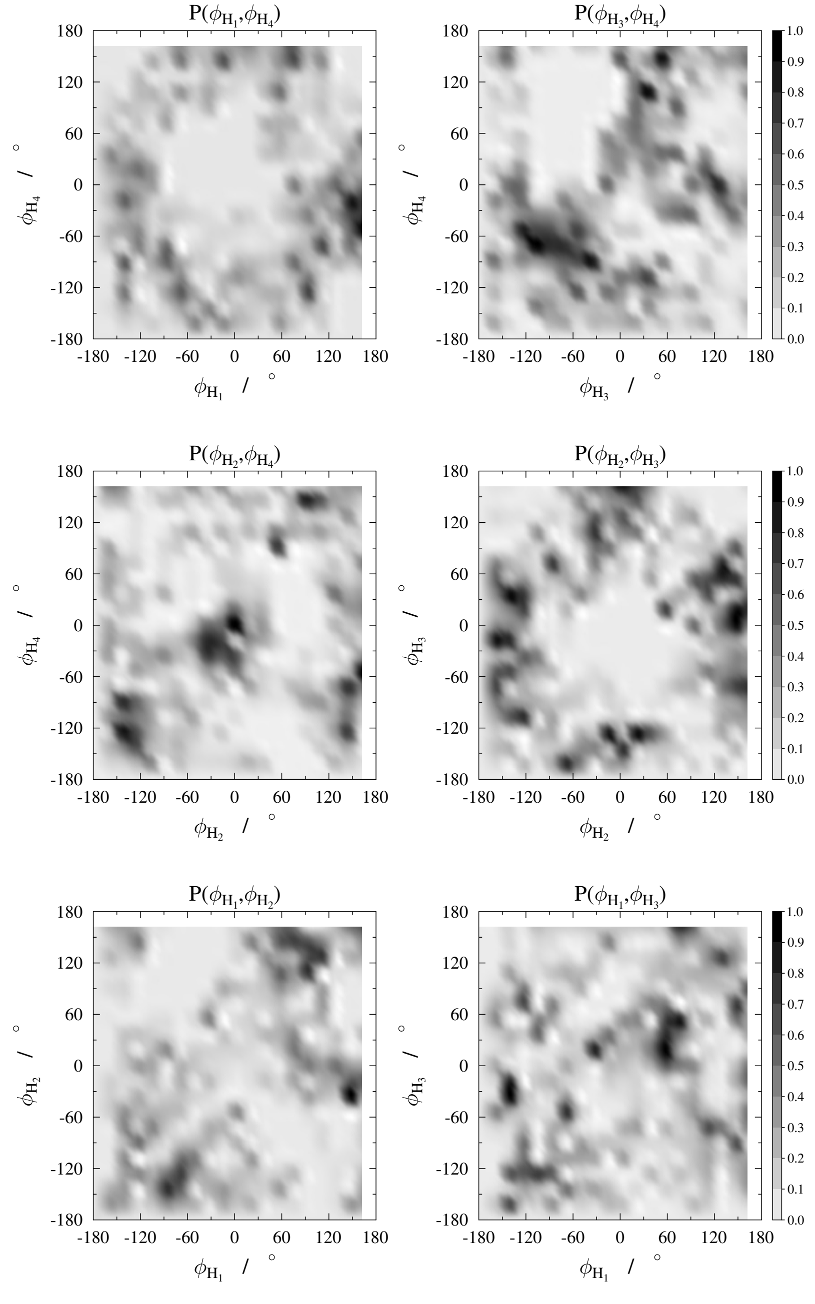

Figure 3.15: Joint probability of the azimuth angle ϕ around the precession axis between NH bond pairs in the Li$_2$NH bulk.

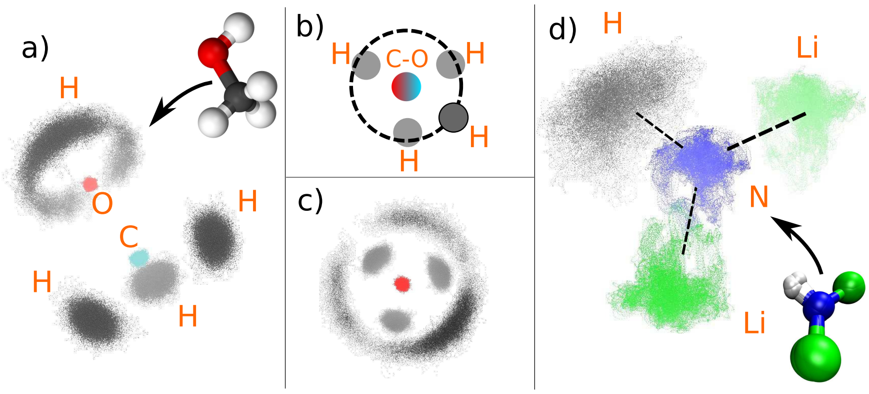

Figure 3.16: Quantum particle density obtained from PIMD calculations for: **a)** CH_3OH molecule, **b)** and **c)** CH_3OH view from the CO axis, and **d)** Li_2NH molecule. Colors: H atoms in *black*, Li in *green*, N in *blue*, O in *red*, and C in *cyan*.

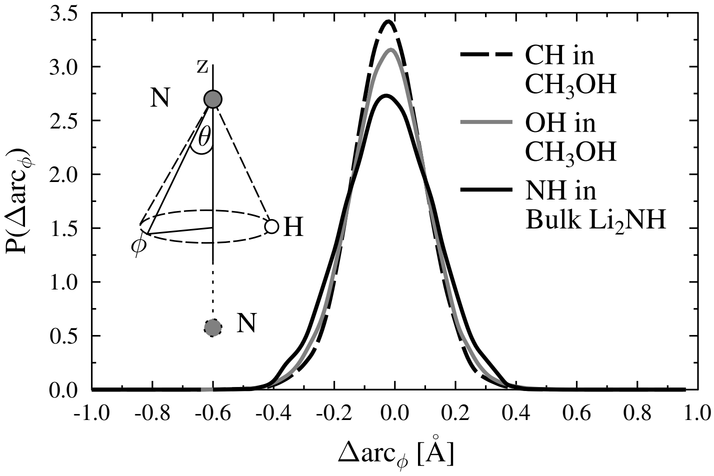

Figure 3.17: Distribution of arc distances to the centroid in the azimuth angle ϕ (see inset), for the protons in bulk Li_2NH, in the CH bonds of CH_3OH, and in the OH bond of CH_3OH.

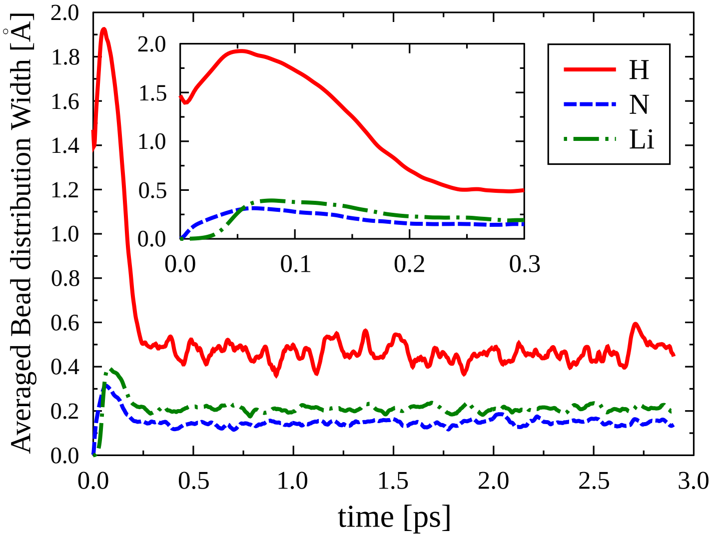

Figure 3.18: Beads distribution width $\mathcal{W}(t)$ for the initially delocalized configuration of Li$_2$NH, during the first picoseconds of a simulation ($P = 32$, $T = 300$ K). The inset is a zoom to the first steps, showing how the initially highly delocalized proton beads collapse rapidly to a more localized distribution.

3.4 Conclusion

In this chapter, the present structural picture of lithium amide/-imide compounds on the atomic scale has been critically revised. The local conformation of these systems is crucial for the understanding of the actual microscopic hydrogen uptake and release processes, which are presently one of the main drawbacks of this class of materials for efficient hydrogen storage devices. The possibility of proton quantum delocalization in bulk lithium amide was also studied by means of path-integral molecular dynamics.

The use of first-principles path integral molecular dynamics simulations provided evidence for a pronounced local disorder of the lithium sublattice, which is consistent with the observed high Li diffusion constant but which is not visible in X-ray and neutron diffraction experiments and therefore was not considered in previous structural models. Furthermore, the orientations of the hydrogen atoms in Li_2NH relative to the stable nitrogen lattice were elucidated, and these geometric parameters were related to the ^1H NMR chemical shifts. The values obtained from the first-principles predictions at ambient temperature are in good agreement with the experimental data. On the other hand, our path integral calculations did not exhibit strong effects of proton quantum delocalization on these spectra.

The possibility of quantum delocalization in Li_2NH was analyzed by means of path-integral molecular dynamics (PIMD). Despite the lack of influence of quantum effects in the ^1H NMR signal, our computational study suggests the plausability of an emergence of quantum delocalization of protons in the bulk

Li_2NH. The protons in Li_2NH were found to be in a toroid-shaped potential well. The virtually flat potential with respect to the azimuthal angle leads to a quantum delocalization of the NH protons over the torus, which can still be partially observable at ambient temperatures.

Chapter 4

High Temperature Proton Conduction: The Case of Poly[vinyl Phosphonic Acid]

In the previous chapter, we have studied a material which can potentially solve the problem of energy storage and transport. In this chapter the problem of energy conversion is addressed, more precisely the membrane material of a proton exchange membrane fuel cell (PEMFC).

As mentioned in sec. 1.1, the semipermeable membrane is one of the central functional elements of a fuel cell. This membrane allows only ions of a given kind to travel from one electrode to the other, while blocking the migration of all other particles. For the case of a polymer electrolyte membrane (PEMFC) (sec. 1.1), it consists of a polymeric film that is permeable for protons but jams the diffusion of neutral and anionic particles (in particular H_2, O_2, OH^-) as well as electrons.

There are some polymers that exhibit the aforementioned functionality, of which the most widely used is Nafion(R). It consists of a hydrophobic polymer matrix with hydrophilic endgroups. In the presence of abundant amounts of liquid water, this polymer swells and creates percolation pathways of bulk water channels through the material. These water channels solvate the acidic protons from the polymer, and thus enable long-range proton transport through the entire membrane along the hydrogen-bond network of the water molecules. The transport mechanism of such acidic bulk water systems has been investigated in depth in a series of experimental [104, 108, 98, 57, 58, 86, 109, 43, 46, 72, 97, 48] and computational works [25, 10, 73, 117, 114, 113, 32, 9, 84, 83, 21, 121].

Generally, the conduction mechanism in bulk-water channels is based on the *Grotthuss mechanism* [18], in which a succession of proton jumps along a hydrogen bond chain of water is followed by a local rearrangement of the molecules. This rearrangement in turn allows the next collective jump event. An alternative transport scheme is the *vehicle mechanism*, which implies that an excess proton is bound to a given host molecule, which travels through the surrounding solvent as an entity. While these particular transport mechanisms are well understood by now, they apply mostly to homogeneous systems such as bulk liquids, e.g. regular water. However, the atomistic processes in more heterogeneous environments can naturally differ from these relatively simple pictures.

The presence of bulk water channels limits the operating temperature of a fuel cell to the boiling temperature of water. This is a big limitation, since the efficiency and lifetime of the fuel cell could be greatly increased if the temperature could be raised. This increase is mainly due to another key problem in the fuel cell implementation, which is not directly addressed in this thesis: the problem of the catalysis of H_2 (sec. 1.1). Today, the most used catalyst is a thin layer of platinum in the membrane surface. The catalysis is strongly hindered by CO poisoning of this layer, which would be significantly avoided with higher working temperatures, due to the higher activity of the catalyst. An increase of the operating temperature could possibly even lift the need of a precious metal as a catalyst, as cheaper catalysts (e.g. the Fe-based) could have enough efficiency.

In this chapter a promising proton conducting polymer for mid-high temperatures is studied: Poly-[vinyl phosphonic acid] (PVPA) [28, 3, 89, 2, 85, 64, 65, 45, 108, 119].

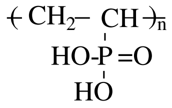

$$\left(\mathrm{CH_2-}\underset{\underset{\underset{\displaystyle\mathrm{HO}}{|}}{\mathrm{HO{-}P{=}O}}}{\underset{|}{\mathrm{CH}}}\right)_n$$

The intended temperature range of a PVPA-based fuel cell would be above the boiling point of liquid water and therefore implies the absence of bulk water channels available for either vehicle conduction or conduction by Grotthus mechanism within water channels. However, it was experimentally confirmed that a sharp decay of the ionic conductivity occurs when the material is highly dried. Nevertheless, a considerable level of proton conduction is observed up to temperatures of 416 K [45], although the absolute conductivity is not yet at the level of industrial usability. This results hint that water indeed does play an important role in proton conduction within PVPA, despite the absence of bulk water channels. Therefore, the relevance of water might come from to the intercalated water molecules (as a kind of "crystal water"), which can remain in the system at temperatures higher than bulk water. Understanding the process of proton conduction, and in particular the function of intercalated water molecules, becomes therefore highly relevant for further improving the properties of this material, and is the main question to be answered in this chapter.

Computational studies of proton conducting materials often put the emphasis on the statistical properties of the natural proton dynamics in the equilibrium system, for instance the rate of proton hopping or the energetics of bond distances [119, 114]. Although these properties are of high relevance for the possible occurrence of proton conduction, the macroscopic properties of the system are normally determined by unbalanced situations, such as the concentration gradient of protons in a fuel cell. Furthermore, the macroscopic relevance of local jump processes is reduced due to the problem of forth-and-back hopping. The latter does not contribute to physically observable conduction, which requires long-range transport of charge carriers.

The main question addressed in this chapter is that of elucidating which are the main contributions to proton conduction in this material, ultimately explaining the loss of conductivity in PVPA when the system is highly dried. To this end, a series of first-principles molecular dynamics simulations of long-range proton transport in PVPA was carried on. This simulations include excess protons and an external driving force to mimic the potential difference given by the electric field and the proton concentration gradient in the real system. Then, the resulting net motion of the charge carriers is studied and quantified by means of a specifically designed collective variable, in the spirit of the meta-dynamics scheme [62, 40, 39, 38]. This description gives access to the proton conductivity σ and the microscopic conduction mechanism of the polymer as a function of environmental conditions such as temperature and water content. As an outcome of this work, the main results presented in this chapter are also presented in [69].

4.1 Setup

The calculations were carried out using the accelerated Car-Parrinello-like molecular dynamics method of Kühne et al. [59] (section 2.2.4), implemented within the mixed gaussian and plane-wave code CP2K/Quickstep [66, 120]. For the former, an accurate triple-ζ basis-set with an additional set of polarization functions (TZVP) [94] is used, while for the latter a density cutoff of 280 Ry is employed. The interactions between the ionic cores and the valence electrons are described by norm-conserving pseudopotentials [27] (sec. 2.1.7), whereas the exact exchange and correlation energy is approximated by the BLYP functional. Furthermore, the equations of motion are integrated by a finite timestep of $0.5fs$.

A simplified model of PVPA has been used in our simulations: Four independent linear (syndiotactic) PVPA strands were placed hexagonally with mutual distances of 8Å under periodic boundary conditions, yielding a unit cell of volume $\Omega = 10.25 \times 13.86 \times 16\text{Å}^3$. Despite being a fairly simple model for a real polymer, in which many relevant features like tacticity, polymer topology or density fluctuations were omitted [8], it has been successfully used to obtain a realistic representation of the hydrogen bonding network and the local polymer topology [64, 65]. As we are to study the hydrogen bonding network dynamics during proton conduction, related to short

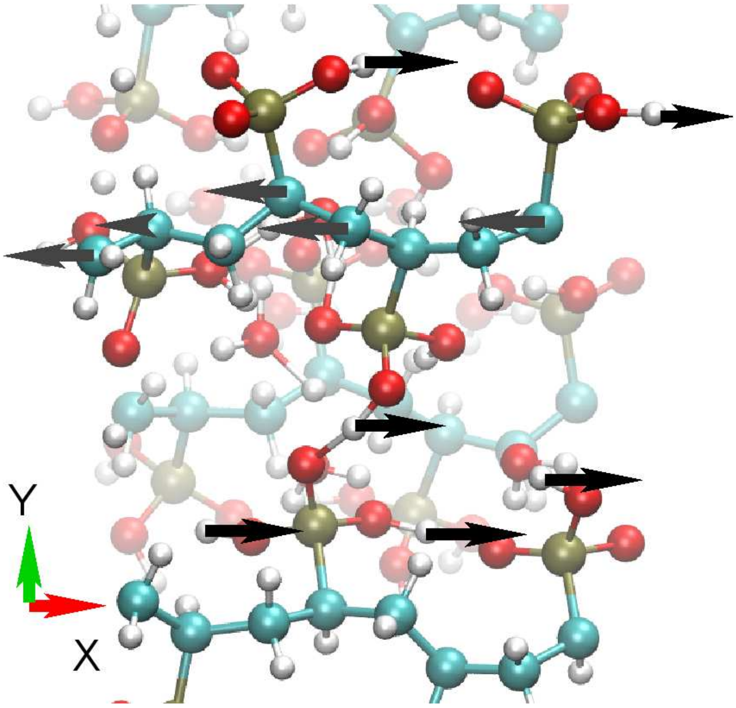

Figure 4.1: Representations of the model system for PVPA. The arrows indicate the external force bias applied (see text).

range jumps, this simplified setup is expected to deliver reliable results. It is to be stressed that the study does not aim at an explanation of the whole conduction process, but rather only at the dynamics of bonding (proton jumping). Other processes, where the topology of the polymer plays a decisive role, fall out of the scope of the study.

Following experimental estimates of the water content [49], the polymer model is complemented by two and eight individual water molecules intercalated between the polymer chains, which are referred to from now on as “dry” and “wet” PVPA. The system is further doped with one and two excess protons for the dry and wet models, respectively.

In ab-initio simulation timescales (picoseconds), the actual process of proton conduction would not be observable without an external driving force. Therefore, a constant force bias $\mathcal{F}$ is selectively applied to acidic protons, together with a compensating counterforce applied to the carbon atoms of the polymer backbone (sketched in fig. 4.1). The backbone (C atoms) was chosen instead of O or P atoms because the counterforce is intended to interfere minimally on the system while eliminating the net external force on the system. The magnitude of this force should be large enough to yield a sizeable ionic current, but it should not interfere with covalent bonding within the system. As in our calculations an MD run with $F \sim 200$ pN led to the breaking of a P-O bond, so that further simulations are restricted to $1 \ldots 100$ pN. Forces below this range turned out to have no detectable influence on the hydrogen dynamics, at least on our simulation timescales. The external bias force leads to a systematic translational motion of the excess protons in the system, which is to be quantified, as it will be discussed in sec. 4.3.

4.2 Dynamics of Proton hopping

In order to characterize the dynamics of the hydrogen bonding network, a state vector is defined as

$$\mathbf{H}(t) = \{H_1(t), \cdots, H_k(t), \cdots, H_N(t)\}\ , \tag{4.1}$$

with $H_k(t) = j$ if proton k is H-bonded to oxygen j at time t (and $H_k(t) = 0$ if there is no hydrogen bond). This definition contains all information about which hydrogen atom is bonded to which oxygen atom. Based on this vector, the H-bond-network correlation function $\eta(t)$ is defined via

$$\eta(t) = \sum_k \tilde{\delta}_{H_k(t),H_k(0)} \,, \tag{4.2}$$

where $\tilde{\delta}$ represents a modified Kronecker function which is also zero if either $H_k(t)$ or $H_k(0)$ is zero. The function is to be averaged over many starting points in order to eliminate dependence on the chosen initial state. This definition accounts for the decay of the initial state of the network: if the bonding network has changed due to a proton jump, the η function will decay by $\Delta\eta = -1$, while if one proton jump restores a bond from the initial state, the function will increase by $\Delta\eta = +1$. This correlation function is less sensitive to forth-and-back jumps of protons between donor and acceptor oxygens compared to a simple calculation of the proton hopping events. These oscillatory forth-and-back jumps occur very frequently in the md simulations but are not relevant for sustained proton conduction.

Fig. 4.2 shows the averaged curves of the decay of $\eta(t)$. This decay characterizes the number of jumps taking place per unit of time on each system. The initial decay rate, calculated as the numerical derivative of $\eta(t)$ after 0.1 ps,

$$\frac{1}{\tau_H} \equiv -\frac{1}{\eta(0)} \left[\frac{\Delta\eta}{\Delta t}\right]_{t=0}^{t=0.1\mathrm{ps}} \,, \tag{4.3}$$

was taken as the characteristic value for the jump rate, and is presented in table 4.1. A constant decay rate for the whole timescale cannot be presented, as it evolves time, being the decay law of the $\eta(t)$ a function governed by several parameters (this is treated in sec. 4.2.1).

T [K]	$\frac{1}{\tau_H^{\mathrm{w}}}\left[\frac{1}{\mathrm{ps}}\right]$	$p^{\mathrm{w}}_{\mathrm{H_2O}}$	$\frac{[H_3O^+]}{[PO_3H_3^+]}$	$\frac{1}{\tau_H^{\mathrm{d}}}\left[\frac{1}{\mathrm{ps}}\right]$	$p^{\mathrm{d}}_{\mathrm{H_2O}}$	$\frac{[H_3O^+]}{[PO_3H_3^+]}$
100	0.0310	95.7%	.680	0.0525	86.2%	.651
300	0.0320	26.5%	.011	0.2721	24.8%	.178
400	0.2379	42.7%	.341	0.1490	73.4%	.259
500	0.2888	48.5%	.182	0.2516	7.1%	.014
600	0.2178	47.9%	.180	0.5266	56.6%	.553

Table 4.1: From left to right, the decay rate of the hydrogen bond network after 0.1ps ($1/\tau_H \equiv -\frac{1}{\eta(0)}\left[\frac{\Delta\eta}{\Delta t}\right]_{t=0}^{t=0.1\mathrm{ps}}$), the ratio $p_{\mathrm{H_2O}}$ of jumps per excess proton involving a water molecule (normalized to water concentration), the ion concentration ratio $[\mathrm{PO_3H_3^+}]/[\mathrm{H_3O^+}]$ (normalized to the respective concentrations of water and phosphonic groups). All properties are presented for the wet (left) and dry (right) PVPA under different temperatures and an external force bias of intensity $F = 30$ pN.

Surprisingly, the wet and dry setup yield similar decay rates for most temperatures. This very mild temperature dependence indicates that the effective jump barrier is not the rate-limiting quantity, but that it is rather the arrangement of the donor-/acceptor oxygens which determines whether a successful jump occurs. In the 300 K case (wet system) the system is trapped in a local minimum of the configuration potential for the most of the simulation time, i.e. the excess proton was not able to reach the water vehicle, thus hindering the dynamics of the protons in the system. The effect can be seen in the correlation of unusually low conductivity σ (see section 4.3, table 4.3) with the also unusually low concentration ratio $\frac{[H_3O^+]}{[PO_3H_3^+]}$ and jump rate $1/\tau_H$.

Throughout the calculations, proton jumps do not occur at a constant rate, but rather in events of many coordinated jumps, followed by long periods without relevant activity.

The rate of jumps to or from a water molecule normalized to the number of available water molecules tends towards 40-50% in the wet system (table 4.1), while no trend was observed in the dry system. The concentration of hydronium ions relative to charged phosphonic groups (again, normalized to the respective concentrations of water and phosphonic groups), is about 20% in the wet system and generally under 50% in the dry at high temperatures. This indicates that the excess protons jump approximately with the same probability to a water or to a phosphonic group, but forming H_3O^+ only briefly, effectively using water molecules as a bridge to hop between the phosphonic groups where they stay most of the time (fig. 4.3).

The apparently inverse $\frac{[H_3O^+]}{[PO_3H_3^+]}$ ratio is due to the much higher concentration of acid groups with respect to water [79].

4.2.1 *On the decay law of* $\eta(t)$

As can be seen in fig. 4.2, the decay function $\eta(t)$ (defined at the beginning of this section) is better fitted for long simulation times by an stretched exponential law,

$$\eta(t) = Aexp[-(t/t_0)^\gamma]\,, \tag{4.4}$$

(see fitting parameters in table 4.2). Although this is not a very usual decay law, it has been previously observed in some systems, generally associated with disorder [90, 20]. In order to explain its emergence in this system, a model for the hydrogen bonding network of PVPA was created (see fig. 4.4). In this model, the polymer is thought as a network of N phosphonic groups, where each group consists of three (labeled) H sites. In every step, two of the three sites in each group are occupied by a hydrogen, and every hydrogen is also labeled. Then, one excess proton is added to a randomly chosen group. Finally, one proton in the charged phosphonic group (i.e. that with the three sites occupied) is randomly chosen and is assigned to a new phosphonic group, thus representing a proton jump. This hopping procedure is then iterated for the newly formed hydrogen network.

The decay of the hydrogen bonding network was tested in this model using different rules for proton hopping. In figure 4.5, the resulting decay function $\eta(t)$ for five different hopping rules is shown. Each curve was obtained from averaging the decay function of a number of 400 runs with 1000 phosphonic groups each. The extreme case where the rule allows to randomly choose any phosphonic group independently of its distance showed an exponential decay. This can be expected, since with this hoping rule the probability to hop back to a previous configuration is negligible for large network. Then, if in each step the probability of a group to have the excess proton is $P \in [0, 1]$, the corresponding probability after t steps will be $P^t \equiv exp(-\alpha t)$. The corresponding $\eta(t)$ function being then $\eta(t) = Nexp(-\alpha t)$, where N is the total number of sites ($N \to \infty$). Another way to see it is that the decay in the $\eta(t)$ function in each step is directly proportional to its value:

$$\frac{\mathrm{d}\eta(t)}{\mathrm{d}t} = -\alpha\eta(t)\,, \tag{4.5}$$

thus obtaining again an exponential decay, $\eta(t) = Aexp(-\alpha t)$.

In the cases where only 1st and 2nd neighbor jumps where allowed (including cases where a probability of not jumping was added), an stretched exponential was the best fit to the decay function (see fig. 4.2). It is remarkable that this decay arises independently of the introduction of a probability of not jumping, thus the jumping rate may change the power of the exponent (γ), but will still be stretched exponential; it is a property imposed by the system and not by the jumping rate.

This decay law can be explained because of the fact that the probability of returning to a previous configuration with the selected hopping rules is bigger than in the case of a random jump over the whole network. In these cases, the probability of turning back to a previous state increases as the system evolves and the excess proton explore further regions of the network. The change in the $\eta(t)$ function in each step can therefore be thought as inversely proportional to some function monotonically increasing with time. With a good level of generality, this function can be chosen to be a power of time, where the power is a parameter to fit.

$$\frac{\mathrm{d}\eta(t)}{\mathrm{d}t} = -\alpha\eta(t)/t^{\beta} \,. \tag{4.6}$$

The simplest case of $\beta = 1$ corresponds to a power-law decay

$$\eta(t) \propto 1/(t - t_0) \,, \tag{4.7}$$

which does not fit properly to the data. For the other values of β, the solution to the differential equation 4.6 is

$$\eta(t) = Aexp(-(t/t_0)^{\gamma}) \,, \tag{4.8}$$

where $t_0 = (\alpha\beta)^{-\beta}$ and $\gamma = \beta + 1$. The stretching exponent γ fits the decay function $\eta(t)$ better when $0 < \gamma \leq 1$, being $\gamma = 1$ the exponential decay of the random jump case previously mentioned.

This stretched exponential decay is typically found in the relaxation of disordered systems, and is associated with a decay occurring on all possible timescales [90], in other words, a typical half-life cannot be associated to any state (in our case H-bonds), because some states may remain for indefinite time and others be lost extremely quickly.

T	α_{w}	γ_{w}	t_0^{w}	α_{d}	γ_{d}	t_0^{d}
300	0.0042	0.1642	2.59×10^{14}	0.0604	0.4710	3.86×10^{2}
400	0.0423	0.2019	6.31×10^{6}	0.0392	0.3616	7.75×10^{3}
500	0.0663	0.4547	3.90×10^{2}	0.0599	0.3706	1.98×10^{3}
600	0.0349	0.2670	2.86×10^{5}	0.0979	0.1893	2.13×10^{5}

Table 4.2: Stretched exponential fitting parameters for 5 ps of the $\eta(t)$ for wet (w) and dry (d) PVPA under different temperatures. The parameters are $\eta(t) = \eta(0)exp[-\alpha t^{\gamma}] = \eta(0)exp[-(\frac{t}{t_0})^{\gamma}]$.

Alternatively, the emergence of a stretched exponential can also be associated with a superposition of many exponential decay functions, with a very particular weighing function:

$$e^{-t^{\gamma}} = \int_0^{\infty} du\, \rho(u)\, e^{-t/u} \ , \tag{4.9}$$

where

$$\rho(u) = -\frac{1}{\pi u} \sum_{k=0}^{\infty} \frac{(-1)^k}{k!} \sin(\pi\gamma k)\Gamma(\gamma k + 1) u^{\gamma k} \, . \tag{4.10}$$

However, there is no evidence suggesting such a distribution of individual exponential decays.

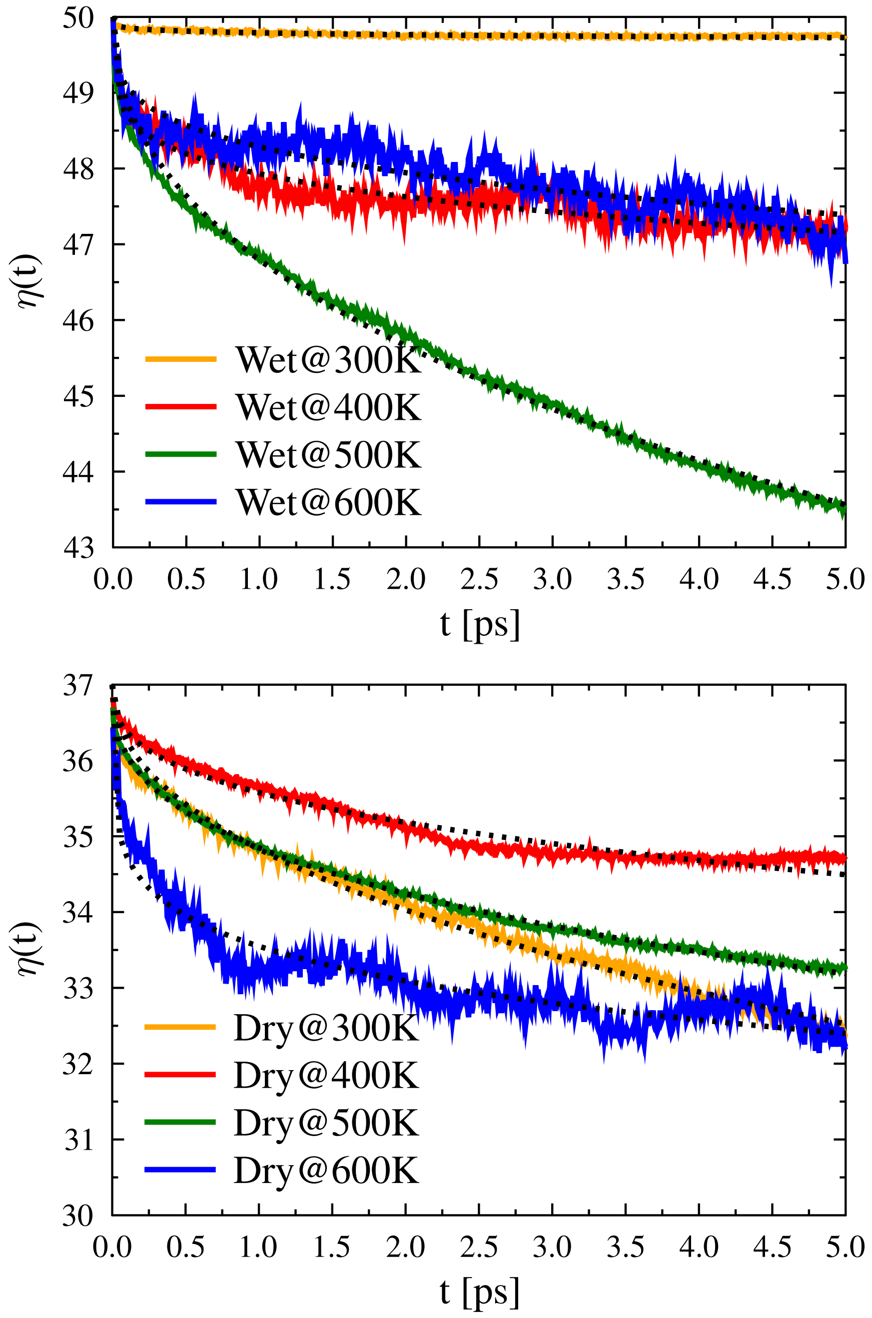

Figure 4.2: Decay function $\eta(t)$, for wet (up) and dry (down) PVPA. Curves are fitted to a stretched exponential (see sec. 4.2.1) with the parameters found in table 4.2.

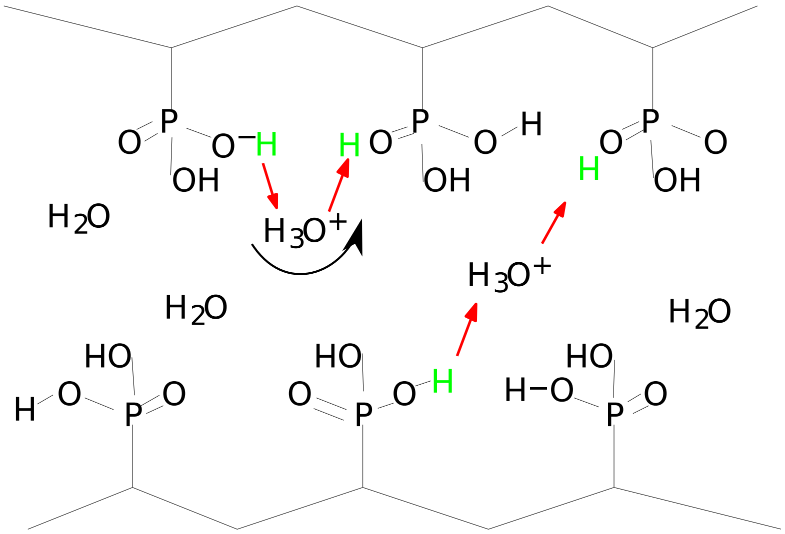

Figure 4.3: Water molecules bridge the proton sites, complementing Grotthuss proton hopping between phosphonic acid groups.

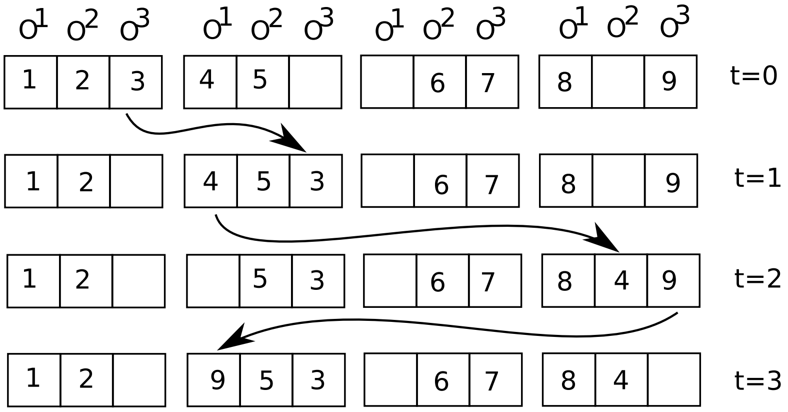

Figure 4.4: Four steps of the evolution of the hydrogen network model. In each step a proton is randomly chosen from the fully occupied phosphonic group and reassigned to another group (i.e. a jump). In the figure all the three represented jumps contribute to a decay of $\Delta\eta = -1$, including the last case, where the proton comes back to its initial group but in a different ordering (i.e. attached to a different oxygen).

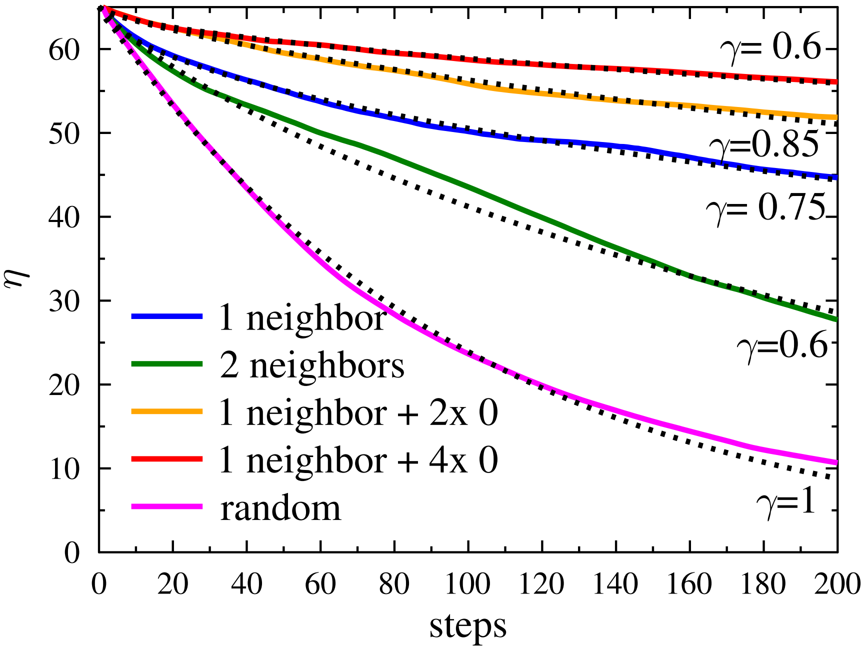

Figure 4.5: Decay function $\eta(t)$, for the simplified model. The different curves correspond to different hopping rules, these being **(random)** each step the excess proton can jump to any phosphonic group, **(1 or 2 neighbor)** the proton jumps randomly to a 1st/2nd neighbor, and **(1 neighbor +2x 0, or +4x 0)** hopping to a 1st neighbor but with a probability of not jumping, which is two/four times higher than that of a jump to a 1st neighbor.

4.3 Proton conductivity σ and the $\mathcal{Q}$ variable

Proton conduction is a macroscopically measurable property. The macroscopic displacement of current arises from subtle biases in the microscopical dynamics. Therefore, the property connecting the microscopic dynamics with the macroscopic property of conduction requires a careful design. In order to quantify the amount of proton conduction taking place in the system from the atomic motion, a collective variable $\mathcal{Q}$ was designed. This variable measures the integrated ionic current based on the atomic coordinates of acidic hydrogen, oxygen and phosphor atoms. It is defined as:

$$\mathcal{Q} := \sum_{\mathrm{H_{ac}}} \mathbf{R}_{\mathrm{H}} + w_{\mathrm{O}} \sum_{\mathrm{O}} \mathbf{R}_{\mathrm{O}} + w_{\mathrm{P}} \sum_{\mathrm{P}} \mathbf{R}_{\mathrm{P}} \tag{4.11}$$

with oxygen and phosphorous weighting coefficients $w_{\mathrm{O}} = -2$ and $w_{\mathrm{P}} = N_{\mathrm{O}} - N_{\mathrm{H}}/N_{\mathrm{P}}$ (where N_{X} is the number of atoms of species X). The weighting coefficients were chosen in order to ensure that the translational motion of neutral water molecules and neutral PA groups is automatically eliminated. The first term correspond to "bare" proton conduction, as it would be measured in a gas of free protons (in that case all proton displacement translates to proton conduction). The second term eliminates the contribution of the protons in neutral water as they don't contribute to a net charge displacement (almost rigid water molecules are assumed). The third term eliminates the contribution from the motion of phosphonic groups, which have oxygen and hydrogen atoms contributing to the previous terms in $\mathcal{Q}$, but do not contribute to a net charge displacement. Finally, the motion of the polymer backbone is, by construction, nearly irrelevant for the evolution of

$\mathcal{Q}$, as only acidic protons are considered (this is equivalent to a fourth term eliminating the contributions of carbonic protons).

From the variable $\mathcal{Q}$, the effective ionic current density $\mathcal{J}$ can be obtained, via $\mathcal{J} = e\dot{\mathcal{Q}}(t)/\Omega$. This in turn enables the conversion of $\mathcal{Q}(t)$ into a conductivity σ, under the assumption of a fictitious external field $\mathcal{E} = \mathcal{F}/e$ acting (only) on the protons:

$$\sigma = \frac{\mathcal{J}}{\mathcal{E}} \times \frac{c_+^{\text{exp}}}{c_+^{\text{calc}}} = \frac{e^2\,\dot{\mathcal{Q}}(t)}{\Omega\,\mathcal{F}} \times \frac{c_+^{\text{exp}}}{c_+^{\text{calc}}}. \tag{4.12}$$

In order to compare σ with the experimentally measured ionic conductivity, in Eq. (4.12), $\mathcal{J}/\mathcal{E}$ must be rescaled with the ratio of experimental to computational H^+ concentrations $c_+^{\text{exp}}/c_+^{\text{calc}}$. As these concentrations reflect the amount of dissociated phosphonic groups, the experimentally expected value can be obtained from the equilibrium constant

$$K_a^{\Theta} = \frac{[\text{H}^+]\,[\text{HPO}_3^-]}{[\text{H}_2\text{O}]\,[\text{H}_2\text{PO}_3]} \tag{4.13}$$

and the charge neutrality condition, if water dissociation is neglected:

$$\gamma := \frac{c_+^{\text{exp}}}{c_{\text{H}_2\text{PO}_3}^{\text{exp}}} = \sqrt{K_a^{\Theta}\,\frac{[\text{H}_2\text{O}]}{[\text{H}_2\text{PO}_3] + [\text{HPO}_3^-]}}. \tag{4.14}$$

Using the numerical value of phosphoric acid (H_3PO_4) of $K_{\text{PVPA}}^{\Theta} = 1.38 \cdot 10^{-4}$ [23] and an approximate experimental water/acid concentration ratio of $\frac{[\text{H}_2\text{O}]}{[\text{H}_2\text{PO}_3]+[\text{HPO}_3^-]} \approx 0.2$ [49], the expected dissociation ratio is $\gamma \approx 5 \cdot 10^{-3}$. On average, this corresponds to one excess proton per 200 PA groups, while our computational model contains a 25 times higher charge carrier concentration in the wet PVPA and 12.5 times higher in the dry PVPA. Thus, the computed conductivity in the wet system has to be rescaled by $c_+^{\text{exp}}/c_+^{\text{calc}} = 1/25 = 0.04$ and $c_+^{\text{exp}}/c_+^{\text{calc}} = 1/12.5 = 0.02$ in eq. (4.12) for the wet and dry systems, respectively at T =300 K. For different temperatures, the factors are adjusted with the law $K_a(T) = \exp[-\Delta G/k_B T] = \exp[\ln(K_a^{300\text{K}})300\text{K}/T]$. The obtained raw and rescaled values of σ are shown in table 4.3.

The evolution of the component $\mathcal{Q}_x$ parallel to the external driving force is shown in fig. 4.6 for three sets of temperature. The straight lines are linear regressions of the actual data.

T [K]	$\sigma^{\text{w}}_{\text{raw}}$ $\left[\frac{\text{S}}{\text{cm}}\right]$	σ^{w} $\left[\frac{\text{S}}{\text{cm}}\right]$	$P^{max}_{\vert\vert\Delta\tilde{\mathcal{Q}}\vert\vert}$	$\sigma^{\text{w}}_{\text{raw}}$ $\left[\frac{\text{S}}{\text{cm}}\right]$	σ^{d} $\left[\frac{\text{S}}{\text{cm}}\right]$	$P^{max}_{\vert\vert\Delta\tilde{\mathcal{Q}}\vert\vert}$
100	>0.01	>0.0001	2.425	0.19	>0.0001	2.403
300	0.04	0.0016	2.415	0.37	0.0073	2.444
400	0.90	0.1100	2.403	0.08	0.0049	2.424
500	2.50	0.5922	2.410	0.02	0.0024	2.419
600	0.25	0.0913	2.416	0.40	0.0738	2.418

Table 4.3: The raw and rescaled conductivity σ obtained from the average slope of $\mathcal{Q}$ and the peak value $P^{max}_{||\Delta\tilde{\mathcal{Q}}||}$ at which the probability of a jump is maximal (i.e. the optimal O-O distance for a H jump). All properties are presented for the wet (left) and dry (right) PVPA under different temperatures and an external force bias of intensity $F = 30$ pN.

The top plot illustrates that for $T = 300$ pN, there is virtually no change in $\mathcal{Q}_x$ above the noise level during the trajectory of 25 ps duration, neither for the dry (grey line) nor for the wet (black line) PVPA model. Increasing the external driving force tenfold leads to a significant trend of $\mathcal{Q}_x$ for the wet model at $T = 400K$ (center graph) and an even stronger trend at $T = 500K$ (bottom graph). The dry setup, in turn, exhibits a certain drift in $\mathcal{Q}_x$ as well, but with a considerably smaller magnitude than the humidified polymer.

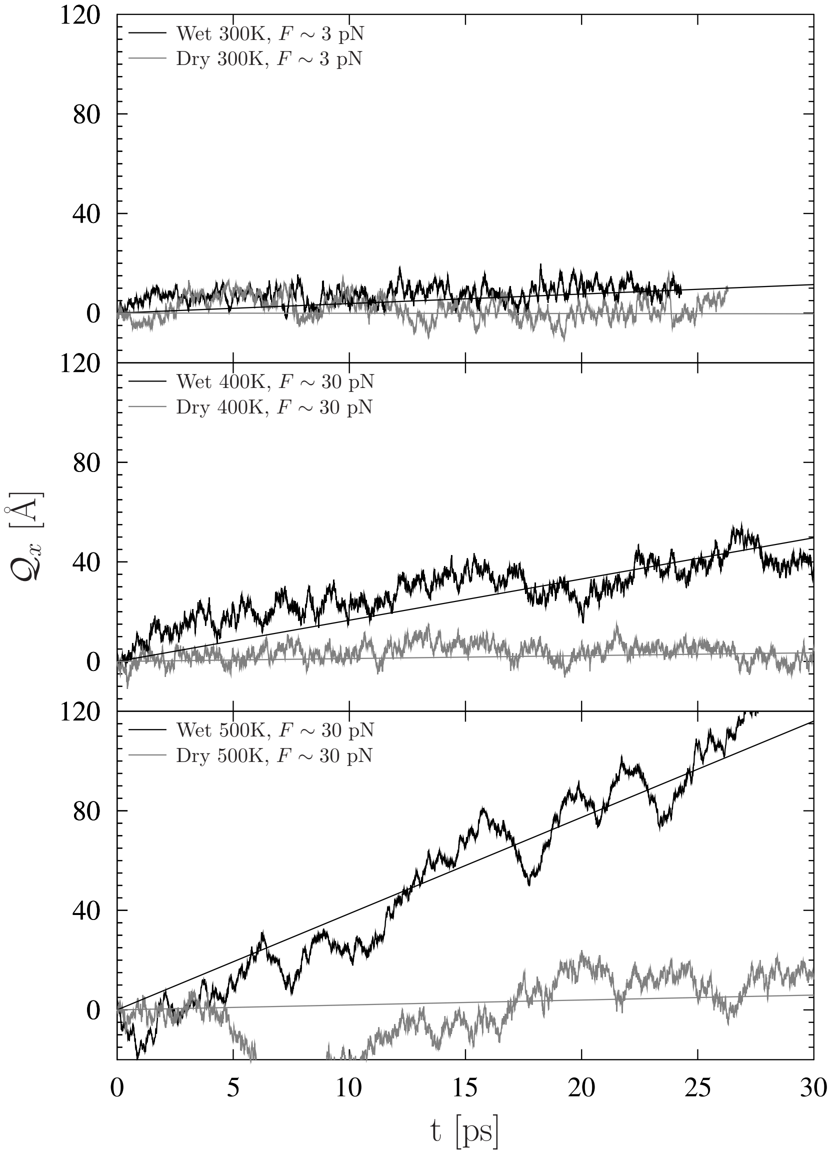

Figure 4.6: Evolution of the component of $\mathcal{Q}$ in the axis of the applied force for dry and wet PVPA, under different temperatures and external forces.

All components of the conduction variable ($\mathcal{Q}_x$, $\mathcal{Q}_y$, $\mathcal{Q}_z$) show uncorrelated oscillations of amplitude ~10Å, which correspond to the natural intra- and interchain hopping of protons, along

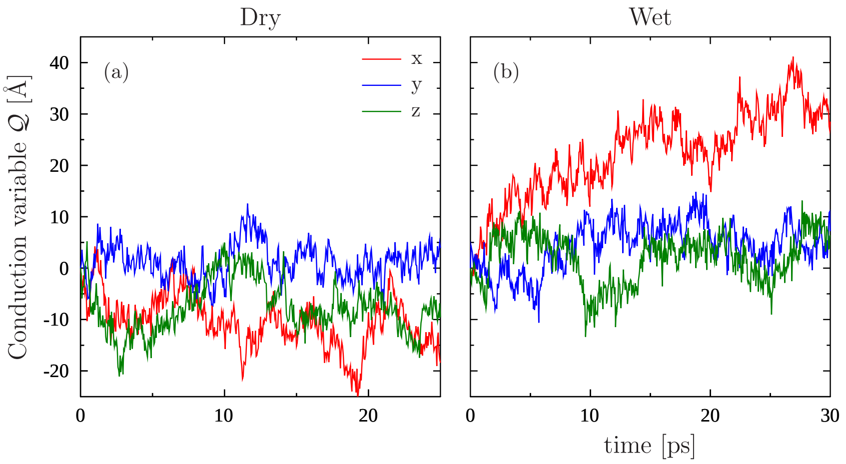

Figure 4.7: x (red), y (blue) and z (green) components of the conduction variable $\mathcal{Q}$, for one of the dry (left) and wet (right) PVPA with $T = 400$ K.

with other fast oscillations of amplitude $\sim$ 1 Å (see fig. 4.7). This natural fluctuations set the limit for the precision in the calculation of the conduction drift to ± 0.03 S/cm.

The numerical values of the ionic conductivities derived via eqs. (4.11) and (4.12) are summarized in table 4.3. In combination with the proton jump rates reported previously (table 4.1), this shows that the long-range transport of excess protons is hindered in the dry environment despite the numerous successful proton jump events. Varying the temperature at constant $\mathcal{F}$ from 100 K to 500 K results in an increase in the drift in the case of the wet system, while the dry system shows no clear trend (table 4.3). These behaviors do not hold in the $T = 600K$ runs, which might be associated with the fact that the material itself has been found to degrade to ∼15% between 473 K and 743 K [44, 49].

As mentioned in previous section, the 300 K low conductivity σ in the wet system seems to be caused by the system being found in a configurational potential minima, where the excess protons were unable to reach the water vehicle, thus hindering the dynamics of the protons in the system. The effect can be seen in the correlation of unusually low σ with the also unusually low concentration ratio $\frac{[H_3O^+]}{[PO_3H_3^+]}$ and jump rate $1/\tau_H$ (see section 4.2). A similar situation can be observed in the 500 K simulation of the dry system, where although there is a good amount of proton jumping, the lack of intervention of water molecules leads to a lack of net sustained flux.

A closer inspection of the obtained trajectories reveals interruptions of the percolating hydrogen bond network as the most likely reason for the absence of persistent conduction in the dry system. A sustained net flow of protons withing a polymer chain would require phosphonic groups to twist $\sim$180°, which is (from observation) a rather rare event. The potential barrier for a concerted proton hopping within one polymer chain is therefore too high, and the protons must either jump out of the polymer chain (which is highly facilitated by nearby water molecules) or jump back in to the previous phosphonic group, thus not contributing to proton conduction.

4.3.1 $\Delta\tilde{Q}$ *and the O-O distance of a jump.*

The derivative of Q variable has a direct relation to the distance of a proton jump. The change due to an individual jump is, however, under the noise of the natural vibrations of the system. To study this property, a modified $\tilde{Q}$ is defined, in which the position of any hydrogen is taken to be that of the oxygen to which it binds,

$$\mathbf{R}_{H_i} \to \mathbf{R}_{O_j} \ , \tag{4.15}$$

where proton H_i is bonded to oxygen O_j. In this way, each hopping event can clearly be seen as a discrete jump in the $\tilde{\mathcal{Q}}$ variable: from eq. (4.11):

$$\Delta\tilde{\mathcal{Q}} = \sum_i \mathbf{R}_{O(new)} - \mathbf{R}_{O(old)} = \sum d_{O-O} \ , \tag{4.16}$$

where d_{O-O} is the distance between the oxygen to which the proton was bonded before the jump and the oxygen to which it has jumped during a simulation timestep τ.

The probability of a jump for a given $||\Delta\tilde{\mathcal{Q}}||$ in a timestep τ is from eq. 4.16 equivalent to the probability of jumps for a given O-O distance. This probability density is shown in fig. 4.8 for the wet and dry systems at different temperatures. There, and more clearly in table 4.3, a narrow peak at $||\Delta\tilde{\mathcal{Q}}|| \sim 2.4$ Å can be observed for both dry and wet systems at all temperatures, all cases sharing essentially the same distribution. A H-hopping optimized configuration of this system should set O-O distances to that value. As the distribution of jumps in both wet and dry systems is identical, we infer that the dynamics in both systems is governed by the same mechanism.

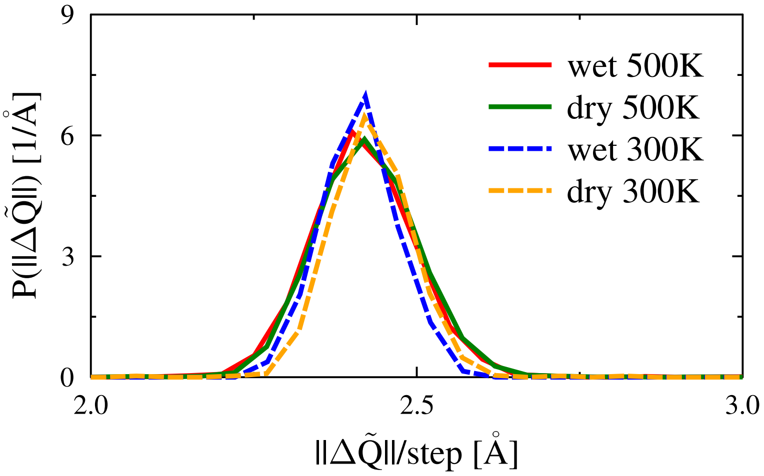

Figure 4.8: Distribution of $\Delta\tilde{Q}$ between successive MD timesteps (0.5fs) for the wet and dry systems at 300K and 400K. This $P(\parallel \Delta\tilde{Q} \parallel)$ represents the distribution of oxygen-oxygen distances at the moment of an H^+ jump event.

4.4 Conclusion

An atomistic picture of the proton conduction mechanism of PVPA was presented in this chapter. The outcome of this study shows that the residual water molecules are required as short-distance vehicles for sustained proton conduction, in agreement with experimental observations. In addition, a simple method to actively simulate conduction on an atomistic level was presented, along with a proposal of microscopic conduction variable connected to measurable macroscopic quantities.

The comparison between the wet and dry PVPA clearly demonstrates the inalienability of water within PVPA for proton conduction purposes. In particular, we find that although proton hopping between two adjacent phosphonic groups occurs rather frequently, a sustained net flow of protons, which would require a phosphonic group to twist ~180°, is a rare event. As a consequence the potential barrier for a concerted proton hopping within the polymer chain can hardly be overcome by the protons directly, so that the conduction process can only be effective if the protons are permitted to jump out of the polymer chain. In the dry system this is only possible via direct interchain hopping, while the higher proton conduction in the wet system immediately suggests that the potential barrier is further lowered by enabling a water-mediated proton hopping between the polymer chains. Since at the same time, essentially no pure vehicular proton conduction has been observed in our calculations, we conclude that the main role of water is to bridge the path of the protons when hopping among phosphonic groups, hence to catalyze interchain hopping. This eventually leads to a water-mediated Grotthuss mechanism.

This microscopic picture of the transport mechanism feeds hope that the short-range-vehicle role of the intercalated water molecules could be taken by other functional groups which might eventually replace the water. Such flexibly anchored groups within the PVPA polymer, would enable sustained proton conduction well beyond the boiling point of water.

Chapter 5

Summary

In this work, two important open issues for the implementation of Proton Exchange Membrane Fuel Cells (PEMFCs) were addressed from a computational materials science approach. These issues are namely the problems of hydrogen storage and high temperature proton conduction. Here, we have used *ab-inito* molecular dynamics to study two promising materials for the solution of these open problems.

In chapter 3, our study of the lithium imide/amide (Li_2NH/-$LiNH_2$) hydrogen storage system at room temperature was presented. The main questions addressed were the elucidation of the proper structure of the material at room temperature and the understanding of the quantum nature of hydrogen nuclei in the bulk Li_2NH, as well as its influence in the structure. In this system, the quantum nature of hydrogen atoms could play a relevant role both in the structure and the dynamics of the system. A DFT study may not be sufficient to account for the nuclear quantum effects. Therefore, the structural properties of lithium imide and amide were studied on the atomic scale with *ab-initio* Path-Integral Molecular Dynamics (PIMD) simulations, thus providing insight in the atomic dynamics up to the nuclear quantum level of accuracy.

Our results show that the Li atoms are more mobile and more disordered than suggested by Xray experiments. This pronounced local disorder in the lithium sublattice is fully consistent with the observed high Li diffusion constant.

The orientation of the formed N-H bonds in Li_2NH relative to the stable nitrogen lattice was elucidated and related to the ^1H NMR chemical shifts. Comparison with ^1H NMR experiments support the computational results of a disordered Li lattice against an ordered one.

Concerning to the nature of the protons in Li_2NH, the presented PIMD calculations suggest the plausibility of proton quantum delocalization in the bulk Li_2NH material. The toroid-shaped potential in which the protons move, which we found to be virtually flat with respect to the azimuthal angle, would lead to quantum delocalization of the NH protons.

The second main aspect of hydrogen technology treated in this work is proton conduction at high temperatures, presented in chap. 4. There, the proton conduction process in poly[vinyl phosphonic acid] (PVPA) was studied. This material is particularly promising as a PEMFC membrane because it exhibits significant proton conductivity at temperatures higher than the boiling temperature of water.

The proton conduction process within PVPA was studied on the atomic scale with a steered *ab-initio* molecular dynamics approach. The specific aim of this study was to describe the main contributions to proton conduction in PVPA, in order to explain the known loss of conductivity when the system is highly dried.

For this study, a specific method was developed to simulate conduction on an atomic level. It consists in applying a force bias in a given direction to the set of protons that can contribute to proton conduction (i.e. the acidic protons), effectively mimicking the expected effect of a constant potential difference.

The outcome of this study shows that sustained proton conduction occurs effectively in the PVPA system only when enough water content is present ("wet" PVPA), a fact that is in agreement with experimental observations. The main mechanism for proton conduction in the studied systems is a water-mediated Grotthus mechanism, viz. a Grotthuss-style hopping mechanism that must be supported by short-distance transport of hydronium ions to neighboring acids. In effect, the presence of residual water molecules is essential to the effectiveness of the process of proton conduction, since these have the function of "bridging" the path of the protons when hopping among phosphonic groups. This explains the low conduction rate in the case of the dry system, even when conduction through mechanical transportation molecules is essentially absent.

As an immediate "tangible" outcome, this work has spanned a series of first-authored articles [69, 70, 71] in peer-reviewed international journals.

We hope that the gain in the understanding of the microscopic properties of the studied materials that we provide in this work will help the future development of improved materials for fuel cells, and consequently having contributed our grain of salt to the solution of current energy problems and its related environmental problems.

Appendix A

Proof of the Hohenberg-Kohn Theorems

A.1 First HK Theorem

The external potential $v(\mathbf{r})$ is determined, within a trivial additive constant, by the electron density $\rho(\mathbf{r})$.

The proof of this theorem is by reduction to an absurd. Let us suppose that the theorem is false, and there are two different potentials $v(r)$ and $\tilde{v}(r)$ that have the same ground-state density ρ_0. In addition, let us assume an already antisymmetrized and normalized ground-state wavefunction Ψ_0,

$$
\begin{aligned}
\Psi_0(\mathbf{r}_1 \cdots \mathbf{r}_N) &= \Psi_0[\rho_o(\mathbf{r})](\mathbf{r}_1 \cdots \mathbf{r}_N) && \text{(A.1)} \\
\rho_0(\mathbf{r}_1 \cdots \mathbf{r}_N) &= N \int \cdots \int \mathrm{d}^3\mathbf{r}_1 \cdots \mathrm{d}^3\mathbf{r}_N |\Psi_0(\mathbf{r}_1 \cdots \mathbf{r}_N)|^2 \ . && \text{(A.2)}
\end{aligned}
$$

We will use the *variational theorem* of quantum mechanics, which states that the ground-state wavefunction Ψ_0 is the wavefunction that minimizes the energy, that is, if the ground state of the system is nondegenerate, for every test wavefunction $\tilde{\Psi}$

the following holds:

$$E_0 \leq \frac{\langle\tilde{\Psi}|H|\tilde{\Psi}\rangle}{\langle\tilde{\Psi}|\tilde{\Psi}\rangle} , \tag{A.3}$$

where the equality occurs only for the ground-state function

$$E_0 = \frac{\langle\Psi_0|H|\Psi_0\rangle}{\langle\Psi_0|\Psi_0\rangle} . \tag{A.4}$$

Applying this to the two Hamiltonians H and $\tilde{H}$, which result from the same number N of nuclei interacting with the electrons with potential $v(r)$ and $\tilde{v}(r)$, respectively, we obtain the inequalities

$$\tilde{E}_0 \leq \frac{\langle\tilde{\Psi}_0|H|\tilde{\Psi}_0\rangle}{\langle\tilde{\Psi}_0|\tilde{\Psi}_0\rangle} \tag{A.5}$$

$$E_0 \leq \frac{\langle\Psi_0|\tilde{H}|\Psi_0\rangle}{\langle\Psi_0|\Psi_0\rangle} . \tag{A.6}$$

Adding these inequalities (and remembering that the wavefunctions are normalized) we get

$$E_0 + \tilde{E}_0 \leq \langle\tilde{\Psi}_0|\tilde{H}|\tilde{\Psi}_0\rangle + \langle\Psi_0|H|\Psi_0\rangle \tag{A.7}$$

$$= \langle\tilde{\Psi}_0|\tilde{H} - H + H|\tilde{\Psi}_0\rangle + \langle\Psi_0|H|\Psi_0\rangle \tag{A.8}$$

Adding the two terms $\langle\tilde{\Psi}_0|\tilde{H}|\tilde{\Psi}_0\rangle$ and $\langle\Psi_0|H|\Psi_0\rangle$, which by the variational theorem are a positive contribution, we get

$$E_0 + \tilde{E}_0 < \langle\tilde{\Psi}_0|\tilde{H}|\tilde{\Psi}_0\rangle + \langle\Psi_0|H|\Psi_0\rangle + \tag{A.9}$$

$$\langle\tilde{\Psi}_0|\tilde{H} - H|\tilde{\Psi}_0\rangle + \langle\Psi_0|H - \tilde{H}|\Psi_0\rangle \tag{A.10}$$

Now, expressing the previous equation in terms of densities and taking the hypothesis that both wavefunctions result in the same densities $\rho_0 = |\Psi_0|^2 = |\tilde{\Psi}_0|^2 = \tilde{\rho}_0$, we obtain (after cancelling terms):

$$\begin{aligned} 0 &< \int \mathrm{d}^N \mathbf{r} \rho\left(\{\mathbf{r}_i\}\right) \sum_i \left(v(r_i) - \tilde{v}(r_i)\right) + \\ & \int \mathrm{d}^N \mathbf{r} \rho(\{\mathbf{r}_i\}) \sum_i \left(\tilde{v}(r_i) - v(r_i)\right) \qquad \text{(A.11)} \\ \Rightarrow 0 &< 0 \, . \qquad \text{(A.12)} \end{aligned}$$

The last equation occurs since both integrals can be combined, and it is an absurd. Therefore, the hypothesis must be false. As a consequence, if two systems of electrons which share the same ground state density are subject to potentials $v(\mathbf{r})$ and $\tilde{v}(\mathbf{r})$, these potentials must differ in less than a constant.

A.2 Second HK Theorem

*For a v-*representable *trial density $\tilde{\rho}(\mathbf{r})$, such that $\tilde{\rho}(\mathbf{r}) \geq 0$ and $\int \tilde{\rho}(\mathbf{r})\mathrm{d}\mathbf{r} = N$, the value of the energy functional $E_v[\tilde{\rho}]$ of the corresponding distribution is an upper bound of the ground state E_0,*

$$E_0 \leq E_v[\tilde{\rho}] \qquad \text{(A.13)}$$

The proof of this theorem is by using the first HK theorem and the variational theorem. In fact, this can be thought as a generalization of the variational theorem from wavefunctions to ground-state densities.

A trial density $\tilde{\rho}(\{\mathbf{r}_i\})$ that fulfills all conditions of the theorem will be bound to the result of the first HK theorem, that is, the potential $\tilde{v}(\mathbf{r})$ is determined by $\tilde{\rho}$. As the Schrödinger equation determines the wavefunction of the system, and the potential is determined by the density, there is a wavefunction $\tilde{\Psi}$ generating $\tilde{\rho}$, which is the solution to the equation

$$\left(T + \sum_i \tilde{v}(\mathbf{r}_i)\right) \tilde{\Psi} = \tilde{H}\tilde{\Psi} = \tilde{E}\tilde{\Psi} \ , \tag{A.14}$$

where T is the kinetic energy operator.

The resulting wavefunction will fulfill $|\tilde{\Psi}(\{\mathbf{r}_i\})|^2 = \tilde{\rho}(\{\mathbf{r}_i\})$, as well as the variational theorem, yielding

$$E_v[\rho_0] = E_0 = \langle \Psi_0 | H | \Psi_0 \rangle \leq \langle \tilde{\Psi} | H | \tilde{\Psi} \rangle = E_v[\tilde{\rho}] \ , \tag{A.15}$$

where the variables with subindex 0 correspond to the ground state. The equality occurs if and only if $\Psi_0 = \tilde{\Psi}$, which is only met if $\rho_0 = \tilde{\rho}$.

Bibliography

[1] Ashcroft, N. W. and Mermin, N. D., *Solid state physics*. Saunders, Philadelphia, 1976.

[2] Aslan, A. and Bozkurt, A., "Development and characterization of polymer electrolyte membranes based on ionical cross-linked poly(1-vinyl-1,2,4 triazole) and poly(vinylphosphonic acid)," *J. Power Sources*, vol. 191, p. 442, 2009.

[3] Aslan, A., Celik, S. U., and Bozkurt, A., "Proton-conducting properties of the membranes based on poly(vinyl phosphonic acid) grafted poly(glycidyl methacrylate)," *Solid State Ion.*, vol. 180, p. 1240, 2009.

[4] Bachelet, G. B., Hamann, D. R., and Schluter, M., "Pseudopotentials that work," *Phys. Rev. B*, vol. 26, p. 4199, 1982.

[5] Bakker, H. J. and Nienhuys, H.-K., "Delocalization of Protons in Liquid Water," *Science*, vol. 297, p. 587, 2002.

[6] Balogh, M. P., Jones, C. Y., Herbst, J., Hector, L. G., Jr., and Kundrat, M., "Crystal structures and phase transformation of deuterated lithium imide, Li_2ND," *J. All. Comp.*, vol. 420, p. 326, 2006.

[7] Becke, A. D., "Density-functional exchange-energy approximation with correct asymptotic behavior," *Phys. Rev. A*, vol. 38, p. 3098, 1988.

[8] Binder, K., *Monte Carlo and molecular dynamics simulations in polymer science.* Oxford Univ. Press, 1995.

[9] Blake, N. P., Petersen, M. K., Voth, G. A., and Metiu, H., "Structure of hydrated Na-Nafion polymer membranes," *J. Phys. Chem. B*, vol. 109, p. 24244, 2005.

[10] Boero, M., Ikeshoji, T., and Terakura, K., "Density and temperature dependence of proton diffusion in water: A first-principles molecular dynamics study," *ChemPhysChem*, vol. 6, p. 1775, 2005.

[11] Brown, S. P. and Spiess, H. W., "Advanced solid-state nmr methods for the elucidation of structure and dynamics of molecular, macromolecular, and supramolecular systems," *Chem. Rev.*, vol. 101, p. 4125, 2001.

[12] Car, R. and Parrinello, M., "A combined approach to DFT and molecular dynamics," *Phys. Rev. Lett.*, vol. 55, p. 2471, 1985.

[13] Ceperley, D., "Path integrals in the theory of condensed helium," *Rev. Mod. Phys.*, vol. 67, p. 279, 1995.

[14] Ceperley, D. M. and Alder, B. J., "Ground state of the electron gas by a stochastic method," *Phys. Rev. Lett.*, vol. 45, p. 566, 1980.

[15] Cheeseman, J. R., Trucks, G. W., Keith, T. A., and Frisch, M. J., "A comparison of models for calculating nuclear

magnetic resonance shielding tensors," *J. Chem. Phys.*, vol. 104, p. 5497, 1996.

[16] Committee on Alternatives and Strategies for Future Hydrogen Production and Use, National Research Council, National Academy of Engineering, *The Hydrogen Economy: Opportunities, Costs, Barriers, and R&D Needs*. The National Academies Press, 2004.

[17] David, W. I. F., Jones, M. O., Gregory, D. H., Jewell, C. M., Johnson, S. R., Walton, A., and Edwards, P. P., "A mechanism for non-stoichiometry in the lithium amide/lithium imide hydrogen storage reaction," *J. Am. Chem. Soc.*, vol. 129, p. 1594, 2007.

[18] de Grotthuss, C. J. T., "Sur la décomposition de l'eau et des corps qu'elle tient en dissolution à l'aide de l'électricité galvanique," *Ann. Chim.*, vol. 58, p. 54, 1806.

[19] Ditchfield, R., "Gauge including atomic orbitals," *J. Chem. Phys.*, vol. 56, p. 5688, 1972.

[20] Dobrovolskis, A. R., Alvarellos, J. L., and Lissauer, J. J., "Lifetimes of small bodies in planetocentric (or heliocentric) orbits," *icarus*, vol. 188, p. 481, 2007.

[21] Elliott, J. A. and Paddison, S. J., "Modelling of morphology and proton transport in PFSA membranes," *Phys. Chem. Chem. Phys.*, vol. 9, p. 2602, 2007.

[22] Feynman, R. P. and Hibbs, A. R., *Quantum mechanics and path integrals*. McGraw-Hill New York, 1965.

[23] Franz, R. G., "Comparisons of pKa and Log P values of some carboxylic and phosphonic acids: Synthesis and measurement," *AAPS Pharmsci.*, vol. 3, p. 10, 2001.

[24] Gasteiger, H. A., Kocha, S. S., Sompalli, B., and Wagner, F. T., "Activity benchmarks and requirements for pt, pt-alloy, and non-pt oxygen reduction catalysts for pemfcs," *Applied Catalysis B: Environmental*, vol. 56, p. 9, 2005.

[25] Geissler, P. L., Dellago, C., Chandler, D., Hutter, J., and Parrinello, M., "Autoionization in liquid water," *Science*, vol. 291, p. 2121, 2001.

[26] Goedecker, S., Teter, M., and Hutter, J., "Separable dual-space gaussian pseudopotentials," *Phys. Rev. B*, vol. 54, p. 1703, 1996.

[27] Goedecker, S., Teter, M., and Hutter, J., "Separable dual-space gaussian pseudopotentials," *Phys. Rev. B*, vol. 54, p. 1703, 1996.

[28] Goktepe, F., Celik, S. U., and Bozkurt, A., "Preparation and the proton conductivity of chitosan/poly(vinyl phosphonic acid) complex polymer electrolytes," *J. Non-Cryst. Solids*, vol. 354, p. 3637, 2008.

[29] Gregory, D. H., "Lithium nitrides, imides and amides as lightweight, reversible hydrogen stores," *J. Mater. Chem.*, vol. 18, p. 2321, 2008.

[30] Grotjahn, D. B., Sheridan, P. M., Al Jihad, I., and Ziurys, L. M., "First synthesis and structural determination of a monomeric, unsolvated lithium amide, $LiNH_2$," *J. Am. Chem. Soc.*, vol. 123, no. 23, p. 5489, 2001.

[31] Hamann, D. R., Schluter, M., and Chiang, C., "Norm-Conserving pseudopotentials," *Phys. Rev. Lett.*, vol. 43, p. 1494, 1979.

[32] Hayes, R. L., Paddison, S. J., and Tuckerman, M. E., "Proton transport in triflic acid hydrates studied via path integral car-parrinello molecular dynamics," *J. Phys. Chem. B*, vol. 113, p. 16574, 2009.

[33] Hellmann, H., "A new approximation method in the problem of many electrons," *J. Chem. Phys.*, vol. 3, p. 61, 1935.

[34] Hellmann, H., "Metallic binding according to the combined approximation procedure," *J. Chem. Phys.*, vol. 4, p. 324, 1936.

[35] Hohenberg, P. and Kohn, W., "The inhomogeneous electron gas," *Phys. Rev.*, vol. 136, p. B864, 1964.

[36] Hu, Y. H. and Ruckenstein, E., "Hydrogen storage of Li_2NH prepared by reacting Li with NH_3," *Ind. Eng. Chem. Res.*, vol. 45, p. 182, 2006.

[37] Hutter, J. and others, "Computer code CPMD, version 3.12." Copyright IBM Corp. and MPI-FKF Stuttgart 1990-2008, `www.cpmd.org`.

[38] Iannuzzi, M., "Proton transfer in imidazole-based molecular crystals," *J. Chem. Phys.*, vol. 124, p. 204710, 2006.

[39] Iannuzzi, M. and Parrinello, M., "Proton transfer in heterocycle crystals," *Phys. Rev. Lett.*, vol. 93, p. 025901, 2004.

[40] Iannuzzi, M., Laio, A., and Parrinello, M., "Efficient exploration of reactive potential energy surfaces using car-parrinello molecular dynamics," *Phys. Rev. Lett.*, vol. 90, p. 238302, 2003.

[41] Ichikawa, T. and Isobe, S., "The structural properties of amides and imides as hydrogen storage materials," *Z. Kristallogr.*, vol. 223, p. 660, 2008.

[42] Jameson, C. J. and de Dios, A. C., "Theoretical and physical aspects of nuclear shielding," *Nucl. Mag. Res.*, vol. 33, p. 47, 2004.

[43] Jannasch, P., "Recent developments in high-temperature proton conducting polymer electrolyte membranes," *Current Opinion in Colloid & Interface Science*, vol. 8, p. 96, 2003.

[44] Jiang, D. D., Yao, Q., McKinney, M. A., and Wilkie, C. A., "TGA/FTIR studies on the thermal degradation of some polymeric sulfonic and phosphonic acids and their sodium salts," *Polymer Degradation and Stability*, vol. 63, p. 423, 1999.

[45] Jiang, F., Kaltbeitzel, A., Fassbender, B., Brunklaus, G., Pu, H., Meyer, W. H., Spiess, H. W., and Wegner, G., "Effect of Polymer Composition and Water Content on Proton Conductivity in Vinyl Benzyl Phosphonic Acid-4-Vinyl Pyridine Copolymers," *Macromol. Chem. Phys.*, vol. 209, p. 2494, 2008.

[46] Jiménez-García, L., Kaltbeitzel, A., Pisula, W., Gutmann, J. S., Klapper, M., and Müllen, K., "Phospho-

nated hexaphenylbenzene: A crystalline proton conductor," *Angew. Chem. Intl. Ed.*, vol. 48, p. 9951, 2009.

[47] Jones, R. O. and Gunnarsson, O., "The density functional formalism, its applications and prospects," *Rev. Mod. Phys.*, vol. 61, p. 689, 1989.

[48] Kalapos, T., Decker, B., Every, H., Ghassemi, H., and Zawodzinski., T., "Thermal studies of the state of water in proton conducting fuel cell membranes," *Journal of Power Sources*, vol. 172, p. 14, 2007.

[49] Kaltbeitzel, A., Schauff, S., Steininger, H., Bingöl, B., Brunklaus, G., Meyer, W. H., and Spiess, H. W., "Water sorption of poly(vinylphosphonic acid) and its influence on proton conductivity," *Solid State Ionics*, vol. 178, p. 469, 2007.

[50] Keith, T. A. and Bader, R. F. W., "Calculation of magnetic response properties using a continuous set of gauge transformations," *Chem. Phys. Lett.*, vol. 210, p. 223, 1993.

[51] Kleinman, L. and Bylander, D. M., "Efficacious form for model pseudopotentials," *Phys. Rev. Lett.*, vol. 48, p. 1425, 1982.

[52] Klerke, A., Christensen, C. H., Norskov, J. K., and Vegge, T., "Ammonia for hydrogen storage: challenges and opportunities," *J. Mater. Chem.*, vol. 18, p. 2304, 2008.

[53] Koch, W. and Holthausen, M. C., *A Chemist's Guide to Density Functional Theory*. Wiley-VCH, 2001.

[54] Kohn, W. and Sham, L. J., "Self-consistent equations including exchange and correlation effects," *Phys. Rev.*, vol. 140, p. A1133, 1965.

[55] Kolafa, J., "Time-reversible always stable predictor-corrector method for molecular dynamics of polarizable molecules," *J. Comp. Chem.*, vol. 25, p. 335, 2004.

[56] Kordesh, K. and Simader, G., *Fuel Cells and Their Applications*. Wiley-VCH, 1996.

[57] Kreuer, K. D., Paddison, S. J., Spohr, E., and Schuster, M., "Transport in proton conductors for fuel-cell applications: Simulations, elementary reactions, and phenomenology," *Chem. Rev.*, vol. 104, p. 4637, 2004.

[58] Krivobokov, I. M., Gribov, E. N., Okunev, A. G., Spoto, G., and Parmon, V. N., "Transport properties of modified nafion membranes: Effect of zeolite and precursors," *Solid State Ionics*, vol. 180, p. 1694, 2010.

[59] Kühne, T., Krack, M., Mohamed, F., and Parrinello, M., "Efficient and accurate Car-Parrinello-like approach to Born-Oppenheimer molecular dynamics," *Phys. Rev. Lett.*, vol. 6, p. 066401, 2007.

[60] Kuo, I.-F. W., Mundy, C. J., McGrath, M. J., Siepmann, J. I., VandeVondele, J., Sprik, M., Hutter, J., Chen, B., Klein, M. L., Mohamed, F., Krack, M., and Parrinello, M., "Liquid water from first principles: Investigation of different sampling approaches," *J. Phys. Chem. B*, vol. 108, p. 12990, 2004.

[61] Kutzelnigg, W., "Individual gauges for localized orbitals," *Isr. J. Chem.*, vol. 19, p. 193, 1980.

[62] Laio, A. and Parrinello, M., "Escaping free-energy minima," *Proc. Natl. Acad. Sci. USA*, vol. 99, p. 12562, 2002.

[63] Lee, C., Yang, W., and Parr, R. G., "Development of the Colle-Salvetti correlation-energy formula into a functional of the electron-density," *Phys. Rev. B*, vol. 37, p. 785, 1988.

[64] Lee, Y., Bingöl, B., Murakhtina, T., Sebastiani, D., Meyer, W., Wegner, G., and Spiess, H., "High resolution solid state nmr studies of poly(vinyl phosphonici acid) proton conducting polymer: Molecular structure and proton dynamics," *J. Phys. Chem. B*, vol. 111, p. 9711, 2007.

[65] Lee, Y., Murakhtina, T., Sebastiani, D., and Spiess, H., "^{2}H solid state nmr of mobile protons: It is not always the simple way," *J. Am. Chem. Soc.*, vol. 129, p. 12406, 2007.

[66] Lippert, G., Hutter, J., and Parrinello, M., "A hybrid gaussian and plane wave density functional scheme," *Mol. Phys.*, vol. 3, p. 477, 1997.

[67] Lippert, G., Hutter, J., and Parrinello, M., "A hybrid gaussian and plane wave density functional scheme," *Mol. Phys.*, vol. 92, p. 477, 1997.

[68] Lowton, R. L., Jones, M. O., David, W. I. F., Johnson, S. R., Sommariva, M., and Edwards, P. P., "The synthesis

and structural investigation of mixed lithium/sodium amides," *J. Mater. Chem.*, vol. 18, p. 2355, 2008.

[69] Ludueña, G. A., Kühne, T. D., and Sebastiani, D., "Mixed grotthuss and vehicle transport mechanism in proton conducting polymers from ab-initio molecular dynamics simulations," *Chem. Mat.*, vol. in print, 2011.

[70] Ludueña, G. A. and Sebastiani, D., "Possibility of coherent delocalized nuclear quantum states of protons in Li_2NH," *J. Phys. Chem. Lett.*, vol. 1, p. 3214, 2010.

[71] Ludueña, G. A., Wegner, M., Bjålie, L., and Sebastiani, D., "Local disorder in hydrogen storage compounds: The case of lithium amide/imide," *ChemPhysChem*, vol. 11, p. 2353, 2010.

[72] Luo, W. and Hong, M., "Conformational Changes of an Ion Channel Detected Through Water-Protein Interactions Using Solid-State NMR Spectroscopy," *J. Am. Chem. Soc.*, vol. 132, p. 2378, 2010.

[73] Markovitch, O., Chen, H., Izvekov, S., Paesani, F., Voth, G. A., and Agmon, N., "Special pair dance and partner selection: Elementary steps in proton transport in liquid water," *J. Phys. Chem. B*, vol. 112, p. 9456, 2008.

[74] Marx, D. and Hutter, J., "Ab-initio molecular dynamics: Theory and implementation," in *Modern Methods and Algorithms in Quantum Chemistry*, vol. 1 of *NIC Series*, p. 301, Forschungzentrum Juelich, 2000.

[75] Marx, D. and Parrinello, M., "Ab-initio path-integral molecular-dynamics," *Z. Phys. B Cond. Mat.*, vol. 95, p. 143, 1994.

[76] Médard, C., Lefévre, M., Dodelet, J., Jaouen, F., and Lindbergh, G., "Oxygen reduction by Fe-based catalysts in pem fuel cell conditions: Activity and selectivity of the catalysts obtained with two fe precursors and various carbon supports," *Electrochimica Acta*, vol. 51, p. 3202, 2006.

[77] Moysés Araújo, C., Blomqvist, A., Scheicher, R. H., Chen, P., and Ahuja, R., "Superionicity in the hydrogen storage material Li_2NH: Molecular dynamics simulations," *Phys. Rev. B*, vol. 79, p. 172101, 2009.

[78] Mpourmpakis, G., Froudakis, G. E., Lithoxoos, G. P., and Samios, J., "SiC nanotubes: A novel material for hydrogen storage," *Nano Lett.*, vol. 6, p. 1581, 2006.

[79] Munson, R. A., "Self-dissociative equilibria in molten phosphoric acid," *J. Phys. Chem.*, vol. 68, p. 3374, 1964.

[80] Noritake, T., Nozaki, H., Aoki, M., Towata, S., Kitahara, G., Nakamori, Y., and Orimo, S., "Crystal structure and charge density analysis of Li_2NH by synchrotron x-ray diffraction," *J. All. Comp.*, vol. 393, p. 264, 2005.

[81] Nosé, S., "A unified formulation of the constant temperature molecular dynamics methods," *J. Chem. Phys.*, vol. 81, p. 511, 1984.

[82] Ohoyama, K., Nakamori, Y., Orimo, S., and Yamada, K., "Revised Crystal Structure Model of Li_2NH by Neutron

Powder Diffraction," *J. Phys. Soc. Jap.*, vol. 74, p. 483, 2005.

[83] Paddison, S., "Proton conduction mechanisms at low degrees of hydration in sulfonic acid–based polymer electrolyte membranes," *Annual Review of Materials Research*, vol. 33, p. 289, 2003.

[84] Paddison, S. J. and Paul, R., "The nature of proton transport in fully hydrated nafion," *Phys. Chem. Chem. Phys.*, vol. 4, p. 1158, 2002.

[85] Pan, F., Jia, H., Jiang, Z., and Zheng, X., "Enhanced dehumidification performance of PVA membranes by tuning the water state through incorporating organophosphorus acid," *J. Membr. Sci.*, vol. 325, p. 727, 2008.

[86] Park, S.-Y. and Jang, D.-J., "Accumulated proton-donating ability of solvent molecules in proton transfer," *J. Am. Chem. Soc.*, vol. 132, p. 297, 2010.

[87] Parr, R. G. and Yang, W., *Density functional theory of atoms and molecules*. Oxford Science Publications, 1989.

[88] Perdew, J. P. in *Electronic Structure of Solids* (Ziesche, P. and Eschrig, H., eds.), p. 11, Akademie Verlag, Berlin, 1991.

[89] Perrin, R., Elomaa, M., and Jannasch, P., "Nanostructured Proton Conducting Polystyrene-Poly(vinylphosphonic acid) Block Copolymers Prepared via Sequential Anionic Polymerizations," *Macromol.*, vol. 42, p. 5146, 2009.

[90] Peterson, I., "Time to relax: the concept of fractal time ties together the stretchiness of silk and the brittleness of polymers," *Sci. News*, vol. 135, p. 157, 1989.

[91] Pickett, W. E., "Pseudopotential methods in condensed matter applications," *Comput. Phys. Reports*, vol. 9, p. 115, 1989.

[92] Putrino, A., Sebastiani, D., and Parrinello, M., "Generalized variational density functional perturbation theory," *J. Chem. Phys.*, vol. 113, p. 7102, 2000.

[93] Rosi, N. L., Eckert, J., Eddaoudi, M., Vodak, D. T., Kim, J., O'Keeffe, M., and Yaghi, O. M., "Hydrogen storage in microporous metal-organic frameworks," *Science*, vol. 300, p. 1127, 2003.

[94] Schafer, A., Huber, C., and Ahlrichs, R., "Fully optimized contracted gaussian basis sets of triple zeta valence quality for atoms li to kr," *J. Chem. Phys.*, vol. 100, p. 5829, 1994.

[95] Schlapbach, L. and Zuttel, A., "Hydrogen-storage materials for mobile applications," *Nature*, vol. 414, p. 353, 2001.

[96] Schmidt, J. and Sebastiani, D., "Anomalous temperature dependence of nuclear quadrupole interactions in strongly hydrogen-bonded systems from first principles," *J. Chem. Phys.*, vol. 123, p. 074501, 2005.

[97] Schmidt-Rohr, K. and Chen, Q., "Parallel cylindrical water nanochannels in nafion fuel-cell membranes," *Nature Materials*, vol. 7, p. 75, 2008.

[98] Schuster, M. F. H., Meyer, W. H., Schuster, M., and Kreuer, K. D., "Toward a new type of anhydrous organic proton conductor based on immobilized imidazole," *Chem. Mat.*, vol. 16, p. 329, 2004.

[99] Sebastiani, D., *Development of a new ab initio approach for NMR chemical shifts in periodic systems*. Stuttgart, University, Diss., 2001.

[100] Sebastiani, D., "Ab-initio calculation of nuclear magnetic resonance parameters in condensed phases," *Mod. Phys. Lett. B*, vol. 17, p. 1301, 2003.

[101] Sebastiani, D., Goward, G., Schnell, I., and Spiess, H. W., "NMR chemical shifts in proton conducting crystals from first principles," *J. Mol. Struct.*, vol. 625, p. 283, 2003.

[102] Sebastiani, D. and Parrinello, M., "A new method to compute NMR chemical shifts in periodic systems," *J. Phys. Chem. A*, vol. 105, p. 1951, 2001.

[103] Service, R. F., "New polymer may rev up the output of fuel cells used to power cars," *Science*, vol. 312, p. 35a, 2006.

[104] Sharif, S., Denisov, G., Toney, M., and Limbach, H., "Nmr studies of solvent-assisted proton transfer in a biologically relevant Schiff base: Toward a distinction of geometric and equilibrium H-bond isotope effects," *J. Am. Chem. Soc.*, vol. 128, p. 3375, 2006.

[105] Snook, I., *The Langevin and Generalised Langevin Approach to the Dynamics of Atomic, Polymeric and Colloidal Systems*. Elsevier Science, 2007.

[106] Spiess, H. W., “Advanced solid-state nuclear magnetic resonance for polymer science,” *J. Polymer Sci. A*, vol. 42, p. 5031, 2004.

[107] Sprik, M., Klein, M. L., and Chandler, D., “staging - a sampling technique for the monte-carlo evaluation of path-integrals,” *Phys. Rev. B*, vol. 31, p. 4234, 1985.

[108] Steininger, H., Schuster, M., Kreuer, K. D., Kaltbeitzel, A., Bingöl, B., Meyer, W. H., Schauff, S., Brunklaus, G., Maier, J., and Spiess, H. W., “Intermediate temperature proton conductors for pem fuel cells based on phosphonic acid as protogenic group: A progress report.,” *Phys. Chem. Chem. Phys.*, vol. 9, p. 1764, 2007.

[109] Stoyanov, E. S., Stoyanova, I. V., and Reed, C. A., “The Structure of the Hydrogen Ion (H-aq(+)) in Water,” *J. Am. Chem. Soc.*, vol. 132, p. 1484, 2010.

[110] Sugahara, T., Haag, J. C., Prasad, P. S. R., Warntjes, A. A., Sloan, E. D., Sum, A. K., and Koh, C. A., “Increasing Hydrogen Storage Capacity Using Tetrahydrofuran,” *J. Am. Chem. Soc.*, vol. 131, p. 14616, 2009.

[111] Tangney, P., “On the theory underlying the Car-Parrinello method and the role of the fictitious mass parameter,” *J. Chem. Phys.*, vol. 124, p. 044111, 2006.

[112] Troullier, N. and Martins, J. L., “Efficient pseudopotentials for plane-wave calculations,” *Phys. Rev. B*, vol. 43, p. 1993, 1991.

[113] Tuckerman, M., Laasonen, K., Sprik, M., and Parrinello, M., “Ab-initio molecular-dynamics simulation

of the solvation and transport of hydronium and hydroxyl ions in water," *J. Chem. Phys.*, vol. 103, p. 150, 1995.

[114] Tuckerman, M., Laasonen, K., Sprik, M., and Parrinello, M., "Ab initio molecular dynamics simulation of the solvation and transport of H_3O^+ and OH^- ions in water," *J. Phys. Chem.*, vol. 99, p. 5749, 1995.

[115] Tuckerman, M. E., Berne, B. J., Martyna, G. J., and Klein, M. L., "Efficient molecular dynamics and hybrid monte carlo algorithms for path integrals," *J. Chem. Phys.*, vol. 99, p. 2796, 1993.

[116] Tuckerman, M., D.Marx, Klein, M., and Parrinello, M., "Efficient and general algorithms for path integral carparrinello molecular dynamics," *J. Chem. Phys.*, vol. 104, p. 5579, 1996.

[117] Tuckerman, M., D.Marx, Klein, M., and Parrinello, M., "On the quantum nature of the shared proton in hydrogen bonds," *Science*, vol. 275, p. 817, 1997.

[118] Uras-Aytemiz, N., Devlin, J., Sadlej, J., and Buch, V., "Hcl solvation in methanol clusters and nanoparticles: Evidence for proton-wires," *Chem. Phys. Lett.*, vol. 422, p. 179, 2006.

[119] Vilciauskas, L., Padison, S., and Kreuer, K., "Ab initio modeling of proton transfer in phosphoric acid clusters," *J. Phys. Chem. A*, vol. 113, p. 9193, 2009.

[120] Vondele, J. V., Krack, M., Mohamed, F., Parrinello, M., Chassaing, T., and Hutter, J., "Quickstep: Fast and accurate density functional calculations using a mixed gaus-

sian and plane waves approach," *Comp. Phys. Comm.*, vol. 167, p. 103, 2005.

[121] Wang, C. and Paddison, S. J., "Proton transfer in functionalized phosphonic acid molecules," *Phys. Chem. Chem. Phys.*, vol. 12, p. 970, 2010.

[122] Yates, J. R., Pham, T. N., Pickard, C. J., Mauri, F., Amado, A. M., Gil, A. M., and Brown, S. P., "An investigation of weak CH$\cdots$O hydrogen bonds in maltose anomers by a combination of calculation and experimental solid-state nmr spectroscopy," *J. Am. Chem. Soc.*, vol. 127, p. 10216, 2005.

[123] Zhang, C. J., Dyer, M., and Alavi, A., "Quantum delocalization of hydrogen in the Li_2NH crystal," *J. Phys. Chem. B*, vol. 109, p. 22089, 2005.